Development of 320 GHz Interferometer System for Electron Density Measurement in Heliotron J

Pengfei ZHANG

Abstract

In this dissertation, the diagnostic of electron density in fusion plasma under different fueling techniques is experimentally investigated and analyzed. Increasing the density is beneficial for the confinement in stellarators/heliotron. Understanding high-density plasmas through advanced fueling techniques is crucial to realize better plasma confinement. In Heliotron J, a heliotron fusion device, several fueling techniques, such as pellet injection, supersonic molecular beam injection (SMBI), and short-pulsed high-intensity gas puffing (HIGP), can help achieve high-density plasma.

The interferometer measurement is a standard technique used to measure the electron density of plasma in the magnetically confined plasma. To understand the physics of high-density plasma production, a new 320 GHz multi-channel solid-state source interferometer was designed and constructed for the electron density measurement in Heliotron J. This interferometer is a Michelson type, based on the heterodyne principle, with two independent solid-state sources. Two solid-state submillimeter sources as the microwave generator can provide up to 50 mW submillimeter wave with compacted structure, high stability, and ease maintenance.

This dissertation consists of seven chapters.

In chapter 1, the background of this study is described. To improve the Earth's environment by reducing greenhouse gas emissions, nuclear fusion reactions have great potential as a future energy source. Increasing the plasma density, which is beneficial for energy confinement, makes the measurement and analysis of plasma density very important. The common technique used to measure plasma density on fusion devices is interferometry. The prior study on the development of interferometry is introduced and the motivation and objectives of this study are described.

In chapter 2, the principle of the interferometer for density measurement in plasma is described. Interferometry measures the phase change in plasma to probe the density of

the plasma. The Appleton-Hartree equation is used to derive the phase change before and after electromagnetic wave transmission, which further introduces the relationship between density and phase. Then, the measurement principle of the interferometer and two interferometer configurations, Michelson interferometer and Mach-Zehnder interferometer, which are commonly used in fusion devices are introduced. Finally, the detection principle and derivation process of heterodyne, which is used for interferometer detection signal, are summarized.

In chapter 3, the magnetic field configuration, auxiliary heating system and diagnostics of Heliotron J are presented. Auxiliary heating systems on Heliotron J such as neutral beam injection (NBI) and electron cyclotron resonance heating (ECH) are summarized. The fueling methods to enhance plasma density, such as gas-puffing, SMBI, HIGP and pellet injection, are introduced and the principle of enhancing plasma density is briefly analyzed. Finally, a brief summary of plasma diagnostic tools on Heliotron J is presented.

In chapter 4, the new 320 GHz interferometer system in Heliotron J is overviewed. Firstly, the interferometer system developed in Heliotron J is introduced, and the issues are shown, which motivates of the development of the new interferometer system. Secondly, the process of the design and construction of the new interferometer is presented, along with details of the individual optical transmission components and the corresponding tabletop test results, which are given for the construction of the single-channel interferometer. Finally, the problems encountered in the design and construction of the single-channel are analyzed. A new optical path design is used to solve the problem of low beam transmission efficiency, and an off-axis parabolic mirror is designed and built to extend the single channel with a sheet beam to realize multi-channel measurements.

In chapter 5, the principle of the retroreflector array is summarized and assessed its usefulness as the reflector for interferometer measurement. A retroreflector array, composed of a cluster of small retroreflectors, is experimentally studied for the application to a Michelson-type interferometer system in fusion plasma experiment. Such a new-type reflector has the potential to be a vital and effective tool at a spatially limited location such as on the vacuum chamber wall of plasma experimental devices. To investigate the effect of retroreflector-array on the reflected beam properties, a tabletop experiment is performed with the retroreflector array. An imaging camera is utilized to measure the submillimeter wave beam profile. The experimental result exhibits that diffraction effect on the reflected beam, the most reflected beam power converges on the

one reflected into the incident direction, showing the property as a retroreflector. A focusing lens placed at the front of the detector in the practical application to an interferometer, which improves the quality and intensity of the beam, and compensate the beam displacement induced by the grating effect, demonstrating that the retroreflector array can be used for the Michelson-type interferometer in the fusion plasma experiment.

In chapter 6, the measurement results of the electron density with the new interferometer system are summarized. The single-channel 320 GHz interferometer was constructed and operated as commissioning during the 2021 plasma experiment campaign. After employing a new transmission optical path and OAP system, the beam was extended to a sheet beam to realize multi-channel measurements, and density measurements of two channels were obtained in the plasma experiment.

In chapter 7, summary of this dissertation is given.

Contents

Chapter 1

1. Introduction

1.1 Background

Recent climate changes have had widespread impacts on human and natural systems, with the major contributor being the extensive release of greenhouse gases as a result of human activities [1]. The rise in global temperature as shown in Fig. 1.1, which is a direct outcome of human-induced climate change [2]. The emission of greenhouse gases since the era of human industrialization is the main influence on the increase of global temperature. The massive use of fossil fuels such as coal and oil for power and electricity required for industrialization has led to unprecedented greenhouse gas emissions, bringing about an increase in global temperatures and causing global climate change in recent years. The greenhouse gases released by humans in the last half century and their composition are shown in Fig. 1.2 [1]. Cumulative emissions of carbon dioxide largely determine global mean surface warming by the late 21st century and beyond. To mitigate climate change caused by rising temperatures, countries around the world have begun acting. As of early 2022, nearly three-quarters of the world's global greenhouse gas emissions are covered by a net-zero law, policy or political pledge, identifying a method of reducing carbon dioxide that can be implemented along with social development has become a focus of the international community [2].

To achieve net-zero carbon emission, the most direct way is to replace fossil energy with new energy, as shown in Fig. 1.3, since the fossil fuel emits most of the carbon dioxide [1,3,4]. The governments around the world vigorously develop new energy sources represented by wind, solar and nuclear energy [5,6]. However, wind and solar

energy sources are susceptible to environmental conditions and have lower energy densities compared to traditional sources, making them less reliable. Nuclear energy, with its high energy density, is widely regarded as the most promising source of energy to achieve the goal of carbon neutrality.

The first nuclear power plant was built in 1954 and humanity begins to peacefully apply nuclear energy [7]. Over the past 70 years, three major nuclear accidents have occurred, sparking public concerns about the safety and use of nuclear energy, as well as issues related to nuclear safety and waste disposal. These concerns have led some countries to abandon nuclear power. To reduce greenhouse gas emissions and reverse the impact of environmental change on the Earth, people are focusing on nuclear fusion research to reduce the environmental impact and achieve the ultimate energy source for the future.

Human research on the use of fusion energy began in the 1920s with the study of fusion reactions on planets in the universe. Fusion is the process that nuclei of lighter atoms such as hydrogen collide and fuse to produce nuclei of heavier atoms such as helium and release vast amounts of energy($E=mc^2$) [8]. The most common fusion reaction comes from the sun. The sun's enormous gravitational force confines the positively charged hydrogen nucleus, and the extremely high temperature inside causes the hydrogen to transform into a plasma state and move at high speed, overcoming the natural electrostatic repulsion to collide at high speed, fusing to form heavier helium and releasing huge amounts of energy [9]. However, fusion reactions cannot be achieved on Earth by similar means, and a series of ways to confine the plasma and heat it to 150 million degrees Celsius have been developed to achieve nuclear fusion reactions on Earth. Because hydrogen isotopes such as deuterium-tritium have a large reaction cross-section, and deuterium can be obtained indefinitely from seawater, tritium can be obtained by multiplication (Eq. 1.1, 1.2), which makes the D-T reaction more suitable for achieving fusion on Earth. The reaction equation for the deuterium-tritium reaction is given in. Eq (1.3). The cross-section for the reactions of D-T,D-D and D-He^3 are shown in Fig. 1.4. [10].

Magnetic confinement, as one of the most reliable ways to achieve confined plasma on Earth, uses a magnetic field to confine the high temperature plasma in a certain region to achieve control and maintenance of the burning plasma. Many different methods of magnetic confinement have been developed around the world, mainly its typical representatives are tokamak and stellarator.

Tokamaks were developed by the Soviet Union in the 1950s and their name is a Russian acronym derived from toroidal, kamera, magnit and kotushka [11]. In a tokamak, a polar magnetic field is generated by a toroidal plasma current, and an external coil is used to generate a toroidal magnetic field, both eventually produce a spiral magnetic field, thus confining the plasma within the vacuum chamber. The typical discharge process in a tokamak is based on the establishment of a stable and sufficiently strong toroidal magnetic field, followed by the pre-ionization of the neutral gas in a vacuum chamber, and then the induction of a toroidal current by an external transformer coil. After this, the fusion reaction is achieved by continuously increasing the temperature of the plasma through external heating systems such as neutral beam injection (NBI) systems and RF heating systems. After the presentation of the experimental results of the tokamak device T-3 at the Novosibirsk conference in 1968 [12,13], the tokamak began to develop significantly, and the realization of H-mode operation at ASDEX in Germany in 1982 marked a new stage in the physical research of tokamaks[14]. Many new tokamaks have been developed since then, and the breakthrough of Q=1.25 (the out-versus-in power amplification ratio of the fusion reaction) was achieved at JT-60U in Japan, demonstrating the realizability of fusion research [15]. To enable plasma self-sustaining combustion while testing the necessary technology for fusion reactors and the effectiveness of tritium multiplication, 35 countries are collaborating to build the world's largest tokamak, a magnetic fusion device designed to demonstrate the viability of fusion as a large-scale and carbon-free energy source [16].

ITER has been designed to realize :

1) Achieve a deuterium-tritium plasma in which the fusion conditions are sustained mostly by internal fusion heating

2) Generate 500 MW of fusion power

3) Contribute to the demonstration of the integrated operation of technologies for a fusion power plant

4) Test tritium breeding

5) Demonstrate the safety characteristics of a fusion device

The stellarator/heliotron was from Prof. Spitzer’s pioneering work of Figure-8

stellarator in the 1950s [17]. In a stellarator, there is no or not necessarily an overall circulating current, but instead, on an external coil to generate a polar magnetic field that moves the charged particles along synthetic spiral magnetic lines of force, eliminating drift-induced charge separation. The stellarator/Heliotron is less subject to effects such as disruptions, which relate to the large plasma current [18]. Compare with the tokamaks, the stellarators/ Heliotron have the significant operational advantages as ignited steady-state reactors. After the IAEA Conference in Geneva in 1958, the stellarator research was extended to Germany, Japan, USSR and UK [18]. The new stellarator/heliotron device had been designed and operated in Heliotron E [19], Compact Helical System (CHS) [20], Large Helical Device(LHD, Japan)[21] and Wendelstein7-AS (W7-AS,Germany) [22]. To achieve the high-energy particle confinement and obtain the good particle transport with MHD stability for the stellarator/heliotron plasmas, Heliotron J introduce of a helical axis heliotron configuration.

1.2 Previous study of interferometer system

Interferometry is the utilization of the phenomenon of interference in electromagnetic waves to achieve precise measurements [23]. To make measurements using interference, optical configurations in which two or more beams propagate along different paths are usually used [24]. The most common type of interferometer is a two-beam interferometer, where one beam is used as a probe or test beam through the measurement medium, and the other is used as a reference beam [25]. Eventually, the two separate beams combine, forming an interference pattern. The propagation of the probe beam is affected by the transmission medium due to the differing paths of the two beams [26]. The resulting pattern offers valuable information about the characteristics of the probe beams, such as their phase, amplitude, or wavelength, enabling precise measurements with the interferometer.

Interferometry has served as a laboratory measurement technique for almost a century [23]. Over time, with advancements in wave source technology, particularly in lasers and terahertz technology, the applications of interferometry have significantly expanded. Today, interferometers are extensively utilized for precise measurements of distance, displacement, and vibration. They are also employed in optical system testing and plasma diagnostics [27].

The interferometer is a widely adopted technique for measuring electron density in

magnetically confined plasma [28]. In comparison to other density diagnostics, interferometers offer several advantages, including high temporal resolution and the absence of calibration requirements. As a result, they are extensively utilized in various types of magnetically confined devices. The Large Helical Device (LHD) is equipped with five different interferometer systems to measure different density ranges and achieve different experimental purposes, enabling accurate measurements covering densities such as 10^{18}-10^{21} m^{-3} in the LHD [29]. In HL-2A, a medium-sized tokamak, the multi-channel far-infrared interferometer, is used as a routine diagnostic for plasma density and density perturbations [30]. A multichannel interferometer system with nine channels is routinely operating on the quasi-helically symmetric experiment (HSX) to measure the equilibrium profile and electron density dynamics [31].

1.3 Research motivation and objectives

Understanding high-density plasmas through advanced fueling techniques is crucial to realize better plasma confinement. Increasing the plasma density, which is beneficial for energy confinement, makes the measurement and analysis of plasma density very important. The plasma density and density distribution are important parameter for the study of plasma and data analysis. The effective and precision measurement of the electron density is crucial for the plasma control and physics study in the magnetically confined fusion plasma devices.

In Heliotron J, several fueling techniques, such as pellet injection, supersonic molecular beam injection (SMBI), and short-pulsed high-intensity gas puffing (HIGP), can help achieve high-density plasma [32, 33, 34, 35]. The interferometer measurement is a standard technique used to measure the electron density of a magnetically confined plasma [28]. A single-channel 135 GHz microwave interferometer and a single-channel hydrogen cyanide (HCN) laser interferometer has been developed in Heliotron J [34,35]. However, the access density of the 135 GHz microwave interferometer is limited to 2×10^{19} m^{-3} due to the fringe jump caused by refraction in higher density; the routine operation requires a significant effort for the maintenance and operation of the HCN laser.

The objective of this study as follows: Develop a new multi-channel interferometer using submillimeter wave sources and operation stability for the study of high-density and high-performance plasmas. The electron density measurement serves as the fundamental parameter for understanding the plasma confinement and particle transport

in a stellarator. It provides crucial information regarding both the electron density distribution and density fluctuations within the plasma.

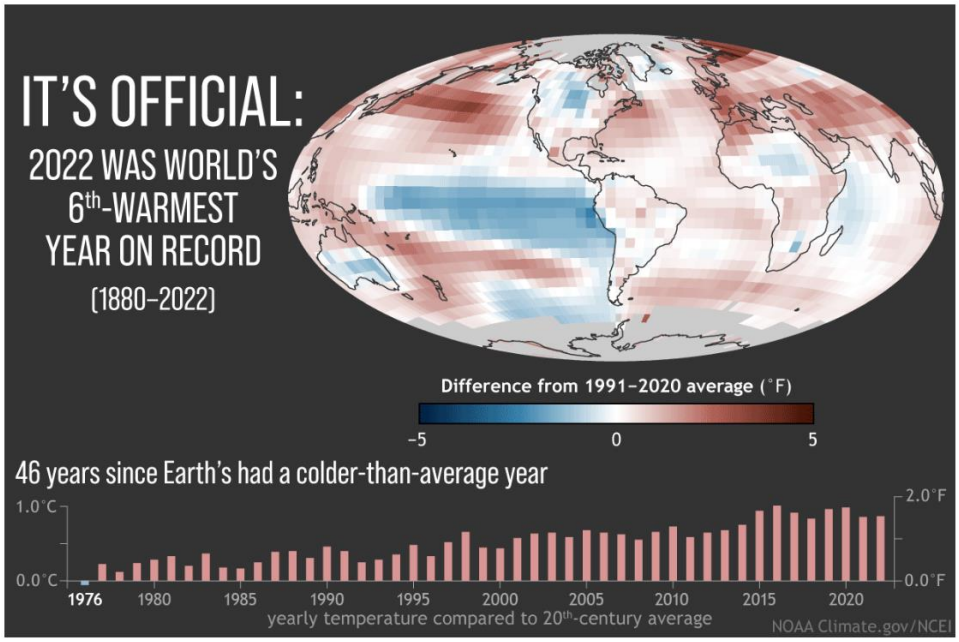

Fig. 1.1 (map) Global average surface temperature in 2022 compared to the 1991-2020 average, red is the places that were warmer than average, blue is the places that were cooler than average. (graph) The bars on the graph show global temperatures compared to the 20th-century average each year from 2022 (right) back to 1976 (left)–the last year the world was cooler than average [2].

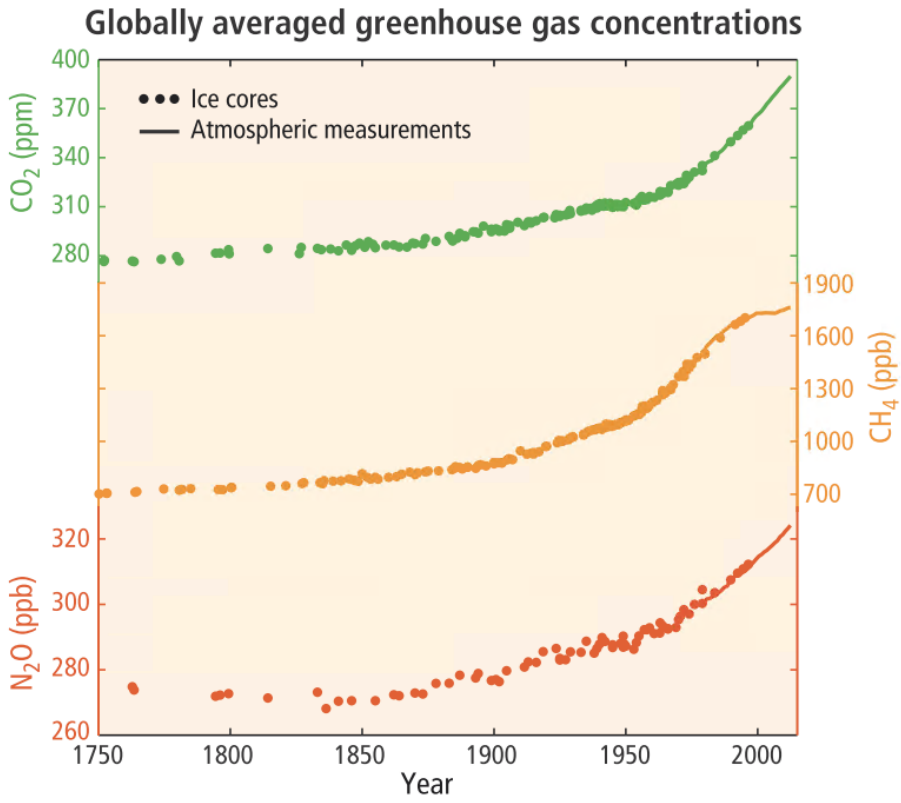

Fig. 1.2 Observed changes in atmospheric greenhouse gas concentrations. Atmospheric concentrations of carbon dioxide (CO_2, green), methane (CH_4 , orange), and nitrous oxide (N_2O, red). Data from ice cores (symbols) and direct atmospheric measurements (lines) are overlaid [1].

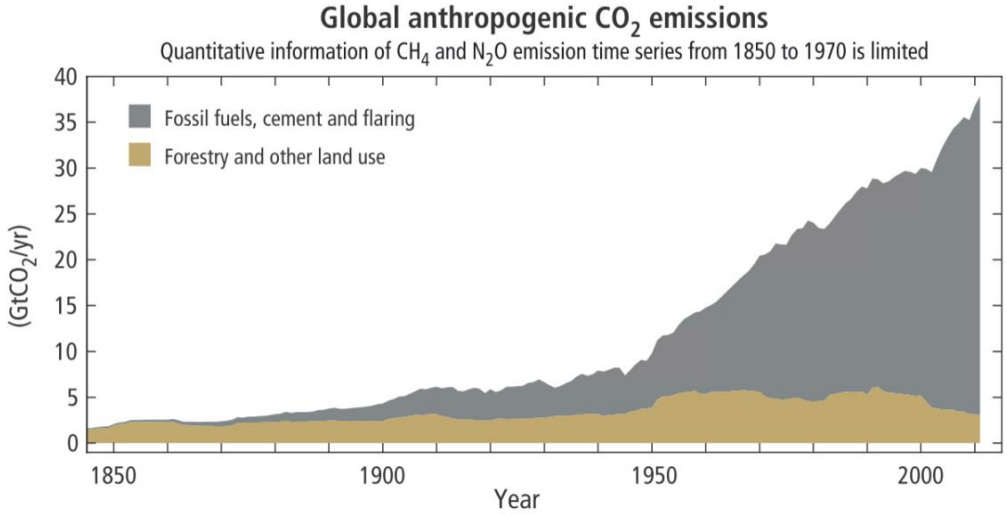

Fig. 1.3 Global anthropogenic CO_2 emissions from forestry and other land use as well as from burning of fossil fuel, cement production and flaring [1].

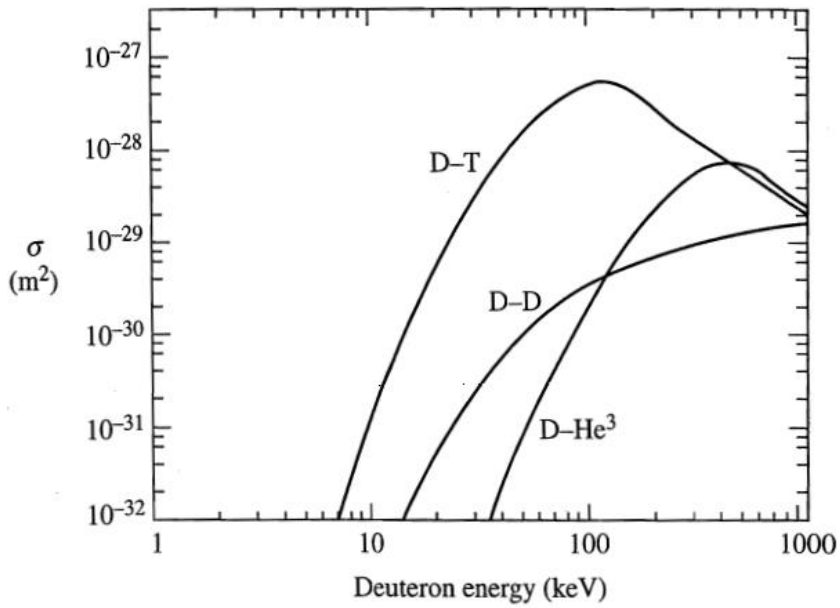

Fig. 1.4 Cross-sections for the reactions of D-T,D-D and D-He_3 [10].

Chapter 2

2. Principle of interferometer measurement

The plasma electron density is one of the most essential and important plasma parameters [36]. The effective measurement of the electron density is crucial for the plasma control and data analysis in the magnetically confined fusion plasma devices [29]. The interferometer measurement is a standard technique used to measure the electron density of a magnetically confined plasma [28]. Due to its advantage of obtaining reliable measurements, the interferometer can be used to research plasma transport and density fluctuation [37]. The principle for plasma interferometer will be described in this chapter.

2.1 Propagation of electromagnetic waves in plasma

Interferometry is a diagnostic method that measures the plasma electron density by detecting the change in phase before and after the transmission of electromagnetic waves in a plasma. Compared to other plasma diagnostics such as Langmuir probes, the influence of electromagnetic waves on the plasma is negligible, while the change of the refractive index of the plasma can be accurately detected, so that various parameters inside the plasma can be finally determined [26].

Considering the speed of the waves travelled in the plasma close to the light in plasma. Therefore, the thermal particle motions can be ignored, and we call this cold plasma approximation. The equation of motion of a single electron as follows:

$$m_e \frac{\partial \boldsymbol{v}}{\partial t} = -e(\mathbf{E} + \boldsymbol{v} \times \mathbf{B_0}) \tag{2.1}$$

Where $\boldsymbol{v}$ is $\propto \exp(iwt)$, $\mathbf{B_0}$ is the static magnetic field and ignore collisions. We just take the z axis in the direction $\mathbf{B_0}$. The solution for v can be shown as:

$$v_x = \frac{-ie}{\omega m_e}\frac{1}{1-\frac{\Omega^2}{\omega^2}}\left(\mathrm{E}_x - i\frac{\Omega}{\omega}\mathrm{E}_y\right) \tag{2.2}$$

$$v_y = \frac{-ie}{\omega m_e}\frac{1}{1-\frac{\Omega^2}{\omega^2}}\left(\mathrm{E}_y + i\frac{\Omega}{\omega}\mathrm{E}_x\right) \tag{2.3}$$

$$v_z = \frac{-ie}{\omega m_e}\mathrm{E}_z \tag{2.4}$$

where $\Omega = eB_0/m_e$ is the electron cyclotron frequency. In this cold plasma, the current density can be shown as:

$$\mathbf{j} = -en_e\mathbf{v} = \sigma \cdot \mathbf{E} \tag{2.5}$$

We can obtain the conductivity tensor:

$$\boldsymbol{\sigma} = \frac{ie^2 n_e}{\omega m_e}\frac{1}{1-\frac{\Omega^2}{\omega^2}}\begin{bmatrix} 1 & -i\Omega/\omega & 0 \\ i\Omega/\omega & 1 & 0 \\ 0 & 0 & 1 - -i\Omega/\omega \end{bmatrix} \tag{2.6}$$

As the $m_i \gg m_e$, the ion contribution may be ignored.

The relation between dielectric tensor and conductivity as follows:

$$\boldsymbol{\epsilon} = \left(1 + \frac{i}{\omega\varepsilon_0}\right)\sigma \tag{2.7}$$

The dielectric tensor can be written as:

$$\boldsymbol{\epsilon} = \begin{bmatrix} 1 - \frac{\omega_{pe}^2}{\omega^2-\Omega^2} & \frac{i\omega_{pe}^2\Omega}{\omega(\omega^2-\Omega^2)} & 0 \\ \frac{-\omega_{pe}^2\Omega}{\omega(\omega^2-\Omega^2)} & 1 - \frac{\omega_{pe}^2}{\omega^2-\Omega^2} & 0 \\ 0 & 0 & 1 - \frac{\omega_{pe}^2}{\omega^2} \end{bmatrix} \tag{2.8}$$

where ω_{pe} is the electron frequency and ω the probing wave frequency.

$$\omega_{pe} = \left(\frac{n_e e^2}{\varepsilon_O m_e}\right)^{1/2}, \tag{2.9}$$

To use the electromagnetic waves as the probe into the plasma and measure the

refractive index of the plasma, it is necessary to consider the case of a homogeneous magnetic plasma in which the motion of ions and the thermal velocity of electrons are negligible. The frequency of the probe beam is higher than the plasma frequency. The relation of them is as follows [26,38].

$$\omega_{pe} < \omega, \tag{2.10}$$

The refractive index N of the plasma can be expressed as the Appleton-Hartree formula under these plasma conditions. With the refractive index of plasma, the parameters of the interior plasma can be obtained. The refractive index *N* as follows:

$$N^2 = 1 - \frac{X(1-X)}{1-X-\frac{1}{2}Y^2\sin^2\theta \pm \left[\left(\frac{1}{2}Y^2\sin^2\theta\right)^2 + (1-X)^2Y^2\cos^2\theta\right]^{1/2}}, \tag{2.11}$$

where $X = ({\omega_{pe}}^2/\omega^2)^{1/2}$, $Y = \omega_{ce}/\omega$, $\omega_{ce} = eB/m_e$ is the cyclotron frequency of the electron, B is the magnetic field, θ is the incident wave vector **k** and the angle of **B** (**k**, **B** are vectors), and n_e is the electron density, and ε_O is the dielectric constant in vacuum, and m_e is the mass of electrons.

For the waves that electric field E direction perpendicular to the magnetic field B (extraordinary waves), the solution is :

$$N = \left[1 - \frac{\frac{\omega_{pe}^2}{\omega^2}}{1 \pm \frac{\Omega}{\omega}}\right]^{1/2}, \tag{2.12}$$

For waves that are polarized with its electric field E parallel to the magnetic field B (ordinary waves) and traverse the plasma normal to the magnetic field direction of plasma, the refractive index of the plasma can be given as:

$$N = \left[1 - \frac{\omega_{pe}^2}{\omega^2}\right]^{1/2}, \tag{2.13}$$

If the probe beam passes through a plasma of thickness ΔZ, then the reference beam that does not pass through the plasma has a phase difference with the probe beam of

$$\varphi = \frac{2\pi}{\lambda} \int_{Z_1}^{Z_2} [N_0 - N(Z)]\, dZ, \tag{2.14}$$

where N_0 is the refractive index in vacuum N_0= 1 and Z_1- Z_2 is the distance passed through the plasma.

The refractive index can be approximated when $n_e \ll n_c$ as:

$$N \cong 1 - \frac{1}{2}\frac{\omega_{pe}^2}{\omega^2} = 1 - \frac{1}{2}\frac{n_e}{n_c}. \tag{2.15}$$

where the n_c is the cutoff density for the probe beam in the plasma. When the density of plasma $n_e > n_c$, the probe beam cannot pass through the plasma. Combining Eq. (2.9) and Eq. (2.15), we can express Eq. (2.14) as follows:

$$\varphi = \frac{e^2}{4\pi c^2 \varepsilon_O m_e} \lambda \int_{Z_1}^{Z_2} n_e(Z)\, dZ. \tag{2.16}$$

For a constant density along concentric circles of the cross-section, we can obtain the density of the plasma $n_e(r) = -\lambda n_c/\pi^2 \int_r^{r_0} [d\varphi(Y)/dY][dY/(Y^2 - r^2)^{1/2}]\, dZ$ from Eq. (2.14), as shown in Fig. 2.1 [38]. Interferometry is the primary diagnostic method for measuring internal plasma parameters using electromagnetic wave propagation in the plasma.

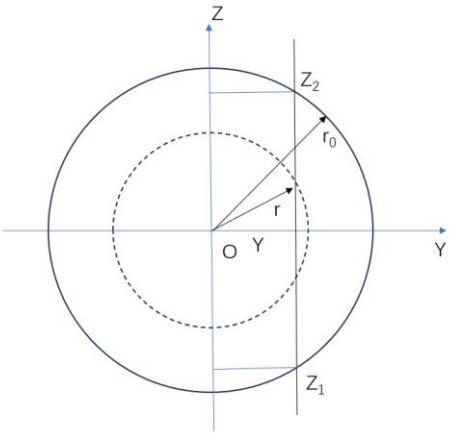

Fig. 2.1 The phase shift along a chord in the concentric [38].

2.2 The principle of interferometer

The interferometer is a device using the phenomenon of interference of waves to realize the measurement. Since the wavelength of probe beam in the measured medium is quite small (in our case around 1mm), very small changes in the optical path difference produce measurable changes in the intensity of an interference pattern. The interferometer

permits extremely accurate measurements in plasma [23]. For the interferometer system, the propagation of a fixed frequency probe beam through air and plasma produces an optical path difference, which is proportional to the phase difference, and we can obtain information of the plasma electron density by comparing the phase difference signals of the probe and reference beams.

2.2.1 Types of Interferometers

To enable measurements using interference, the interferometer system consists of an optical arrangement in which two beams traveling along separate paths are made to interfere, one as the probe beam propagating the plasma, the other is the reference beam. The beam splitter is the common method to be used to make the division of amplitude to produce two beams. The typical systems of the two beams interferometers are the Mach–Zehnder interferometer and Michelson interferometer [25].

A Mach–Zehnder interferometer

The schematic diagram of the Mach–Zehnder interferometer is shown in Fig. 2.2. The system consists of two sets of beam splitters and two sets of plane mirrors. The probe beam is split into two beams after the first beam splitter, one as the probe beam through the plasma and one as the reference beam reflected from the two plane mirrors. The reference beam is always transmitted in air, maintaining the original phase. The probe beam passing through the plasma undergoes a phase change and eventually interferes with the reference beam, allowing information such as the plasma density to be obtained.

The most important feature of the Mach–Zehnder interferometer is that it passes through the measured medium plasma at once. The density of the plasma causes the probe beam to shift the initial propagation direction. As can be seen from the previous section, when the density gradient inside the plasma is large, the initial degree of beam shift increases, resulting in large errors for the detection of higher density plasmas.

B Michelson interferometer

The schematic diagram of the Michelson interferometer is shown in Fig.2.3. The system consists of a set of beam splitter and two plane mirrors, which is more compact compared to the Mach–Zehnder interferometer. The beam from the source is divided into two parts by the beam splitter, one as a probe beam passing through the plasma with a change in phase and the other as a reference beam changing the propagation direction.

These two beams, after reflecting in their respective directions, reach the beam splitter and combine to realize a interference pattern.

The Michelson interferometer passes through the plasma twice, which makes its structure more concise. This also makes the Michelson interferometer more suitable for installation in spatially compact fusion devices. For the offset caused by the high-density plasma, the offset of the probe beam is compensated for by using measures such as retroreflector to return it in the original path.

Because the Mach–Zehnder interferometer need more optical components than the Michelson-type interferometer. It will make the interferometer system more complex especially with multichannel case. And the probe beam only passes through the plasma one time, it will need more diagnostic window and space around Heliotron J. Finally, we chose the Michelson-type as the configuration of our new interferometer system.

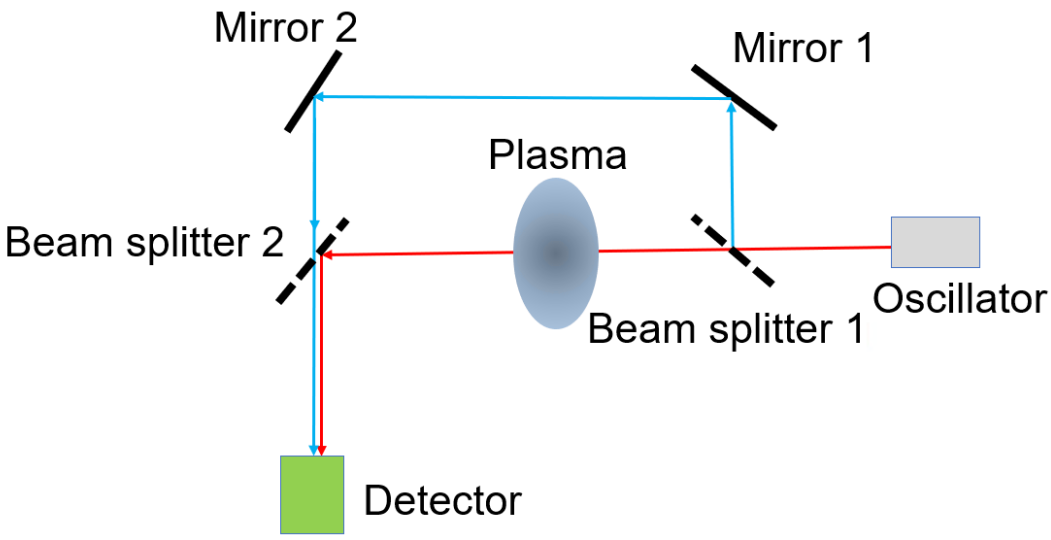

Fig. 2.2 The schematic of Mach–Zehnder Interferometer.

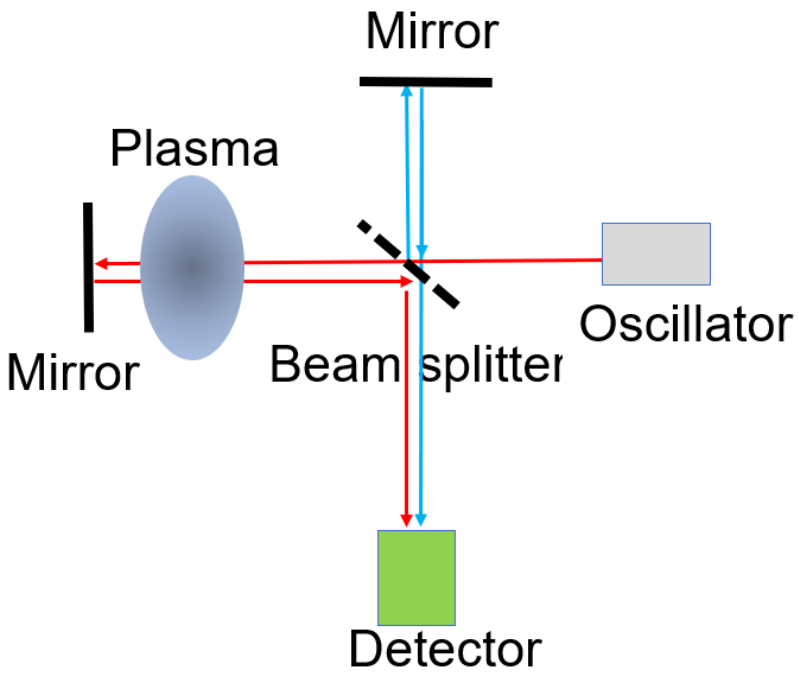

Fig. 2.3 Schematic of Michelson Interferometer.

2.2.2 The principle of heterodyne detection

The heterodyne technique is a commonly used electron density measurement method that uses frequency modulation techniques to convert the phase shift of the probe beam in the plasma to a low-frequency sinusoidal signal phase change, and then calculates the plasma electron density based on the phase change [39]. This subsection focuses on the principle of the heterodyne method for the Michelson interferometer signals.

For a fixed frequency probe beam, after passing through the plasma, the phase will change due to the optical path difference caused by the plasma, and for its amplitude before and after transmission in the plasma. we can show respectively as

$$E_L = A\cos(\omega t) \tag{2.17}$$

$$E_P = A\cos(\omega t + \varphi) \tag{2.18}$$

where E_L is local beam, E_P is probe beam. φ is the phase difference produced by the plasma. When the two beams are combined, the power detect is proportional to $(E_L + E_P)^2$ and φ measurement can be deduced from the $ab\cos(\varphi)$ term. However, this method cannot determine the sign of φ and is sensitive the change in amplitudes.

These difficulties can be overcome by making the system a heterodyne type [39].

The amplitudes of the probing beam and local beam (reference beam) can be represented with

$$E_L = A\cos(\omega + \Delta\omega)t \ , \tag{2.19}$$

$$E_P = B\cos(\omega t) \ , \tag{2.20}$$

The fixed beat frequency is $\Delta\omega$.

The probe beam without passing through the plasma is combined with the local beam into detector 1 and the output signal is:

$$S_R = [A\cos(\omega t + \Delta\omega)t + B_1\cos(\omega t)]^2, \tag{2.21}$$

The probe beam passing through the plasma beam is combined with the reference beam into detector 2 and the output signal is:

$$S_P = [A\cos(\omega t + \Delta\omega)t + B_2\cos(\omega t + \varphi)]^2, \tag{2.22}$$

Expanding the output signals of the two detectors, we can obtain:

$$S_R = A^2\cos^2(\omega t + \Delta\omega)\,t + {B_1}^2\cos^2(\omega t) + AB_1[\cos(2\omega + \Delta\omega)t + \cos(\Delta\omega t)] \tag{2.23}$$

$$S_P = A^2\cos^2(\omega t + \Delta\omega)\,t + {B_2}^2\cos^2(\omega t + \varphi) + AB_2\{\cos[(2\omega + \Delta\omega)t + \varphi]\} + \cos(\Delta\omega t - \varphi)] \ , \tag{2.24}$$

In the practical measurements, the detector detects only the low-frequency part of the signal, so we only study the term (2.23) and the last cos of (2.24). The low-frequency signal can be expressed as

$$S_R = AB_1\cos(\Delta\omega t) \ , \tag{2.25}$$

$$S_P = AB_2\cos(\Delta\omega t - \varphi) \ , \tag{2.26}$$

By using the $\Delta t = t_1 - t_2$, at the zero-crossing point of Eq. (2.27) and (2.20) the measurement of the phase difference caused by the plasma can be determine:

$$\cos(\Delta\omega t_1) = \cos(\Delta\omega t_2 - \varphi) \ , \tag{2.27}$$

$$\Delta\omega t_1 = \Delta\omega t_2 - \varphi, \tag{2.28}$$

$$\varphi = \Delta\omega\Delta t, \tag{2.29}$$

where Δt is independent of the signal and the time resolution is equal to the period of the beat signal. For a heterodyne interferometer, the beat frequency is an important element as it determines the time resolution of the interferometer. High temporal resolution of electron density needs a high beat frequency signal [39,40].

2.3 Application of interferometer to fusion devices

The electron density distribution is important for the plasma research. Interferometer systems have been established as a basic diagnostic tool for the measurement of plasma electron density in various fusion devices including tokamaks and stellarator/heliotron [41].

In the Large Helical Device (LHD), five interferometer system with different sources and designs have been improved to cover the electron density range during different operational purpose. The features of interferometers in LHD are shown in table 2.1 [29].

The millimeter with solid state sources is used for the density monitoring in the density range less than ~5 $\times 10^{19} m^{-3}$. The layout of the millimeter interferometer in LHD is shown in Fig. 2.4. This interferometer is a Mach–Zehnder interferometer with a view chord in the horizontal midplane to minimize the refractive effects caused by the density gradient. Two solid-state sources provide the 140 and 285 GHz millimeter wave to compensate the changes in the long path length [29].

The CH_3OH laser interferometer with 13 channels has been developed for the electron density profile. As the main interferometer on LHD with the measurement of temporal behavior, it is used for feedback control of the electron density. Fig. 2.5 show the schematic of the FIR interferometer. A 119μm CH_3OH laser was chosen as a probe light. The optical configuration is of the Michelson interferometer type with 13channels, which cover almost the entire poloidal cross section [42]. Fig .2.6 shows an example of

line-averaged density and the reconstructed density profiles of a pellet injection plasma.

In the HL-2A, the medium-sized tokamak, a four chords hydrogen cyanide (HCN, λ = 337 μ m) laser interferometer the routine diagnostics to achieve the information of electron density. Two HCOOH laser sources were employed to produce high intermediated frequencies up to 3.0 MHz for the heterodyne detection to measure the fast electron density variation and fluctuations. As shown in Fig. 2.7, the configuration of this interferometer is a Michelson type interferometer with a reflector in the wall of vacuum chamber. To compact the system and reduce the optical components, the orthogonally collinear wave transmission and separation method was adopted in the interferometry system. "⊗" means the polarization direction perpendicular to the paper-plane, and "↕" means the polarization direction parallel to the paper plane [30]. The density with four chords were show in Fig. 2.8. During neutron beam injection (NBI,P = 0.8 MW) and electron cyclotron resonance heating (ECRH, P = 0.8 MW) plasma, and the plasma enters the H-mode from the L-mode since ~520 ms, featuring with the ELM bursts. The four chords can show the evolution of the electron density, the electron density profile becomes peaking and then recovers flattening.

A high-resolution interferometer with nine channels has been installed in the helically symmetric experiment (HSX), a new concept in toroidal stellarators, to measure the equilibrium electron density distribution and its response to perturbations provides important information to magnetically confined plasma research. The schematic of the interferometer system is shown in Fig. 2.9. The parabolic mirrors produce the sheet beam cover the plasma section from the outboard side scrape-off layer to well past the magnetic axis to make the configuration of a Mach–Zehnder Interferometer. A solid-state source provides 288GHz millimeter wave as the probing beam [43]. Fig. 2.10 shows the typical line-integrated densities of the nine channels from the interferometer system during the ECH plasma.

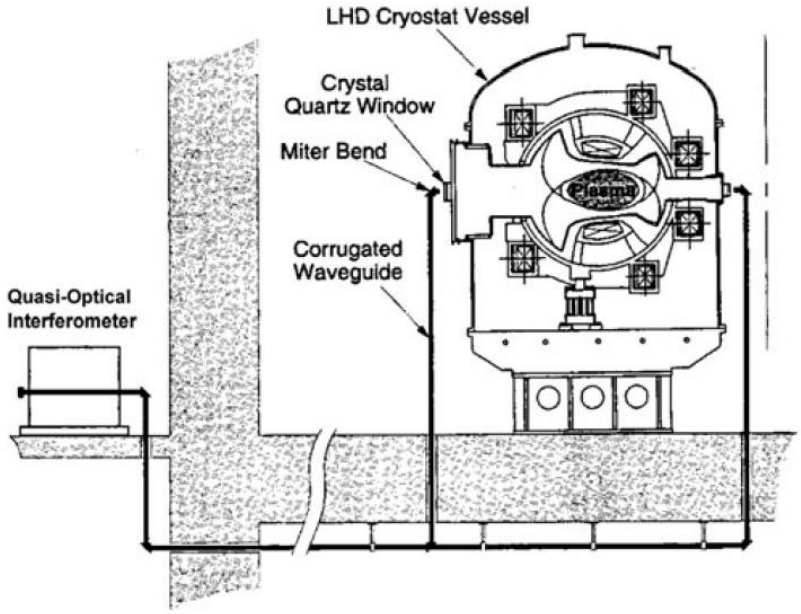

Fig. 2.4 The schematic of millimeter interferometer system in LHD [29].

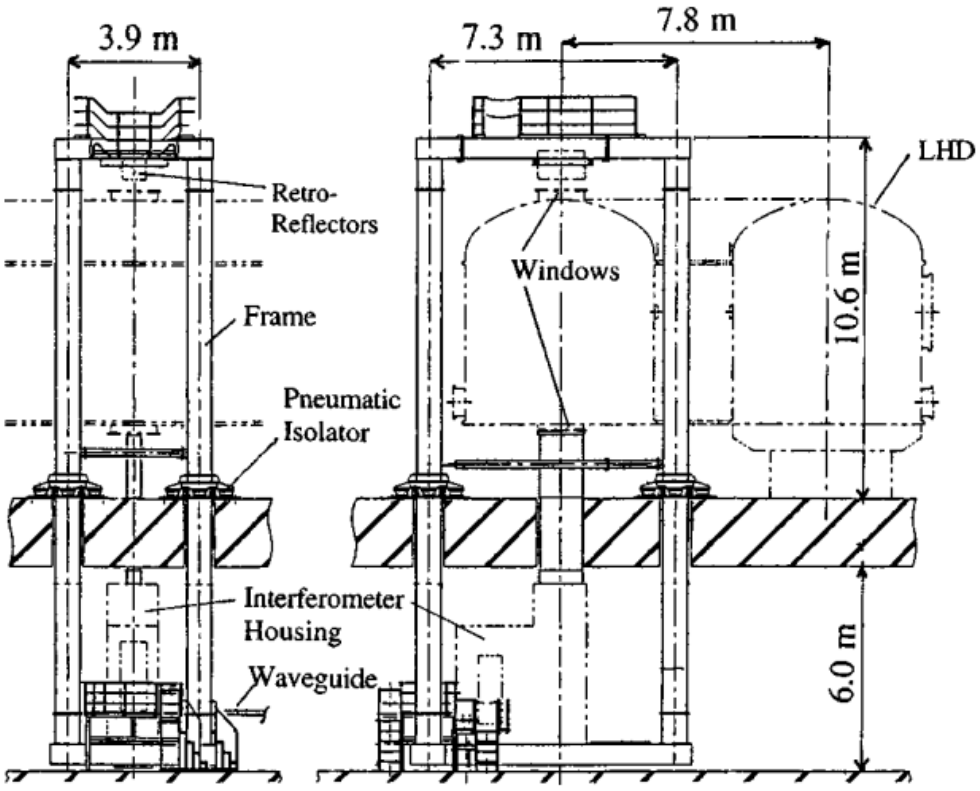

Fig. 2.5 The schematic of FIR interferometer system in LHD [42].

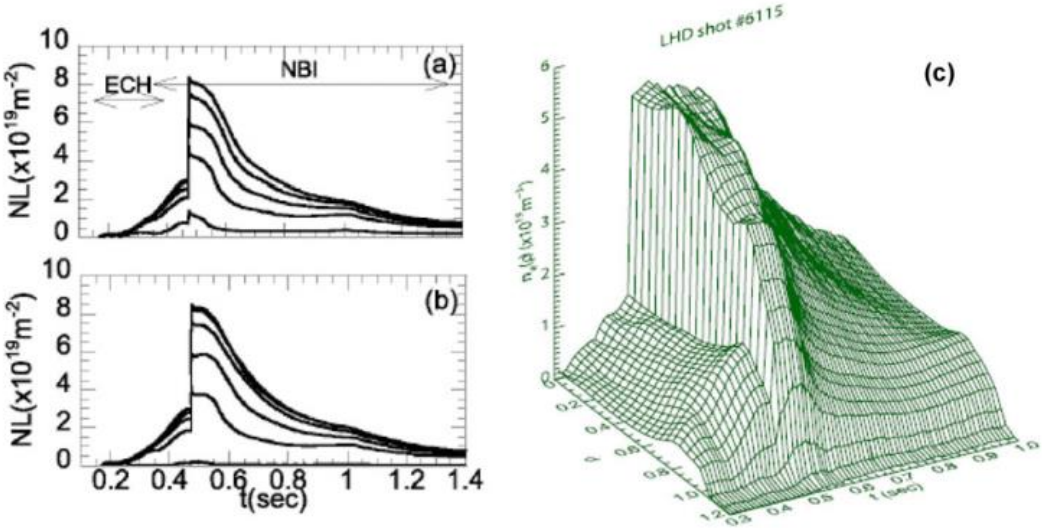

Fig. 2.6 (a) and (b) Temporal behaviors of line integrated densities. (c) Reconstructed density profiles measured with the CH_3OH laser interferometer [29].

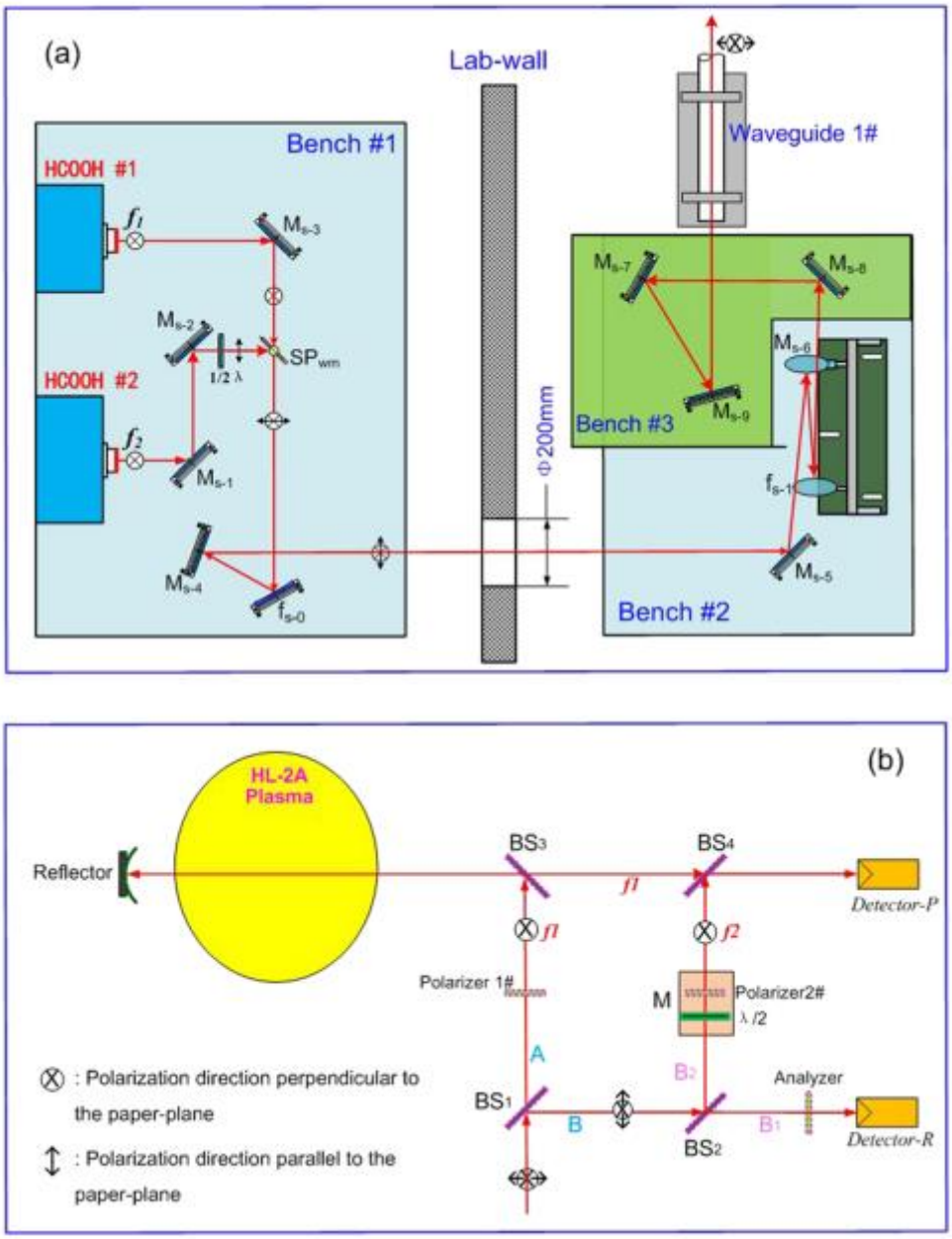

Fig. 2.7 The schematic of FIR interferometer system in HL-2A [30].

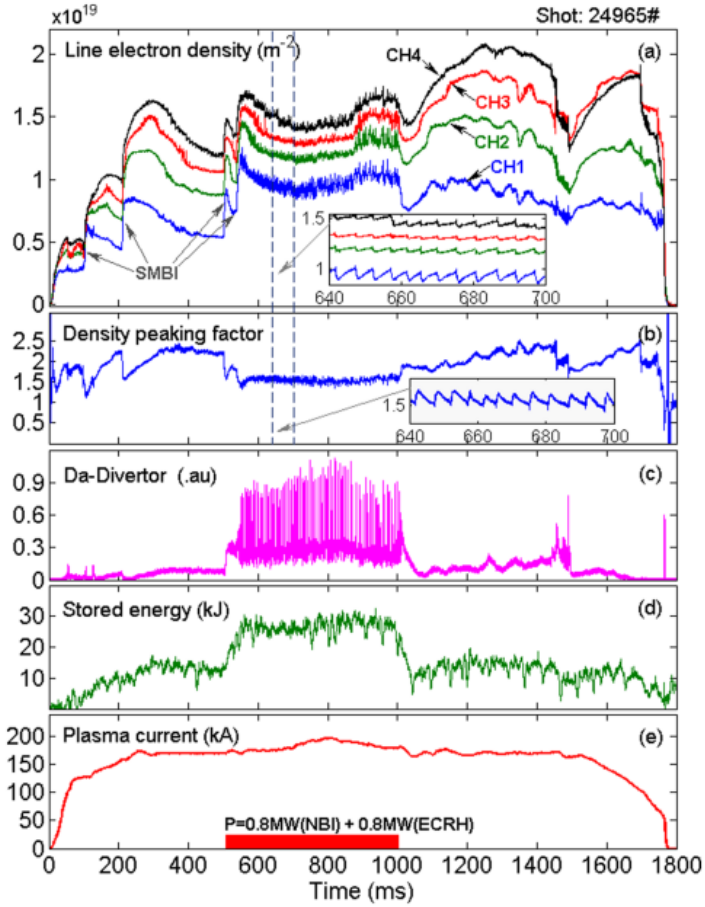

Fig.2.8 Time evolution of the line electron densities measured by the four-chord HCOOH laser interferometer; in this discharge, 4 SMBI pulses were injected, and plasma confinement performance transformed to H-mode from L-mode during NBI and ECRH, (b) electron density peaking factor which was estimated by neL4/neL1, (c) Da radiation, (d) stored energy, and (e) plasma current and heating power [30].

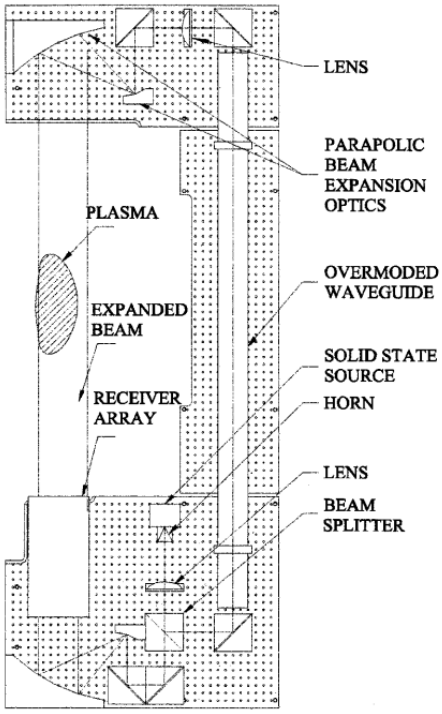

Fig.2.9 Schematic of HSX interferometer system optical layout [43].

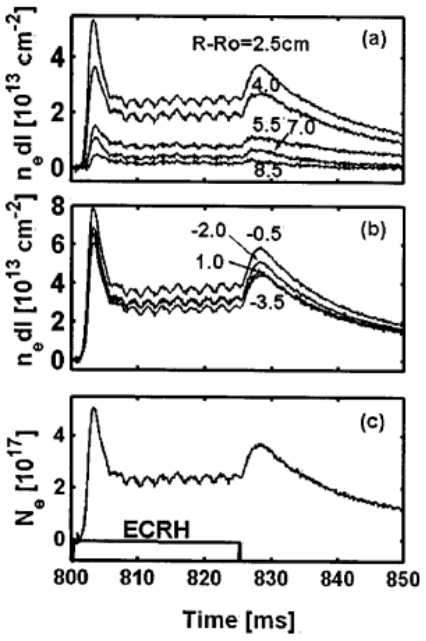

Fig. 2.10 (a) , (b)Line-integrated density time traces from digital phase comparator; (c) total number of electrons for a QHS discharge with 50 kW ECRH from 800 to 825ms [31].

Table2.1 The interferometer system on LHD [29]

Interferometer	Characteristics	Density and Time Resolutions	Purpose
Millimeter	140 and 285 GHz, single channel, Mach-Zehnder	3.1 × $10^{15}$$m^{-3}$ (140 GHz)and 6.3×10^{15} m^{-3} (285 GHz!, 10 μs	For relatively low density plasmas
CH3OH laser	119 μm, 13 channels, Mickelson	5.6 × 10^{15} m^{-3} (central chord) 10 μs	Density profile measurement, density feedback
CO2laser imaging	10.6 μm and 1.06 μm (Nd:YAG laser for vibration compensation), 80 channels, Mach-Zehnder	1.1 × 10^{18} m^{-3} (central chord) 1 μs	For high-density plasmas (e.g., pellet-injected plasmas)
PCI	10.6 μ m, magnetic shear technique, 2-D measurement with a 6 × 8 detector array	—	Measurement of density fluctuation profile
Divertor	66 GHz, single channel, Mach-Zehnder	$2.3\times10^{16}$$m^{-3}$ (supposing a pass length in a plasma 3 cm) 10 μs	Line density and density fluctuation measurement of divertor plasmas

2.4 Summary

The electron density of plasma is an important parameter for plasma study and physics research. Due to the principle of electromagnetic waves propagation in plasma, the interferometer is utilized as the standard diagnostic method to measure electron density. In this chapter, the principles of the Mach-Zehnder interferometer and Michelson interferometer are introduced, which provide the basis for the selection of new interferometers on Heliotron J. The method of interferometer detection is explained, the advantages of heterodyne as an interferometer signal analysis are analyzed, and the method of analyzing the signal is introduced in detail. Finally, the interferometer used on the fusion device is summarized to provide a detailed reference scheme for the design of the interferometer on Heliotron J.

Chapter 3

The Heliotron J device

3.1 Introduction

Heliotron J is a medium sized plasma experimental device with advanced helical axis heliotron, located at the Institute of Advanced Energy of Kyoto University, which is designed and constructed to optimize helical axis heliotron configuration [44,45]. Fig. 3.1 shows the aerial view of Heliotron J. The major radius is **R** = 1.2 m, and a minor plasma radius is **a** = 0.2 m [45]. The magnetic field is generated by an **L** = 1/**M** = 4 helical-axis coil (where **L** is the pole number of the helical coil and **M** is the toroidal pitch number), two types of toroidal coils, and three types of vertical coils [44]. The magnetic field strength is up to 1.5 T, and the magnetic configuration is characterized by the rotational transform of 0.4–0.6 with low magnetic shear and by the magnetic well in the whole confinement region. Several heating systems have been used in Heliotron J: these include 0.4 MW electron cyclotron heating (ECH), 1.5 MW neutral beam injection (NBI) (Two tangential hydrogen beam lines (BLs) of NBI, BL1 and BL2, are used, which have a maximum acceleration voltage of 30 kV and a maximum power of 0.8 MW each), and 0.5 MW ion cyclotron heating (ICH) [46,47]. In addition, typical electron temperatures are Te < ~3 keV and Te < ~0.5 keV in the ECH and NBI plasmas, respectively. The ion temperatures, Ti, in the ECH and NBI plasmas are < 0.3 keV.

The mission of Heliotron J is to test the new physics principles to extend the future of the heliotron line. Compared with the issues from the Heliotron E, Heliotron J can improve the compatibility between the good particle confinement and MHD stability by introducing the helical magnetic axis, thus leading to the possibility of realizing the non-

symmetric quasi-isodynamic optimization. The objectives of Heliotron J as follows [44]:

1. To realize good high-energy particle confinement
2. To obtain higher beta capability (MHD stability)
3. To achieve a controllable particle and power handling scheme (divertor).

In this chapter, the magnetic configuration will be introduced in section 3.2. In section 3.3, the heating system will be described. The fueling technology and diagnostics will be summarized in section3.4 and 3.5 respectively.

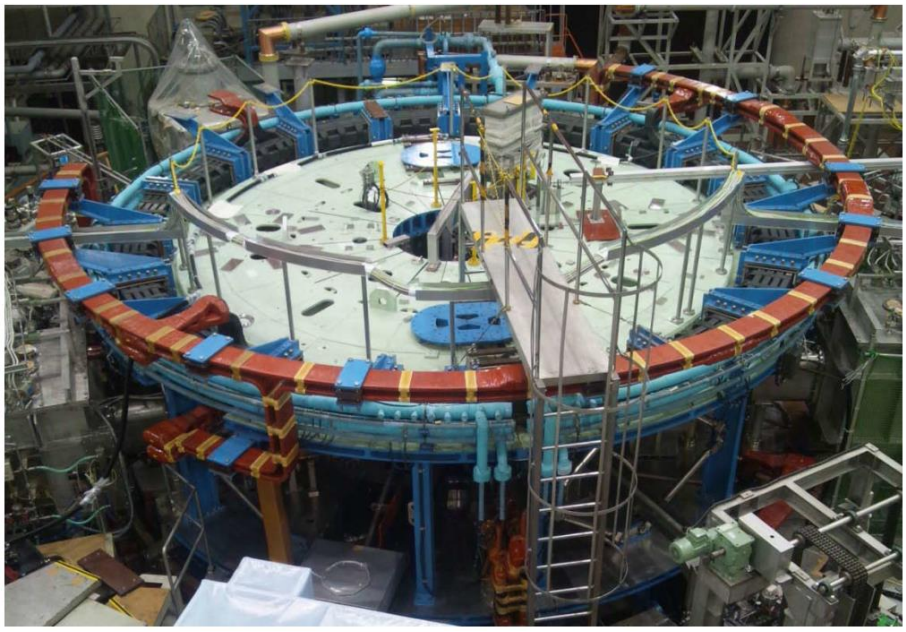

Fig.3.1 Aerial view of Heliotron J.

3.2 Magnetic field configuration of Heliotron J

Heliotron J is a quasi-poloidally symmetric optimization heliotron device with an **L**/**M** =1/4 helical winding coil [44,47]. The magnetic field consists of corner section and straight section. To realize a flexible magnetic field configuration, five sets of coils are installed to control the magnetic field configuration. Each coil is equipped with an individual power supply system, enabling flexible control of magnetic field configurations by adjusting the current in each coil. The coils in Heliotron J are shown in Fig. 3.2, helical and main vertical (H+V), toroidal A and B (TA and TB) and inner and auxiliary vertical (IV and AV) coils with different colors. TB and TA are located in the corner and straight section respectively [49].

In Heliotron J, the magnetic field can be controlled over a wide range through the combination of various coils. Due to the formation of local quasi-isomagnetic field in the straight section, the compatibility of good particle confinement and magnetic wells, can be realized without using auxiliary coils such as IV and AV. The synergy between the intrinsic and auxiliary coil system magnetic fields enables precise and nuanced control over the magnetic field coordination. The distance between the outermost magnetic surface and the inner wall of the discharge tube has been enlarged while maintaining most of the characteristics of the basic configuration, and this configuration is referred to as the "standard configuration (STD configuration)" in the Heliotron J system [50].

Heliotron J has the same magnetic surface at every 90 deg. As depicted in the figure, as shown in Fig. 3.3. Specifically, profiles at 0° , 22.5° , 45° , and 67.5° are chosen along the toroidal direction. The sections at 0° and 22.5° are called as corner section, while the sections at 45° and 67.5° are called as straight section [51].

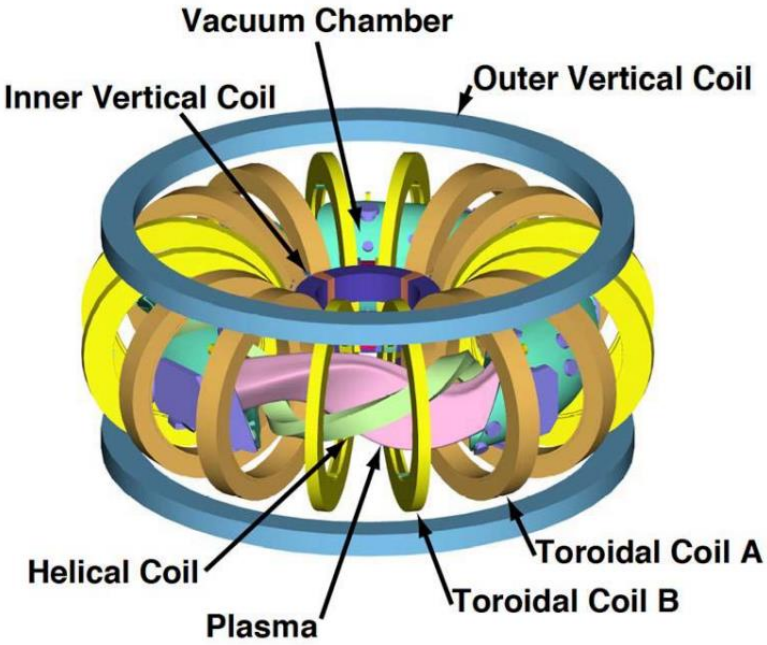

Fig.3.2 The schematic of Heliotron J device [50].

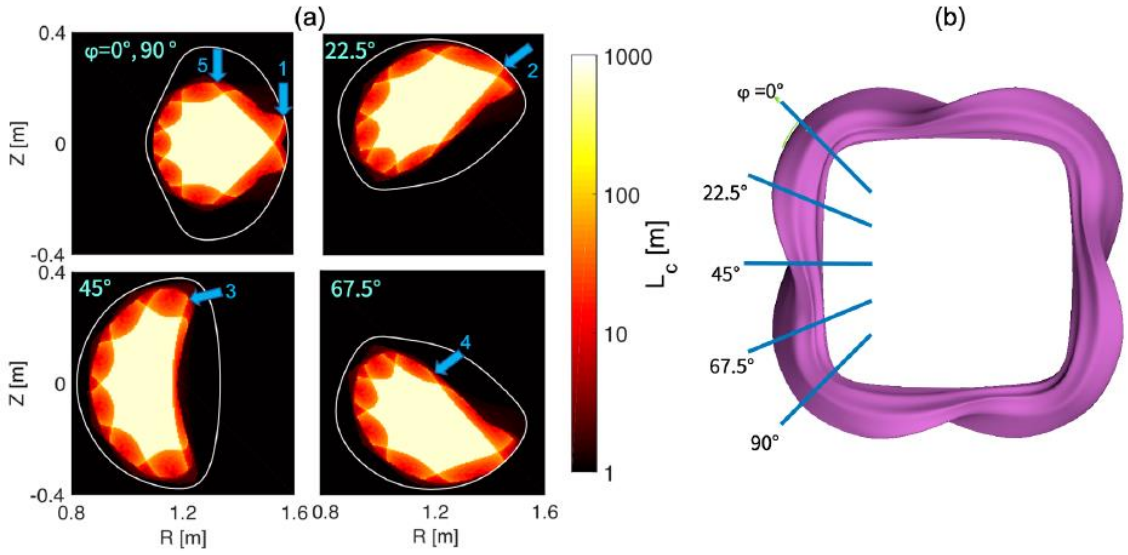

Fig.3.3 The standard magnetic field configuration of Heliotron J [51].

3.3 Plasma heating system in Heliotron J

In Heliotron J, three heating systems have been developed: electron cyclotron resonance heating (ECH), neutral beam particle injection (NBI) and ion cyclotron resonance heating (ICH). These are discussed separately in this subsection. The layout of the heating systems is shown in Fig. 3.4 [52].

3.3.1 Electron cyclotron resonance heating (ECH)

In Heliotron J, plasmas are typical produced and heated by a 70-GHz second harmonic X-mode ECH. The power of the ECH is 0.4 MW with a cut-off density of 3.0 $\times 10^{19}$ m^{-3}. Fig. 3.5 shows the schematic of the ECH system in Heliotron J. As shown in Fig. 3.6, a gyrotron can provide 500kW microwave. The ECH is injected in the # 9.5 port which connected with the gyrotron by almost 20m oversized waveguides. A matching optical unit (MOU) is used to shape the beam into a high-purity Gaussian beam, and the microwave is transmitted to the Heliotron J device by a transmission system comprising oversize waveguides of about 20 m, three miter bends, a power monitor, a polarizer and a waveguide switcher. The beam is then injected into the Heliotron J by a launcher system consisting of a fixed-focusing mirror and a movable flat-plate mirror. The measured transmission efficiency of the oversized waveguide is about 90%, which is in good agreement with the theoretical prediction [50,53].

3.3.2 Neutral beam injection (NBI) heating

NBI heating is an important auxiliary heating method in Heliotron J. Neutral particles, which are less affected by the strong magnetic field, can be injected and interact with the plasma in a given direction of motion to transfer energy and thus higher power can be deposited in the plasmas to realize the heating.

In Heliotron J, two tangential beamlines of the hydrogen neutral beam injection (NBI) systems have been developed (BL1 and BL2),as shown in Fig. 3.7. Each beamline has two bucket-type ion sources, the maximum beam power is 0.7 MW and the acceleration voltage is 30 keV. The mean pitch angle of the beam ions is about 155 (25) degree in the co- (counter-) injection case of the standard configuration of Heliotron J [49].

3.3.3 Ion cyclotron range of frequencies (ICRF) heating

In Heliotron J, ion cyclotron range of frequencies (ICRF) heating, or injected by neutral beam injection (NBI) heating are used to generate the high energy ions and research the energetic ion confinement.

As shown in Fig.3.8, the ICRF heating system consists of an oscillator, matching circuit and antenna. Two oscillators can provide with a maximum oscillation power of 1.5 MW and a pulse width of 0.2 seconds. The oscillator creates a sine wave of about 1V. After three successive amplifications, the oscillation frequency can be the range from 17.8 MHz to 53.4 MHz (up to 26.7 MHz in the first system). The ICRF heating antenna is located in the 'corner' of the vacuum chamber in Heliotron J, above and below the same poloidal plane, as shown in Fig.3.9. The ICRF can provide maximum injection power is about 2.5 MW [50,54].

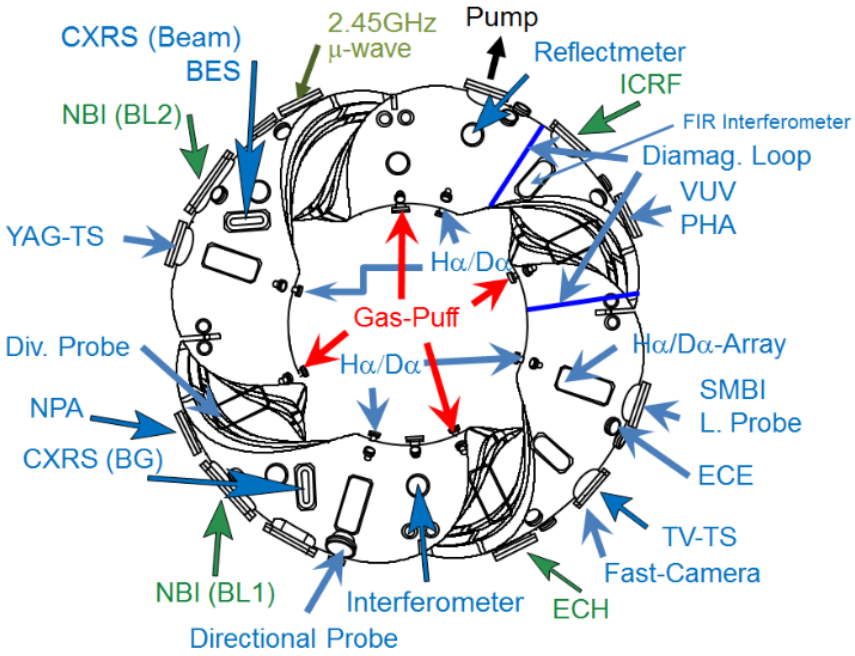

Fig. 3.4 Layout of heating, fueling and some diagnostic equipment [52].

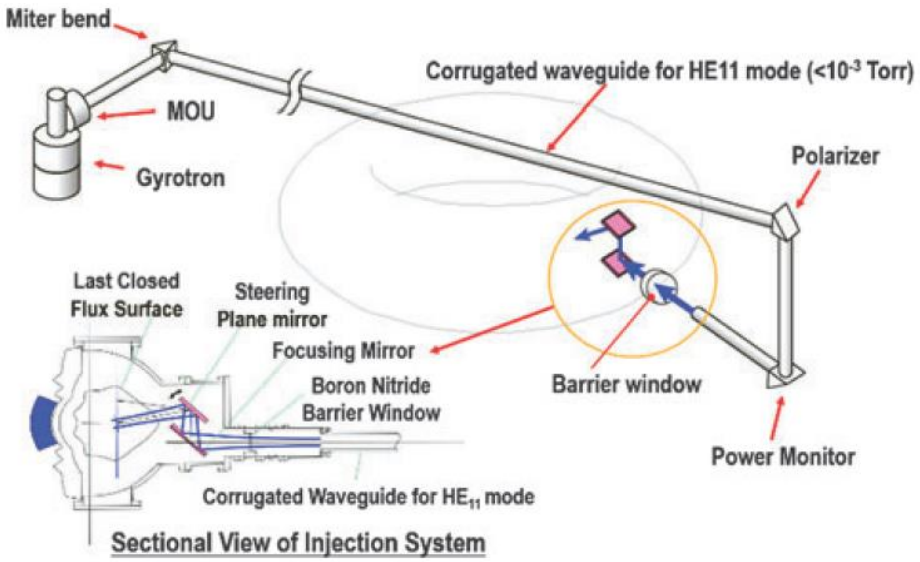

Fig. 3.5 Schematic of 70 GHz ECH/ECCD system [50].

Fig. 3.6 70GHz 500kW Gyrotron [50].

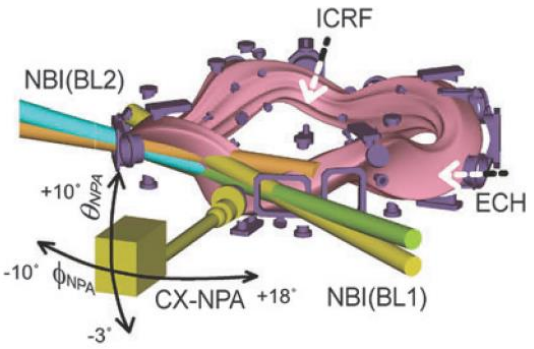

Fig. 3.7 Schematic of NBI systems [50].

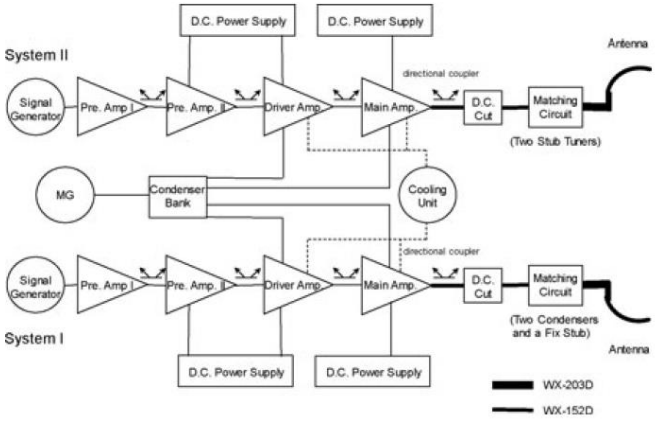

Fig. 3.8 Schematic of ICRF system [50].

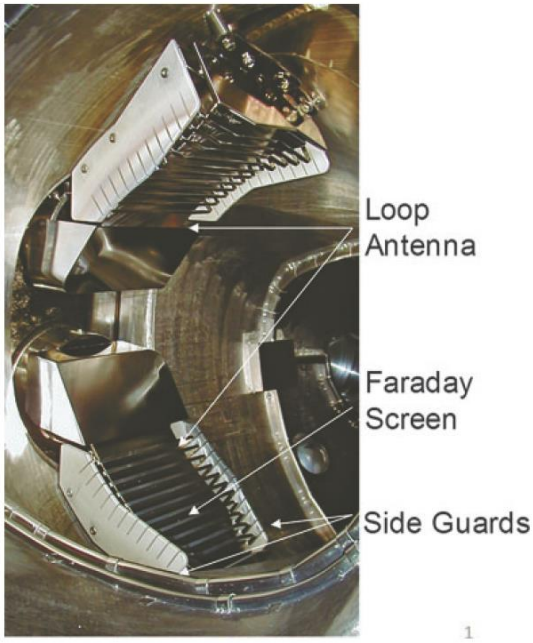

Fig. 3.9 The loop antenna and side Guards of ICRF system in the vacuum chamber of Heliotron J [50].

3.4 Fueling techniques in Heliotron J

Controlling plasma is beneficial for energy confinement. To study the physics of the high-density plasma, several fueling techniques, such as pellet injection, supersonic molecular beam injection (SMBI), and short-pulsed high-intensity gas puffing (HIGP),have been developed in Heliotron J.

3.4.1 Gas-puffing system

In Heliotron J, gas-puffing (GP) system with four piezoelectric valves is used as the conventional fueling technology to control and obtain a high-density and high-performance plasma. As shown in Fig. 3.4, the fours valves are installed at the inboard-side ports at ≈90° intervals of vacuum chamber of Heliotron J. The amount of deuterium D2 molecules from the GP system with the plenum pressure of ~ 0.15 MPa is pre-programmed to control the plasma density during a discharge. Due to spatial constraints around the torus, the nozzles of these valves do not have direct line of sight to the plasma. The induced gas from the valve, therefore, diffuses to the vacuum chamber following multiple reflections within an elbow-shaped pipe that links each nozzle to the chamber [52].

3.4.2 Supersonic molecular-beam injection (SMBI)

The supersonic molecular-beam injection (SMBI) technique, which has been developed by L. Yao et al[56, 57], is considered to be an effective fueling method for deeper penetration of neutral particles into the core plasma compared and can make a significant improvement over the conventional gas-puffing (GP). It can be applied not only for core density control but also as an effective edge modification technique in fusion devices.

In Heliotron J, the SMBI system is equipped on a horizontal port (the port number: #11.5),as shown in Fig.3.4. It consists of a fast solenoid and a magnetic shield. The diameter of its orifice in front of the valve is 0.2 mm for this experiment. During the high-density plasma experiment, SMBI is used for the fueling control [56].

3.4.3 High Intensity Gas-Puff (HIGP)

The high intensity gas-puff developed a new way to reach the higher density and stored-energy operation regime for NBI plasma. The HIGP fueling technique can realize the high-density state in the whole confinement region with its steep gradient in the peripheral region to enhance of the peak stored energy.

In Heliotron J, HIGP fueling technique has been used to realize the high-density plasma more than $1x10^{20}m^{-3}$ [58]. As shown in Fig. 3.4, the valves of HIGP are installed at the inboard-side ports at ≈90° intervals around the torus, located in the low field side of Heliotron J. The amount of deuterium D2 molecules from the GP system with the plenum pressure of ~ 0.15 MPa is pre-programmed to control the plasma density during a discharge. The difference from the SMBI system is that the induced gas from the valve is diffused into the vacuum chamber after several reflections in the elbow connecting each nozzle and chamber [58].

3.4.4 Pellet injection system

To obtain better plasma performance with high-density plasmas, the pellet injection system was installed in the Heliotron J [55]. This pellet injection system is pneumatic acceleration system using a conventional in situ technique. As shown in Fig.3.10, a Gifford – McMahon cycle compact cryocooler (SRDK-415) with the capacity of this

cryocooler is 10 W at 8 K on the second stage, is being used for the pellet formation. The speed of the pellet can be 260±30 m s^{-1} measured by a shadowgraph and light gate with the time-of- flight measurement method between two fixed positions. The size of the pellet is 1.1 – 1.2 mm injected by the fixed injection barrel which can perturb the plasma as expected [55].

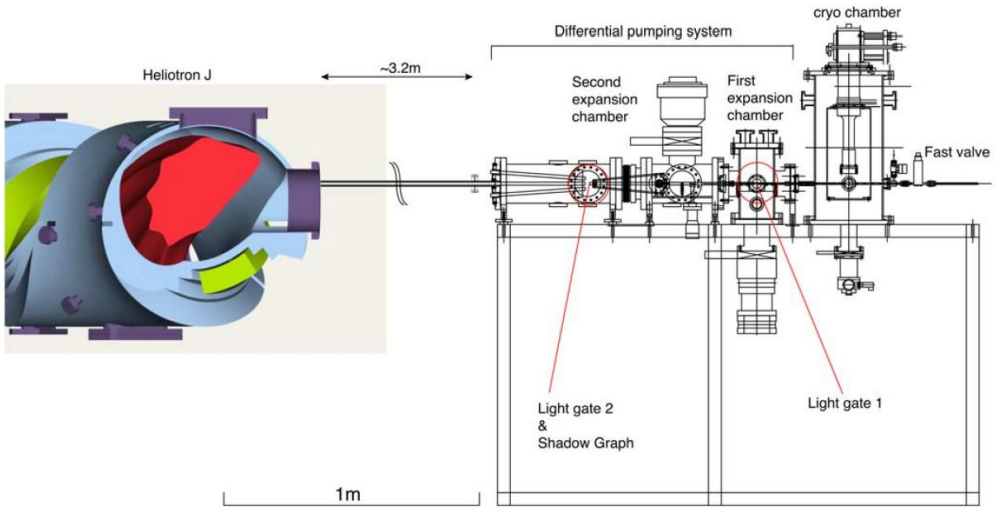

Fig.3.10 Schematic of low-speed and small-size barrel pellet injector in Heliotron J [58].

3.5 The diagnostics in Heliotron J

3.5.1 ECE Radiometer System for Heliotron J

The schematic of the ECE radiometer system in Heliotron J is shown in Fig. 3.11 . The ECE signal emitted from the window mounted on the body #11.5 port is input to the two radiometers after transmission through a waveguide; a notch filter is installed in the waveguide to reduce the influence of the strong microwaves from the 70 GHz gyrotron. The radiometer system is composed of two parts, a conventional radiometer part (part A) and a correlation radiometer part (part B).This system consists of 16 channels can measure 2nd harmonic X-mode from 58 to74 GHz. The bandwidth of this system is set as 1GHz [50,59].

3.5.2 Nd:YAG laser Thomson scattering (TS) system for Heliotron J

Controlling the plasma profile is important issue to enhance the performance of magnetic confinement fusion devices. Due to the electron temperature and density profiles can be measured the simultaneously, Nd:YAG laser Thomson scattering (TS) a basic diagnostic for the high temperature plasma experiment in the fusion devices. And it is a crucial tool for the estimation of the thermal and particle diffusivities for the transport study.

In Heliotron J, a Nd:YAG laser Thomson scattering (TS) has been developed for detailed study of the time evolution of electron temperature (Te) and density (ne) profiles. The system consists of two 550 mJ 50 Hz Nd:YAG lasers with a pulse width of 10 ns, a beam dump, large collection optics, and 25 radial channel ($\sim$ 1 cm spatial resolution) interference polychromators, as shown in Fig. 3.12. To minimize the impact of stray light caused by reflections at the input and output vacuum windows of Heliotron J, a solution has been implemented whereby the laser beams are directed to and from Heliotron J via extended evacuated pipes. The target plasma range is designed as 10 eV < Te < 10 keV and ne > 0.5×10^{19} m^{-3} [50,60,61].

3.5.3 Diamagnetic loop

The measurement of stored plasma energy is important issue to research the particle confinement and energy balance in the fusion plasma. Diamagnetic measurement is the routine method to measure the stored energy in tokamaks and stellarators. The

diamagnetic flux of the plasma is proportional to the volume-average pressure, the stored energy can be obtained by the diamagnetic measurement.

In Heliotron J, a diamagnetic loop is used to measure the change of the magnetic flux to obtain the plasma-stored energy. As shown in Fig. 3.13, the loop is installed in the vacuum chamber of Heliotron J and is coiled into single turn to achieve a fast response [50,62].

3.5.4 Absolute extreme ultraviolet (AXUV) photodiode array

The energy loss from the radiation is an important influence on high-density plasma confinement in fusion research. The importance method of radiation measurement is the AXUV, which has the high time resolution and large region from visible to soft-X ray (1.127eV to 100keV) [63, 64].

In Heliotron J, two AXUV arrays with multiple foil filters have been used for radiation profiles measurement. Figure 3.14 shows the lines of two AXUV arrays and magnetic flux in Heliotron J. Two AXUVD arrays (AXUV 16ELO/G, IRD) have been installed in Heliotron J in order to measure radiation profiles [63, 64]. One array provides a view across the entire poloidal cross section thanks to an optical filter system, while the other observes the region spanning from the plasma center to the SOL on the inboard side of the torus without utilizing an optical filter. The AXUVD boasts remarkable time precision, featuring a swift rise time of merely 0.5 μs. The aluminum foil effectively eliminates the influence of low-energy photons while permitting the transmission of high-energy photons. Conversely, the parylene foil effectively screens out photons spanning from the ultraviolet (UV) to vacuum ultraviolet (VUV) regions.

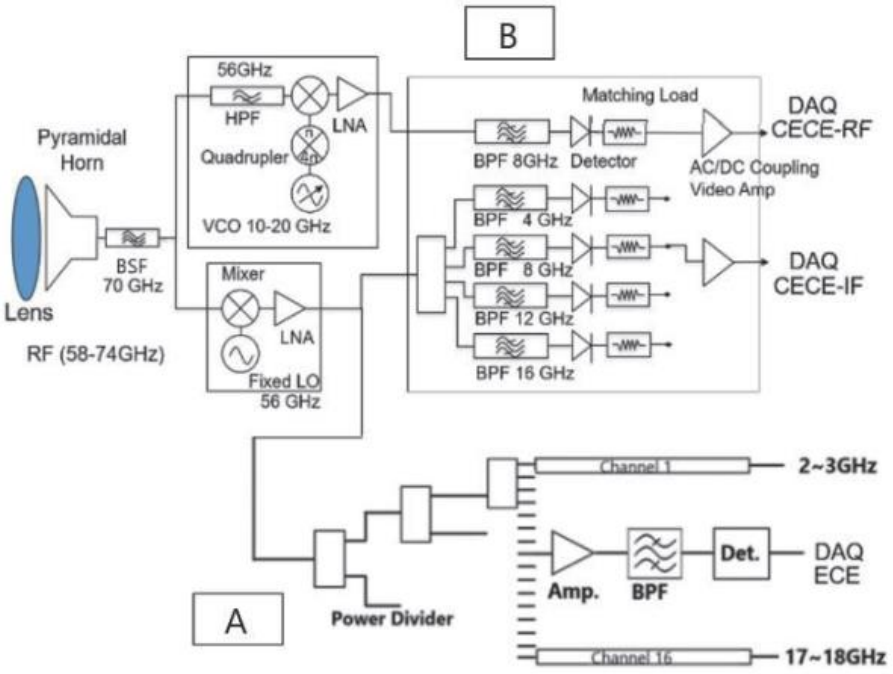

Fig. 3.11 ECE radiometer system [59].

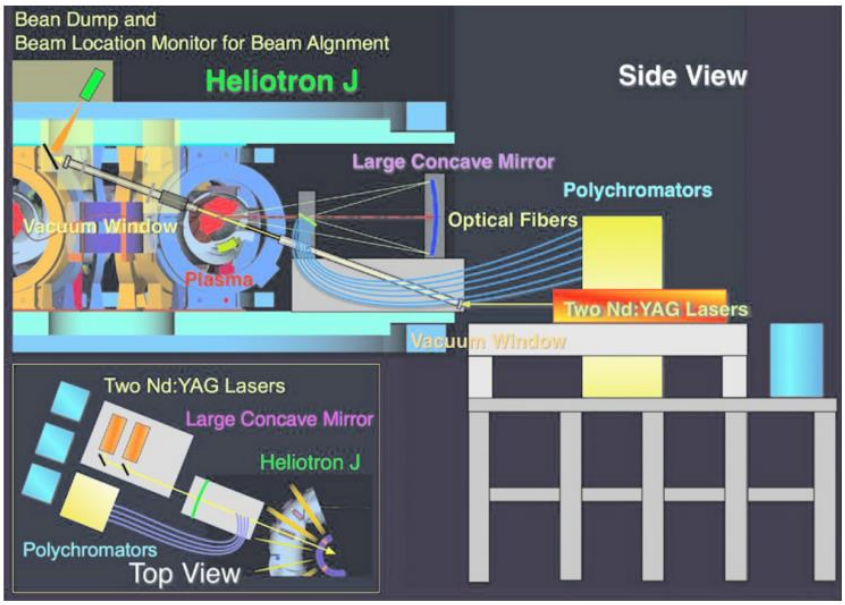

Fig. 3.12 The schematic diagram of Nd:YAG Thomson scattering system [61].

Fig. 3.13 The diamagnetic double loop in the Heliotron J vacuum chamber [62].

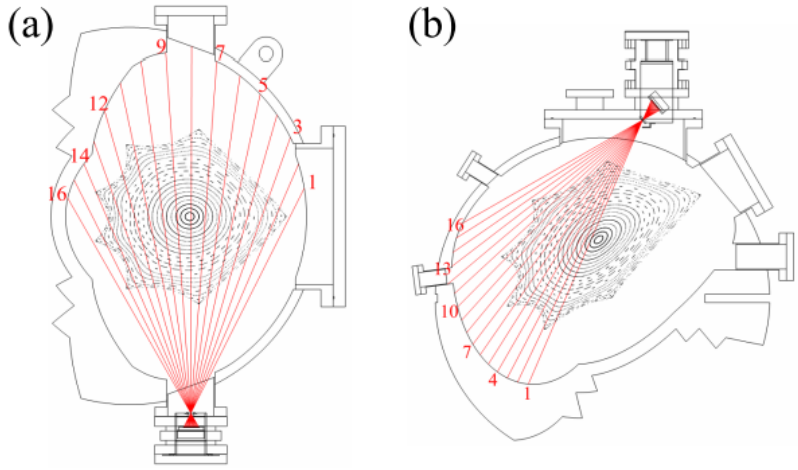

Fig. 3.14 Magnetic flux surface and lines of sight of AXUVD arrays, viewed (a) over the poloidal cross section and (b) the plasma center to the SOL [63].

Chapter 4

Development of 320 GHz interferometer system in Heliotron J

4.1. Overview of the previous interferometer system in Heliotron J

Understanding high-density plasmas through advanced fueling techniques is crucial to realize better plasma confinement. In the medium-sized helical device, Heliotron J, several fueling techniques, such as pellet injection [55], supersonic molecular beam injection (SMBI) [57], and short-pulsed high-intensity gas puffing (HIGP) [58], can help achieve a high-density plasma up to ne = ~1 × 10^{20} m^{-3}.

The interferometer measurement is a standard technique used to measure the electron density of a magnetically confined plasma [28]. A single-channel 140 GHz microwave interferometer and a single-channel HCN laser interferometer have been developed on Heliotron J [40,65]. To solve the difficulties encountered by the HCN laser interferometer and the 140 GHz microwave interferometer and understand the physics of high-density plasma production, a new 320 GHz multi-channel solid-state source interferometer was designed and developed for use in Heliotron J [66, 67,68].

In this chapter, we show the design and construction of the new submillimeter wave interferometer system.

4.1.1 Far infrared (FIR) laser interferometer

A FIR laser interferometer with high time resolution was developed for Heliotron J, as shown in Fig. 4.1 [40]. The FIR laser interferometer is a heterodyne-type Michelson

interferometer. A super rotating grating as a frequency shifter was used to make the frequency shift with maximum 1.44 MHz to enable the interferometer to achieve time resolution of less than 1 μs. An HCN laser (λ = 337 μm) was chosen as a light source to measure plasma with line-averaged density of 1×10^{18} -1.5×10^{20} m^{-3}, which satisfies the operation conditions in Heliotron J. The laser has a Fabry–Pérot-type resonant cavity consisting of a 3.2 m long, 56 mm diameter Pyrex tube and two plane reflectors. Some difficulties in operating the HCN laser are commonly recognized and maintaining the laser power requires careful control of the gas flow rate, the ratio of gas species, and the discharge tube temperature and regular cleaning of the discharge tube [40].

Fig. 4.2 shows the results of the FIR interferometer system. The plasma was initiated by a 70 GHz ECH, then the plasma heating combines low ECH with NBI. A diamagnetic loop shows the plasma stored energy. The line-average density measured by a microwave interferometer and the FIR interferometer were compared. The waveforms of these two interferometers are the same, demonstrating that the single channel FIR interferometer can be used to measure the plasma density in Heliotron J [34].

4.1.2 140 GHz single-channel microwave interferometer

A single-channel heterodyne microwave interferometer at 140 GHz was developed for Heliotron J that measures electron density using O-mode through the plasma since the first plasma operation, as shown in Fig. 4.3. The frequency range was changed to 130 GHz and 129 GHz due to a problem with the mixing of 70 GHz ECH. This microwave interferometer system has been routinely used for plasma experiment [63].

The oscillators of the system are located approximately 10 m away from the Heliotron J with two independent microwave sources provide microwaves, as shown in Fig. 4.4. Two rectangular metal waveguides connect the oscillators to the diagnostic port. For these two oscillators (QUIN STAR, Inc), one provides 140 GHz microwave with output power 23.4 mW as the probing beam through the plasma at #8.5 diagnostics port from the upside to downside, and the other provides 139 GHz microwave with output power 2.4 mW as the reference beam, as shown in Fig. 4.5 [50,65].

After passing the plasma, the signal is received and transmitted by a horn antenna with a lens. As a heterodyne interferometer, the signal was modulated into a 1 GHz signal by mixing with 139 GHz and 140 GHz signals, sent to a frequency conversion circuit, and finally modulated into a 1 MHz signal by mixing with 499 MHz and 500 MHz signals. This 1 MHz phase signal is recorded and processed by a high-speed ADC of a few MS/s

[65].

However, the microwave interferometer is inaccurate for measuring the plasma density for electron densities higher than $2\sim3 \times 10^{19}$ m^{-3} due to the refraction of the plasma resulting in a microwave beam shift. In addition, to realize the plasma density profile, multi-channel density measurements must be realized.

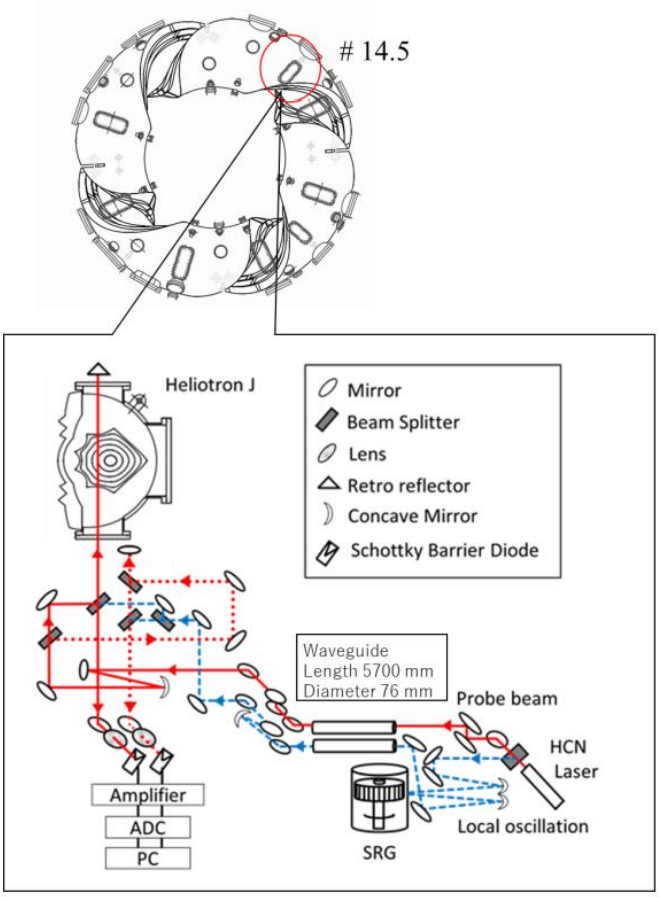

Fig. 4.1 Schematic of the FIR laser interferometer. Solid, dotted, and dashed lines denote the probe beam, reference beam, and local beam, respectively [40].

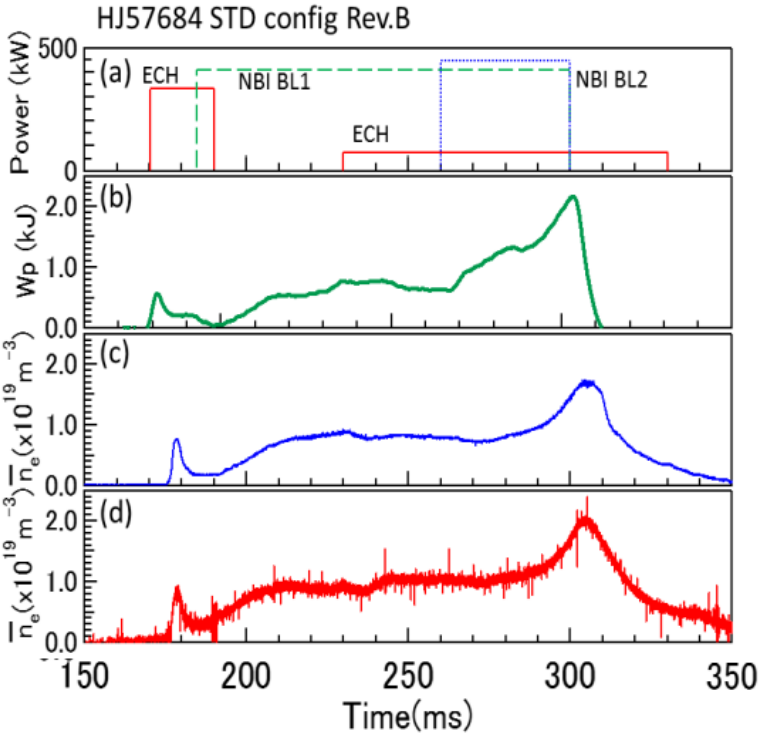

Fig. 4.2 The results of the FIR interferometer system [40].

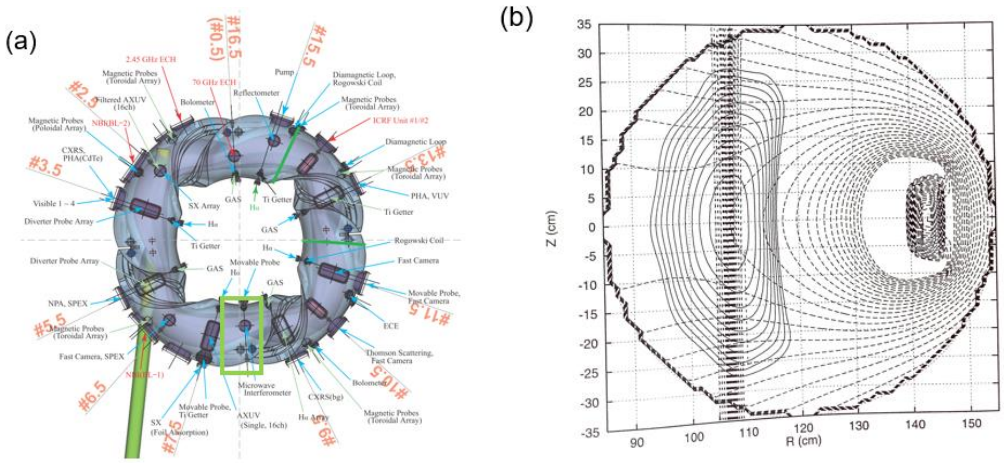

Fig. 4.3 (a) The location of the microwave interferometer in Heliotron J (b) The optical path of the microwave in # 8.5 port [65].

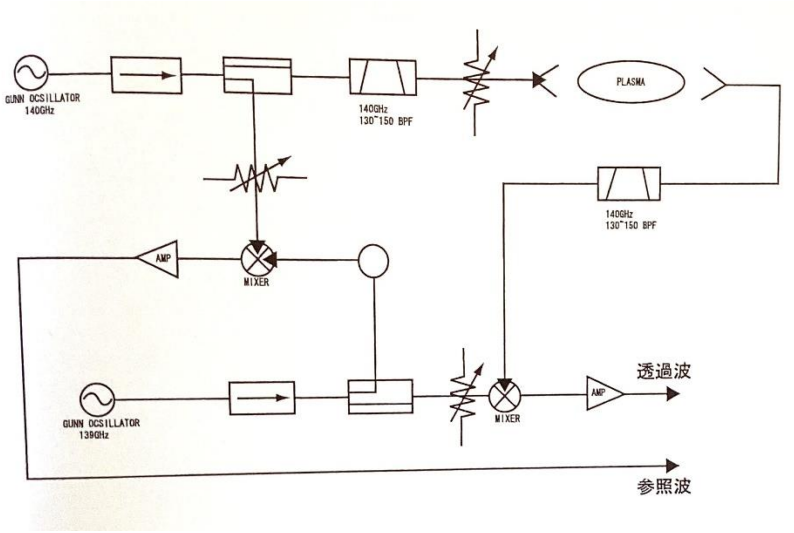

Fig. 4.4 The schematic of microwave interferometer [65].

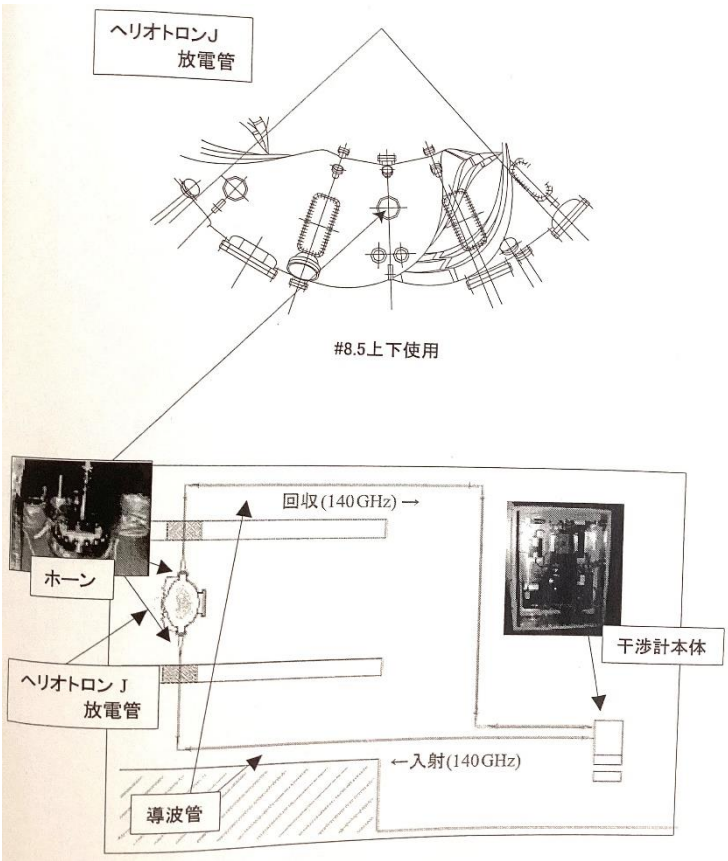

Fig. 4.5 The location of the microwave interferometer in Heliotron J [65].

4.2. Propagation of Gaussian Beam in the free space

The new interferometer utilizes 320GHz submillimeter solid-state wave sources and adopts a heterodyne Michelson-type configuration. The optical path design and beam propagation of this interferometer rely on quasi-optical techniques. As a first step in studying the propagation of Gaussian beams in free space, it is essential to understand the principles of quasi-optical transmission and the theory of Gaussian beam propagation.

4.2.1 Quasi-optical techniques and Gaussian Beam

In recent years, the utilization of short millimeter and submillimeter waves have experienced significant advancements in various fields, including radio astronomy, atmospheric remote sensing, and plasma diagnostics [69]. Consequently, the transmission of short millimeter and submillimeter waves has become increasingly important. To address this, quasi-optical transmission techniques have been developed with the aim of reducing transmission losses and achieving efficient submillimeter wave transmission. Quasi-optical transmission is based on the principle of propagating a relatively collimated beam of radiation through free space. Quasi-optics focuses on the propagation of radiation beams that are moderately collimated but have relatively small dimensions when measured in wavelengths perpendicular to the propagation axis [69,70].

Compared to other low-frequency propagation techniques like the waveguide technique, quasi-optical offers significant advantages by greatly reducing transmission losses, making it highly suitable for sub-millimeter and millimeter wave transmission in free space. Moreover, when it comes to the fundamental propagation of radiation beams and the design of optical devices such as lenses and mirrors for beam transmission, Gaussian transmission and Gaussian optics provide a concise and effective framework for quasi-optical transmission. This widespread adoption of Gaussian beam propagation theory and Gaussian optics enables accurate analysis of quasi-optical propagation and facilitates precise optical path design for transmission systems [69].

4.2.2 Propagation of the Gaussian Beam

To operate the Gaussian beam transmission system efficiently, we consider only the fundamental Gaussian mode, which is axially symmetric. The beam power conforms to the Gaussian distribution at the transverse distance from the propagation axis.

The distribution of the power intensity in the cross section of the Gaussian beam

transmission can be expressed in the eq.(4.1) [38]:

$$I(z) = I_0 \exp\left(-\frac{4r^2}{d^2}\right), \tag{4.1}$$

where I_0 is the peak value of the Gaussian beam, r is the distance from the propagation axis, *d* is the diameter at the 1/e point of the intensity of the beam. The intensity of the Gaussian beam distribution is shown in Fig. 4.6. As the distance from the axis increases, the intensity of the beam typically decreases with the highest intensity located near the beam axis.

As shown in Fig. 4.7 (a), the beam propagates along the Z-axis. In the beam profile perpendicular to the transmission axis, the cross-section of the beam shows a Gaussian distribution according to the Gaussian transmission theory and is only related to the distance from the propagation axis. The dimensions of the beam vary at different positions on the propagation axis. The beam radius is smallest at the beam waist position and gradually increases away from the beam waist.

Along the propagation direction of the beam, the transmission of the beam is an expansion of the equiphase plane, which conforms to the Gaussian form, as shown in Fig. 4.7 (b). The radius of curvature of the beam at the beam waist is infinite, and after moving away from the beam waist, the distribution of the beam is represented by the distance from the beam waist. The diameter at the distance Z from the beam waist on the propagation axis can be obtained from the eq.(4.2) [71],

$$d(z) = \left[{d_0}^2 + \frac{4\lambda^2}{\pi^2}\frac{Z^2}{d_0^2}\right]^{1/2}, \tag{4.2}$$

where d_0 is the diameter of the bundle waist (Z=0). Additionally, we can obtain the radius of curvature, as follows.

$$z_R = Z\left(1 + \frac{\pi^2 d_0^2}{4\lambda^2 \pi Z^2}\right), \tag{4.3}$$

For optical path design of propagation systems with Gaussian beams, converging optics are often used to adjust the size of the Gaussian beam, which is essentially a shift in the beam waist size and position, as shown in Fig. 4.8. The Figure shows the change in parameter of a Gaussian beam after passing through a thin lens. The relationship before and after using an optical component with focal length f can be obtained from the eq.(4.4),

$$\frac{1}{d_2^2} = \frac{1}{d_1^2}\left(1 - \frac{Z_1}{f}\right)^2 + \frac{1}{f^2}\left(\frac{\pi d_1}{2\lambda}\right)^2, \tag{4. 4}$$

where d_1 is the diameter of the Gaussian beam before the thin lens, and d_2 is the diameter of the beam after the transformation from the thin lens. The position of the new beam waist from the Gaussian transformation of the lens can be obtained by this equation as follows,

$$Z_2 - f = (Z_1 - f)\left[\frac{f^2}{(Z_1 - f)^2 + \left(\pi d_1^2/(2\lambda)\right)^2}\right]. \tag{4.5}$$

where Z_2 is the position of the new Gaussian beam waist after the lens.

With these equations, it is possible to determine the position and diameter of the new Gaussian beam waist. In complex transmission systems, the optical design often undergoes multiple iterations and adjustments. By employing these equations, one can effectively accomplish the optical path design and select appropriate optics for a Gaussian beam transmission system. These equations provide valuable tools for optimizing and fine-tuning the system to achieve the desired beam characteristics and performance. These theories are useful for the optical path design in the new interferometer system.

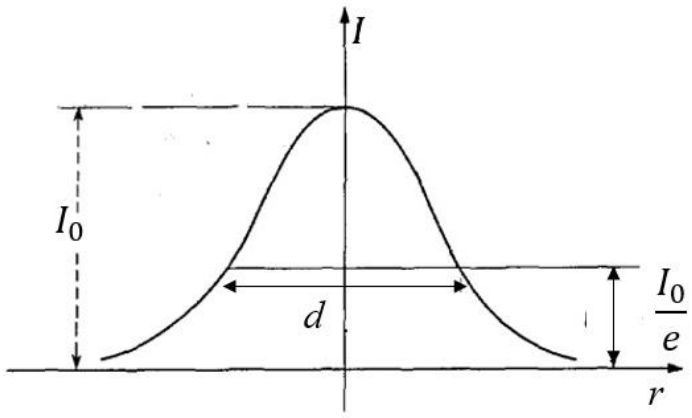

Fig. 4.6 The intensity distribution of Gaussian beam [71].

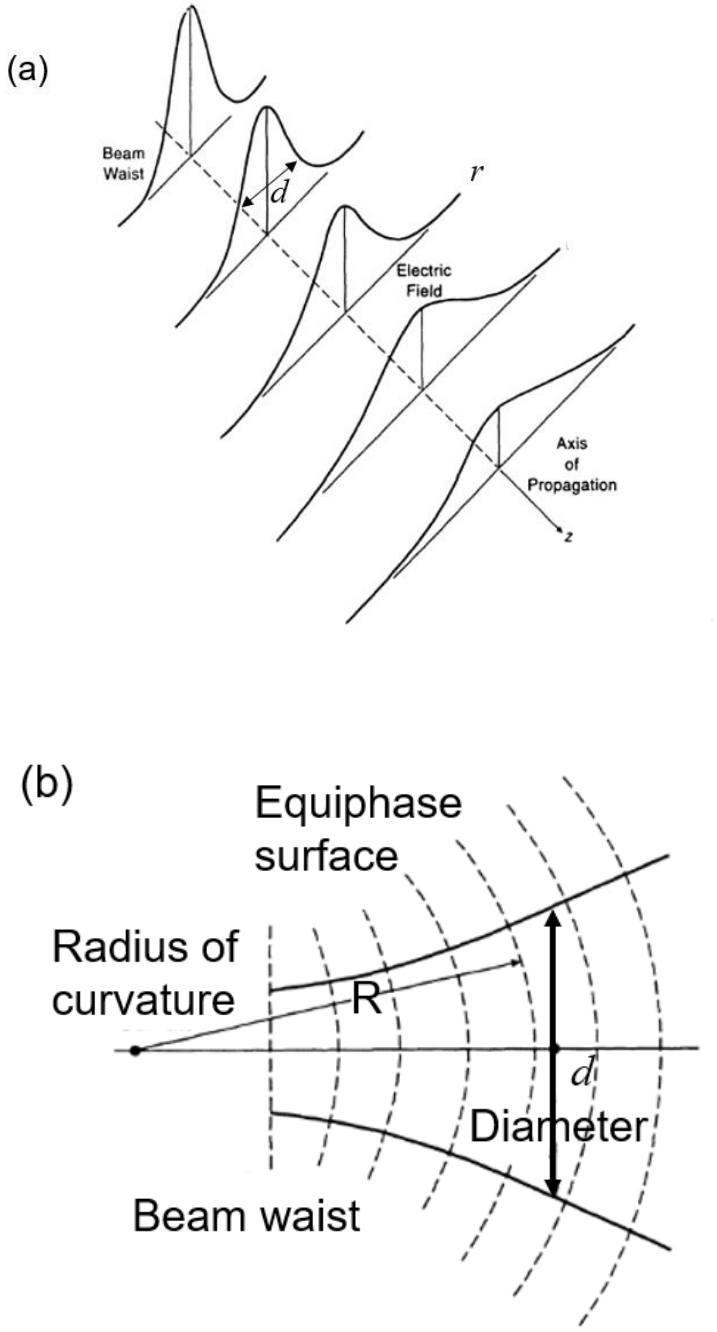

Fig. 4.7 Schematic diagram of Gaussian beam propagation. (a) Propagating beam indicating increase in beam radius and diminution of peak. amplitude as distance from waist increases. (b) Cut through beam showing equiphase surfaces (broken lines), beam radius w, and radius of curvature R [69,70].

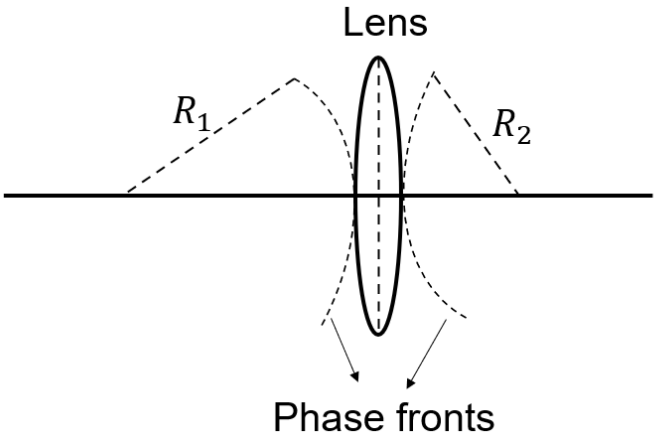

Fig. 4.8 Schematic diagram of Gaussian beam transformation with lens. R_1 is the radius of the before the lens and R_2 is the radius of the beam after the transformation [71].

4.3 New 320 GHz interferometer system

A new 320 GHz solid-state source interferometer is installed in the Heliotron J at the # 10.5 section to explore the physics of high-density plasmas (ne > 2–3 × 10^{19} m^{-3}, typically) realized with advanced fueling techniques. This interferometry system is a Michelson-type, based on the heterodyne principle, with two independent solid-state sources delivering an output power of up to 50 mW. A high time resolution measurement of <1 μs can be derived by tuning the frequency of one source in the frequency range of 312–324 GHz on the new system, which can realize the fluctuation measurement. To reconstruct the electron density profile, a pair of off axis parabolic mirror (OAP) is used to convert the probing beam into sheet beam to realize multichannel measurement [66,67,68].

Figure 4.9 is the schematic of the new 320 GHz multichannel interferometer system in Heliotron J at # 10.5 section. Compare with the previous FIR interferometer, the new interferometer with two separate solid-state sources makes the system more compact and easier to perform routine maintenance. The OAP system produces a sheet beam to achieve multi-channel measurements, reducing the complexity of the system compared to conventional interferometers [67].

In this subsection, we will describe the design and construction of the new 320 GHz multichannel interferometer system. A meticulous explanation of each component comprising the interferometer system will be provided. The content will follow a chronological sequence, starting with the development of single-channel systems and gradually progressing towards the more complex multi-channel systems. This approach allows for a thorough understanding of the evolutionary process and the rationale behind the design choices made for each stage of the interferometer system.

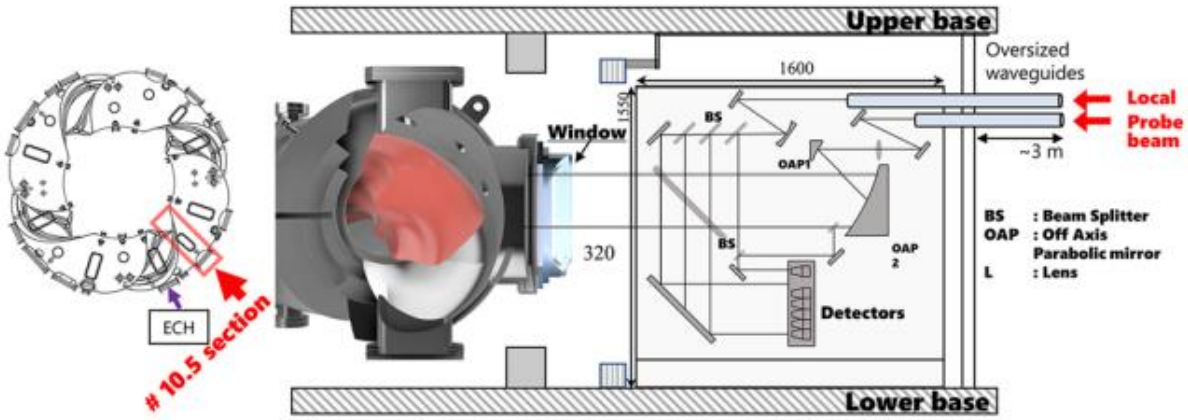

Fig. 4.9 Schematic of new 320 GHz interferometer in Heliotron J [67].

4.3.1 Design and construction of the single-channel 320 GHz interferometer system

The single-channel 320 GHz interferometer has been constructed and operated as commissioning before the installation of the multi-channel system. To minimize the losses caused by submillimeter wave transmission, quasi-optical techniques has been used for the optical path design.

The schematic of the single-channel interferometer is shown in Fig. 4.10. The optical paths of the reference and probe beams have identical designs before entering the waveguide; therefore, only the probe beam path is shown in the schematic. The source located on optical bench A produces 320 GHz submillimeter wave, and concave mirrors and plane mirrors carefully adjust the beam width and the beam waist position at the waveguide inlet to optimize submillimeter wave transmission efficiency in the oversized waveguide to the Heliotron J side. On the optical bench B close to the diagnostic port, the arrangement with concave mirror and plane mirrors injects the probe beam to the plasma along the mid-plane. A retroreflector array installed at the vacuum chamber wall reflects the probe beam to the incident direction. The reflected beam combines with the reference beam and is detected by a detector on the optical bench B.

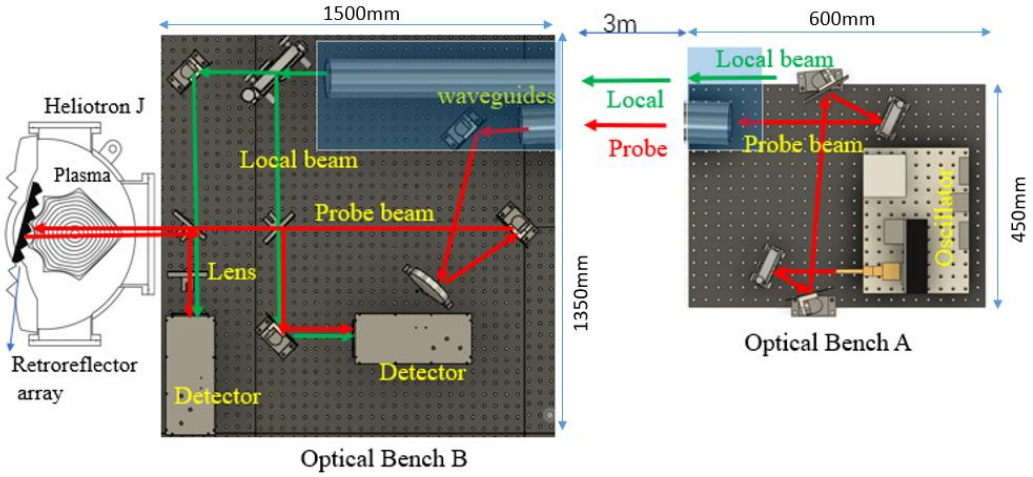

Fig. 4.10 Schematic of a single-channel interferometer. The sources are located on optical bench A. A submillimeter wave is transmitted to optical bench B through oversized dielectric waveguides [68].

4.3.2 Solid state sources

The submillimeter wave source and optical bench A are placed approximately 3 m away from the Heliotron J coils to avoid the influence of the magnetic field on the sources. Two separate solid-state oscillators (VDIE0029, AMC 630, Virginia Diodes, Inc.) are used as microwave generators. The sources are compact and easy to control. Each source provides a maximum of 50 mW output power. The output frequency of one source is fixed at 320.16 GHz, whereas the other is tunable in the frequency range of 312–324 GHz. The frequency difference between the two sources can be easily changed to control the IF frequency. The time resolution of the interferometer is determined by the IF frequency of the system. Therefore, this system may obtain a high time resolution of less than 1 μs to measure density fluctuations [67,68].

Each solid-state source consists of two parts, the oscillator and amplifier, the connection method of them as shown in the Fig. 4.11 and Fig. 4.12. For the fixed frequency source in Fig. 4.11, it is composed of a phase-locked voltage-controlled oscillator (PVCO) output the 13.34GHz microwave, and 24 times amplifier-multiplier chain (AMC) provide the microwave at 320.16 GHz. The other tunable frequency source as shown in Fig. 4.12 is composed of a synthesize with a frequency of 12.3–14.3 GHz and AMC. The output frequency become 312–324 GHz controlled by the PC by a USB cable. And each of the source can provide the maximum power up to 50mW.

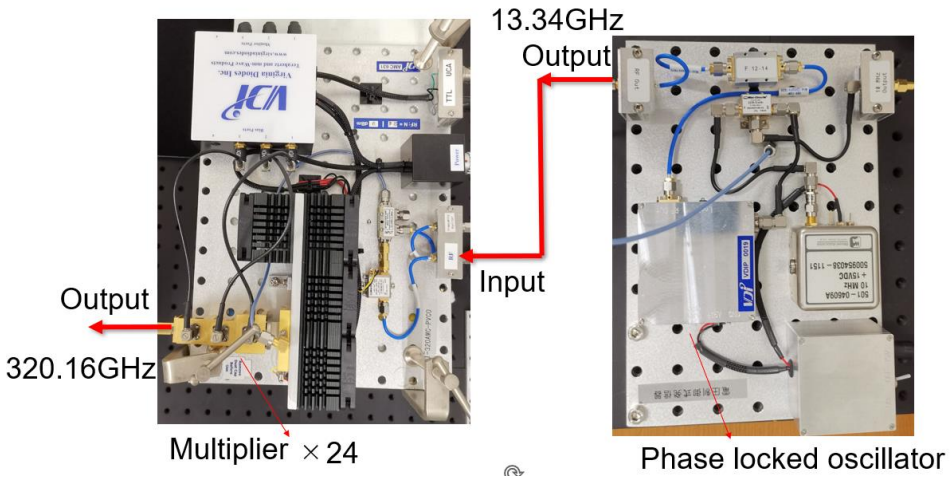

Fig. 4.11 The solid source of 320GHz with fixed frequency.

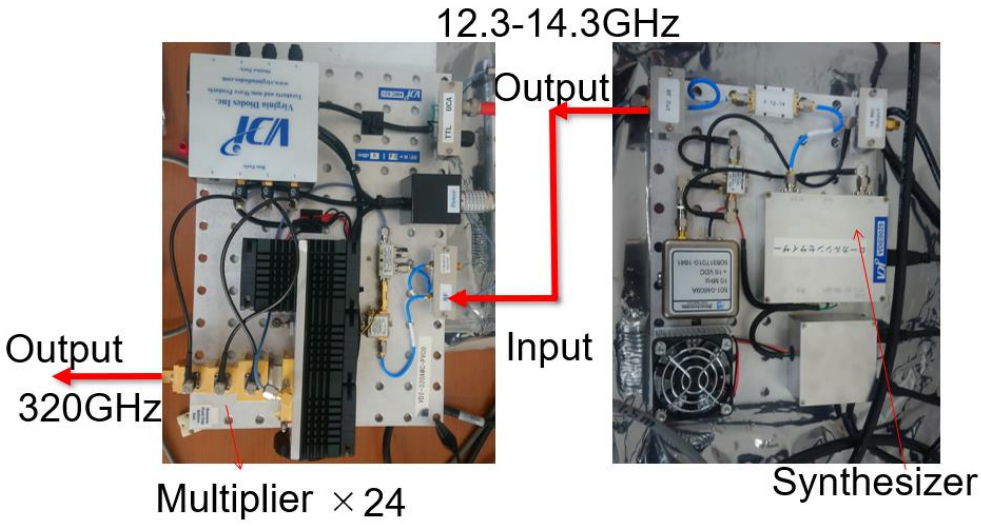

Fig. 4.12 The solid source of 320GHz with tunable frequency.

The descriptions and specifications of each component of the 320 GHz solid-state source are illustrated are shown in table 4.1 and 4.2. Fig. 4.13 shows the economical synthesizer, which is combined with the multiamplifier for microwave generation. Figure. 4.14 displays a fixed frequency oscillator that undergoes modulation by the multiamplifier chain shown in Fig. 4.11, resulting in the output of a 320.16 GHz submillimeter wave signal. The parameter of the phase-locked oscillator and

multiamplifier are shown in table 4.3 and 4.4.The output power of the microwave can be controlled using the User Controlled Attenuation (UCA) feature on the amplifier, which is connected to an external power supply. This power regulation capability is significant for practical measurements, as it allows for precise adjustments in power levels as needed. The product performance (output power versus output frequency) of the AMC 630 and AM631 are shown in Fig. 4.15 and Fig.4.16, respectively.

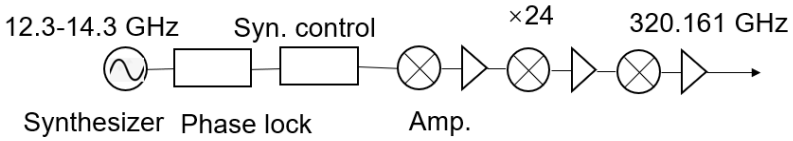

Fig. 4.13 The diagram of the source with tunable frequency.

Table 4.1 Product specifications of AM 630

Description		Specification	Connector
RF Output [1]	Frequency Range	312-324GHz	WR2.8 UG-387/UM
	Output Power(Peak)	50mW	
RF Input [2]	Frequency Range	13-13.5GHz	SMA(f
	Power(Typical/Damage)	-1to 5 dBm/8dBm	
	Multiplication Factor	24	
DC Input [3]	Comparable with VDI-175T power Supply	-	3B 310 LEMO
Amplitude Modulation[4]	TTL/AM Input	0-5V, up to ~5kHz	BNC(f)
RF Attenuation[5]	User Controlled Attenuation	0V(full power), 5V (off)	BNC(f)
Frequency Monitor[6]	-	~13-13.5GHz,~10dBm	SMA(f)

Table 4.2 Product specifications of VDI Economy Synthesizer

No.	Part Description	Specification
1	DC Power Connection	2.1mm I.D.×5.5mm O.D. ×9.5mm (m)
2	RF Output	12.3-14.3GHz;~1dbm*[SMA (f)]
3	Phase Lock Light	LED on=LOCKED
4	10MHz Output	SMA (f)
5	USB Synthesizer Control	USB Type B
6	Stability (set by crystal oscillator)	＜1ppm
7	Switching Speed	100ms(100MHz Step)
8	Phase Noise	-87dBc/Hz at 10kHz offset at~12GHz output

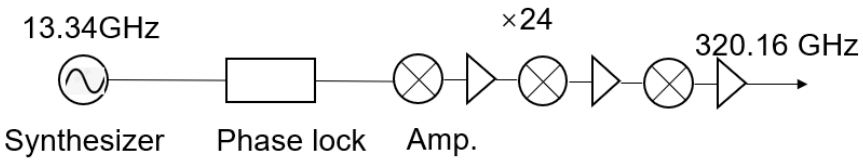

Fig. 4.14 The diagram of the source.

Table 4.3 Product specifications of AM 631

Description		Specification	Connector
RF Output [1]	Frequency Range	312-324GHz	WR2.8 UG-387/UM
	Output Power(Peak)	50mW	
RF Input [2]	Frequency Range	13-13.5GHz	SMA(f
	Power(Typical/Damage)	-1to 5 dBm/8dBm	
	Multiplication Factor	24	
DC Input [3]	Comparable with VDI-175T power Supply	-	3B 310 LEMO
Amplitude Modulation[4]	TTL/AM Input	0-5V, up to ~5kHz	BNC(f)
RF Attenuation[5]	User Controlled Attenuation	0V(full power), 5V (off)	BNC(f)
Frequency Monitor[6]	-	~13-13.5GHz,~10dBm	SMA(f)

Table 4.4 Product specifications of the Phase-locked Voltage controlled Oscillator

No.	Part Description	Specification
1	DC Power Connection	2.1mm I.D.×5.5mm O.D. ×9.5mm (m)
2	RF Output	~1dbm*[SMA (f)]
3	Phase Lock Light	LED on=LOCKED
4	10MHz Output	SMA (f)
5	Stability (set by crystal oscillator)	＜1ppm
6	Output Frequency	13.34GHz
7	Output Power	~1dBm +/- 3dB
8	Phase Noise	-105dBc/Hz at 10kHz offset at~12GHz output

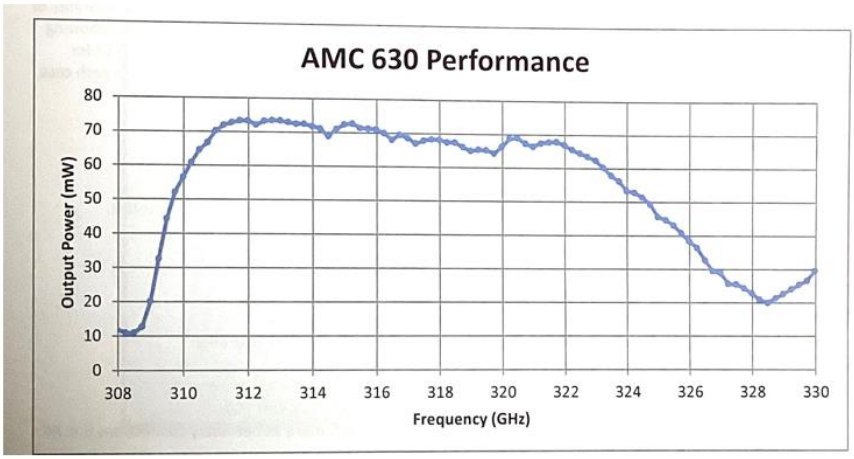

Fig .4.15 output power versus output frequency of AM630.

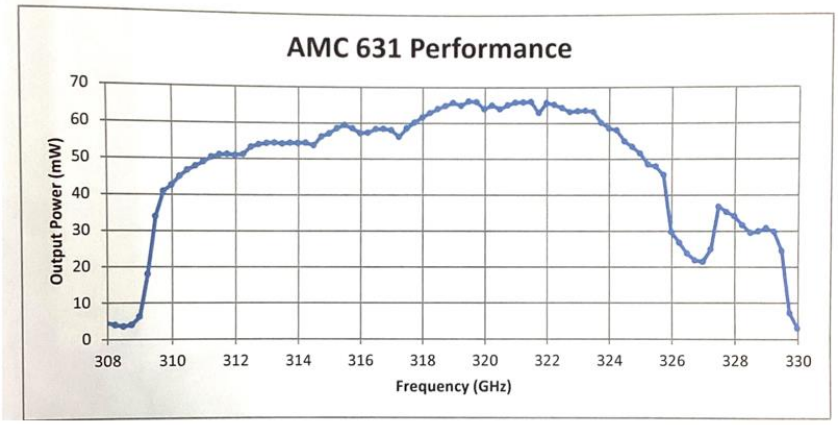

Fig .4.16 output power versus output frequency of AM631.

Prior to the construction of the interferometer system, we conducted a tabletop test on the solid-state source to validate that the beam propagation generated by the source aligns with the principles of Gaussian beam propagation theory. Fig. 4.17 illustrates the setup where the solid-state source is activated, and a microwave detector (DET-03, Millitech, Inc., as depicted in Fig. 4.18) is employed to measure the power distribution profile of the beam. Fig. 4.19 is the structure of the Diagonal Horn of the oscillator. The diameter of the beam waist inside of the oscillator is 3.8mm. The distance between the outlet of the horn and the beam waist ZA is 4.6mm.

The distance between the detector and output of the oscillator is set 158mm. During the measurement, the detector is moved by a moving stage. This measurement confirmed that the power distribution at the source adheres to a Gaussian beam distribution, as predicted by Eq. (4.1).

Furthermore, as presented in Fig. 4.20, experimental results demonstrate a precise match between the power distribution at the source and the Gaussian beam distribution outlined in Eq. (4.2). Subsequently, we conducted the same measurement at four additional points (the distance z from the beam waist is chose at 163, 188, 213, 288, 388 mm from the oscillator) along the propagation path. The original point of scanning is set at the same horizontal level as the oscillator. The obtained results are depicted in Fig. 4.21. The measured data was fitted using Eq. (4.2), and the fitting results indicate that the 320 GHz submillimeter wave conforms to Gaussian transmission throughout the transmission path.

This comprehensive assessment guarantees that both the solid-state source and the transmission path adhere to Gaussian beam characteristics, laying the foundation for the subsequent development and deployment of the interferometer system.

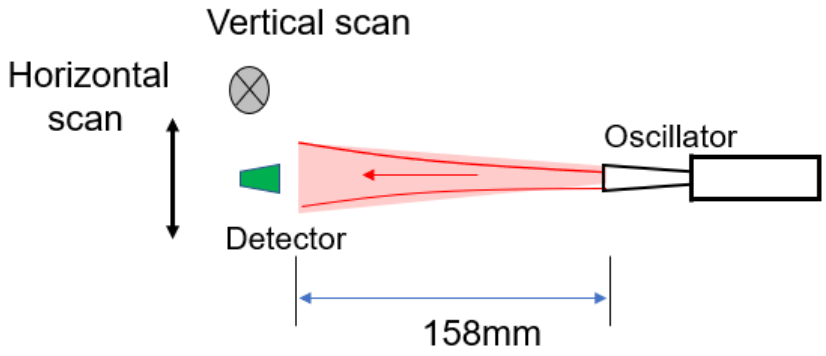

Fig. 4.17 Experiment setup for the Gaussian beam measurement.

Fig. 4.18 The DET-03 detector. Utilizing Schottky barrier zero-bias diodes, provide the power detection over the 18 to 325 GHz range.

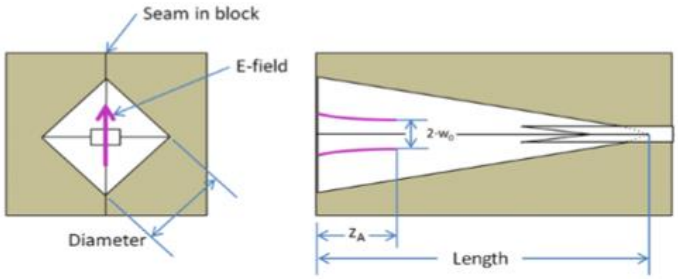

Fig. 4.19 The structure of the Diagonal Horn in the oscillator

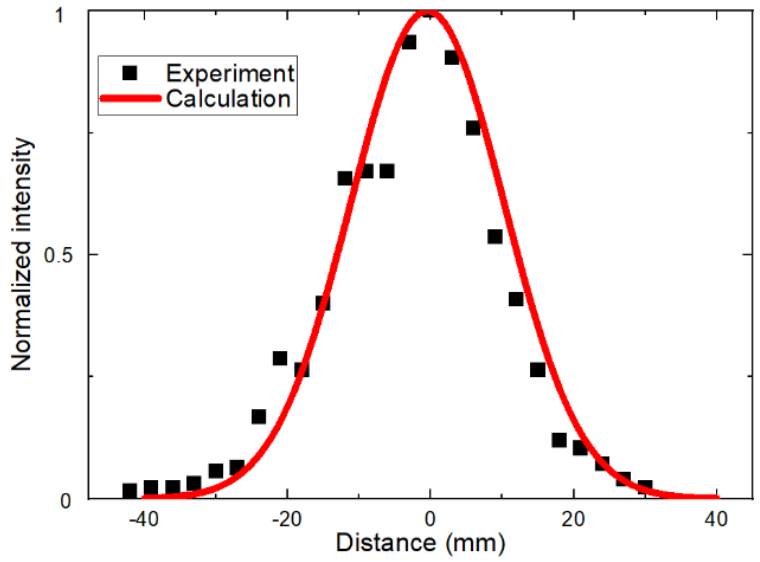

Fig. 4.20 Measurement result of the beam intensity profile after the oscillator. The black square are the measured results, the red line is the calculation of the Gaussian distribution.

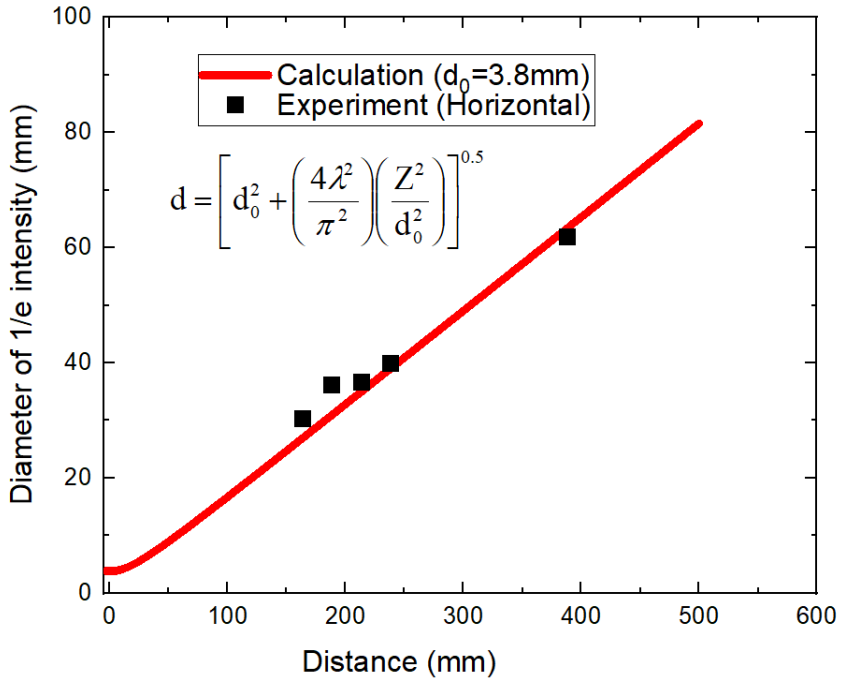

Fig. 4.21 Measurement result of the beam profile in the propagation direction. The black square are the diameters of Gaussian beam of the measured results, the red line is the calculation result of the Gaussian propagation depend on the Eq.(4.2).

4.3.3 Optical path design for single-channel interferometer

With the 320 GHz microwaves generated from the oscillators, the main focus is to achieve efficient transmission of the beam to the Heliotron J device enabling measurements. To accomplish this, a quasi-optical technique is employed, utilizing optical components for microwave transmission. The transmission of the microwave beam involves three key parts:

1. Optical bench A and oversized waveguide : The sources are located on the optical bench A, generate the 320 GHz microwaves that need to be transmitted. The oversized waveguide serves as the connection between the microwave sources and the Heliotron J, device facilitating the efficient transfer of the microwaves.

2. Optical Bench B: The optical bench B is located near the Heliotron J device. It acts as a platform for various optical components and assists in the proper alignment and manipulation of the microwave beam as it enters into the Heliotron J.

3. Retroreflector array: The retroreflector array is installed on the wall of vacuum chamber. Its purpose is to reflect the probing beam back in the original direction, where it combines with the reference beam. This combination enables interference and realizes the measurement process.

A Beam propagation on the source side and the propagation in the waveguide.

According to the principle of Gaussian beam transmission, the beam size will increase as the propagation of the beam from the beam waist. After the oscillator, on optical bench A, the beam size and beam waist position of the microwave are controlled by two concave mirrors. With other two plane mirrors controlling the transmission direction, the beam is transmitted to the waveguide, as shown in Fig. 4.22.

The oversized waveguides are dielectric waveguides with a diameter of 76mm. These waveguides play a crucial role in connecting the microwave source to the optical path on optical bench B, which is situated near the Heliotron J device, as shown in Fig. 4.23 (a), (b), and Fig. 4.24.The transmission efficiency with oversized waveguide depends on the design of the optical path on optical bench A. The wavelength and the position of the concave mirrors are determined by the oversized waveguides. To maximize the transmission efficiency, the position of the beam waist should be at the waveguide inlet and a beam size of less than half of the inner diameter of the waveguide are optimal requirements to achieve higher transmission efficiency. Aligning the incident beam axis

with the waveguide axis is critical for optimal performance [72,73]. Fig. 4.25 provides a schematic of this principle.

The transmission efficiency of the waveguide is given by the following equations [72,73],

$$T = \frac{P_S}{P} = \frac{1-\exp(-F\frac{R^2}{{r_o}^2})}{F} \quad , \tag{4.6}$$

$$F = 1 + \frac{v^2+1}{\sqrt{v^2-1}} \frac{L}{R} \frac{1}{k^2{r_o}^2}, \tag{4.7}$$

where P is the beam power before the waveguide, Ps is the beam power at the exit. R is the radius of the waveguide, r_o is the beam waist. K is the free-space propagation constant. L is the length of the waveguide, v is the refractive index.

Figures. 4.26 shows the transmission efficiency of the waveguide with an inner diameter of 76 mm, calculated based on Refs. 72 and 73 with eq.(4.6) and (4.7). Considering the beam radius constraints from Fig. 4.26, the beam diameter on the entrance of the waveguide was designed and aligned to be approximately 20–50 mm of at a beam diameter the waveguide inlet with the expected transmission efficiency of more than 90%. Depending on these results and the MATLAB calculation, the beam is adjusted by two concave mirrors and two plane mirrors to make the beam waist locate close to the inlet of the waveguide. The concave and plane mirrors are made of aluminum.

Fig. 4.27 shows the calculation results of Gaussian beam transmission. The two concave mirrors with focal lengths of 120mm and 750 mm meet the optical path design. With the concave mirrors and waveguides, the 320GHz microwave transmitted to the optical bench B close to Heliotron J.

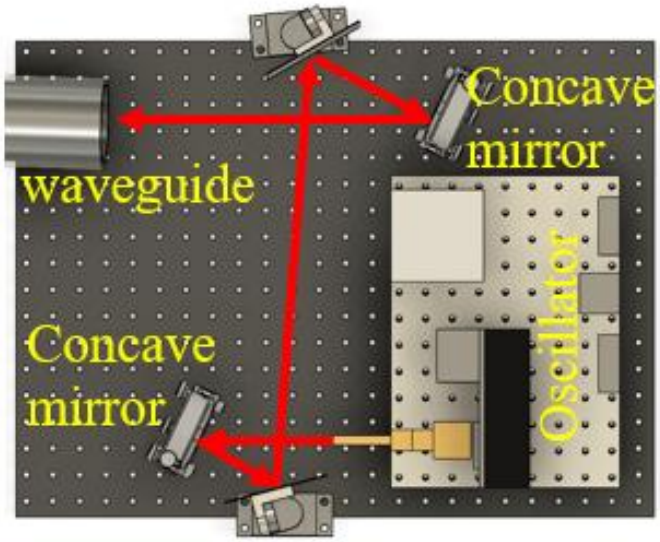

Fig. 4.22 Optical design with two concave mirrors and two plane mirrors to the waveguide on the optical bench A.

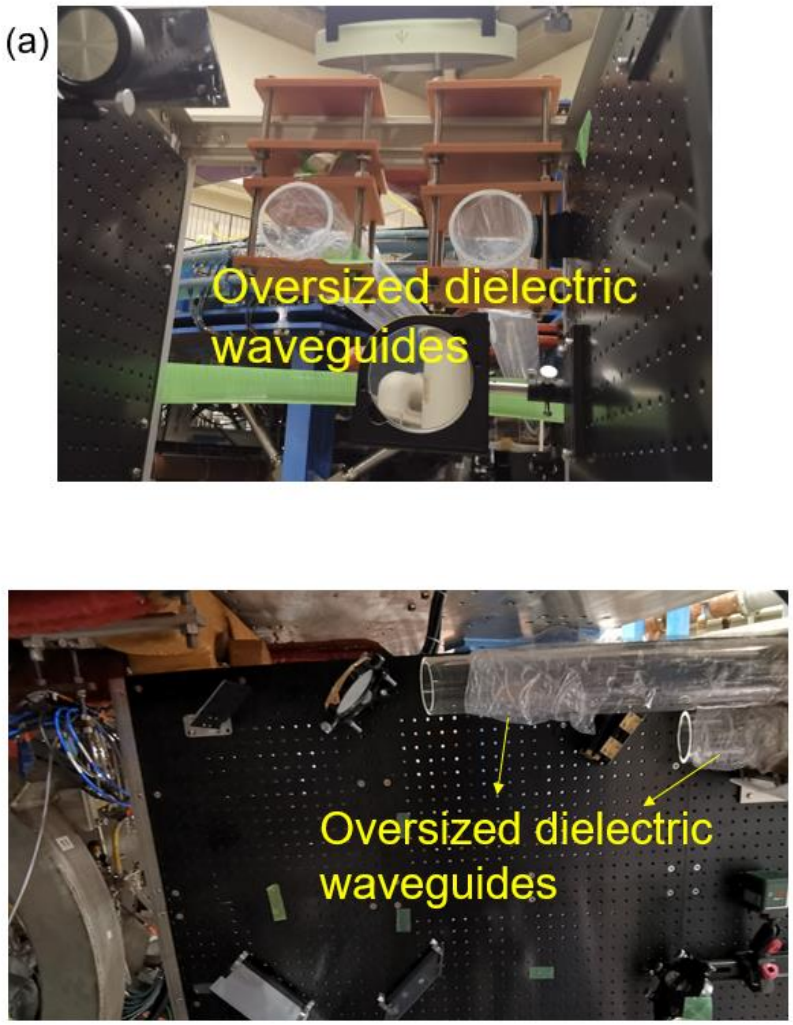

Fig. 4.23 (a) The oversized waveguide on the optical bench A. At the waveguide inlet, the beam size is less than half of the waveguide and the beam waist is located at the waveguide inlet to obtain high transmission efficiency. (b) The oversized waveguide on the optical bench B. Two separate oversized waveguides, one output the probing beam and the other provide the reference beam.

Fig. 4.24 The oversized waveguide connect the optical bench A and optical bench B to realize the high transmission efficiency between the source and HJ.

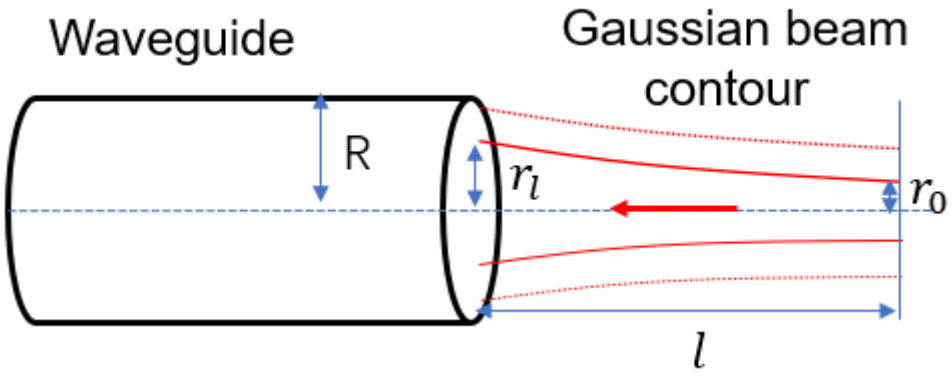

Fig. 4.25 The relation between the beam waist and the oversized waveguide. r_l is the radius of the incident beam at the inlet of the waveguide, r_o is the radius of the beam waist, l is the distance between the beam waist and the inlet of the waveguide [72].

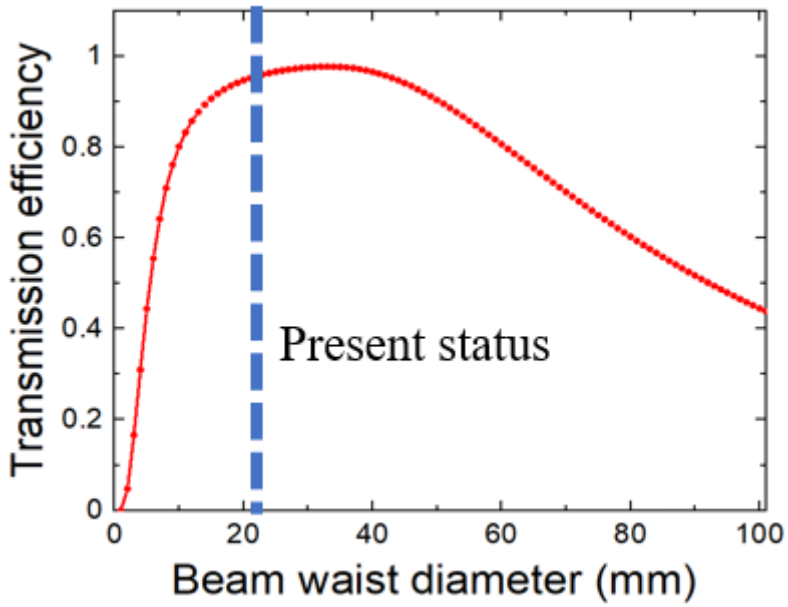

Fig. 4.26 Transmission efficiency of dielectric oversized waveguide with an inner diameter of 76 mm.

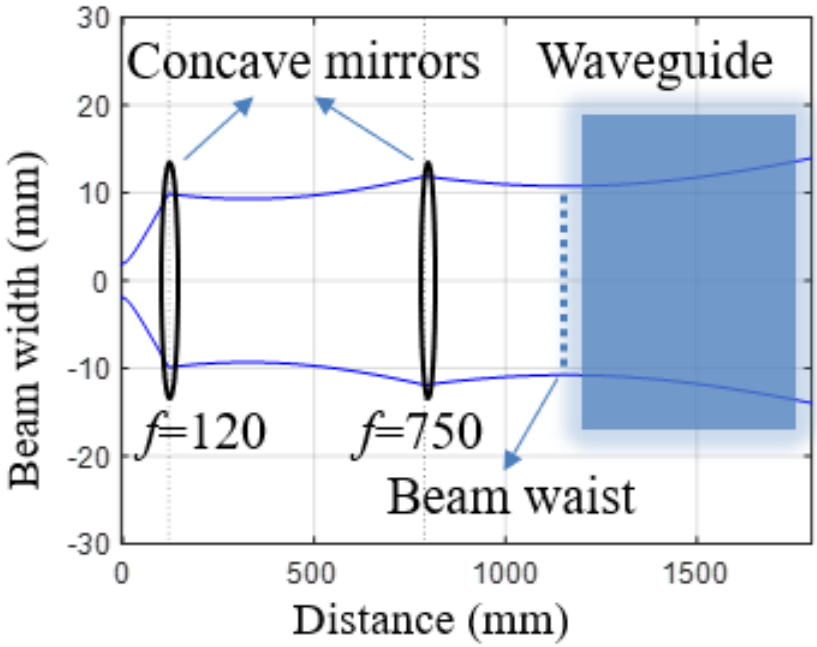

Fig. 4.27 Beam transmission calculation result from the source to waveguide on optical bench A. At the waveguide inlet, the beam size is less than half of the waveguide, and the beam waist is located at the waveguide inlet to achieve high transmission efficiency [68].

B The beam propagation on the Heliotron J side

After the transmission to optical bench B, the probe beam injected from outside the Heliotron J vacuum chamber port into the plasma and reflected by a retroreflector array installed on the inner vacuum chamber wall. The beam mixed with the local beam and detected by a single-ended mixer (WR-2.8FM, Virginia Diode, Inc.) on optical bench B.

The beam alignment on the optical bench B is shown in Fig. 4.28. The submillimeter wave transmitted to optical bench B through the waveguide and injected into the plasma from the diagnostic port, passing through the mid-plane of the plasma. The beam transmission from the waveguide on bench B is calculated, as shown in Fig. 4.29. One concave mirror with a focal length of f = 3000 mm is used to suppress the beam expansion after the waveguide.

To ensure precise beam alignment, we employ a detector to measure the beam on optical bench B. The beam profiles have been measured at two positions at z = 1590 mm (point 1) and z = 2000 mm (point 2), as indicated in Fig. 4.29, on optical bench B to compare the results with the simulation results. A microwave detector (DET-03, Millitech, Inc.) measured the profiles. Figure. 4.30 displays the measurements taken at the two measurement points, with a Gaussian fitting applied. Subsequently, the beam distribution at these points was calculated based on the Gaussian beam transmission principle. The calculated results closely resemble the measured results, affirming that the beam transmission adheres to the Gaussian transmission principle. The agreement between the calculated and measured results serves as strong evidence supporting the reliability of the optical path design and beam alignment. Additionally, since the scanning original point was chosen at the midplane of Heliotron J, these results confirm that the probing beam is accurately positioned at the midplane was appropriately constructed as designed.

During the measurement, submillimeter wave absorbers used to suppress stray signals are employed around the transmission line to ensure that the signal is directly transmitted from the retroreflector array. As shown in Fig. 4.31, the submillimeter wave absorber produced by Maxell, Ltd is a non-transparent material, one side is black absorbing material, the other side is covered with reflected material to increase the wave absorption performance.

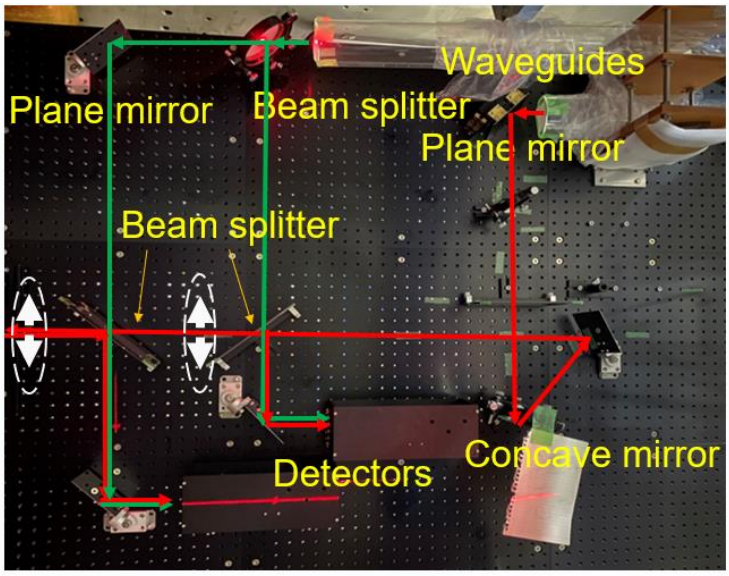

Fig. 4.28 Optical path design on optical bench B. The submillimeter wave is transmitted to the optical bench B through the waveguide and is injected into the plasma from the diagnostic port, passing through the mid-plane of the plasma.

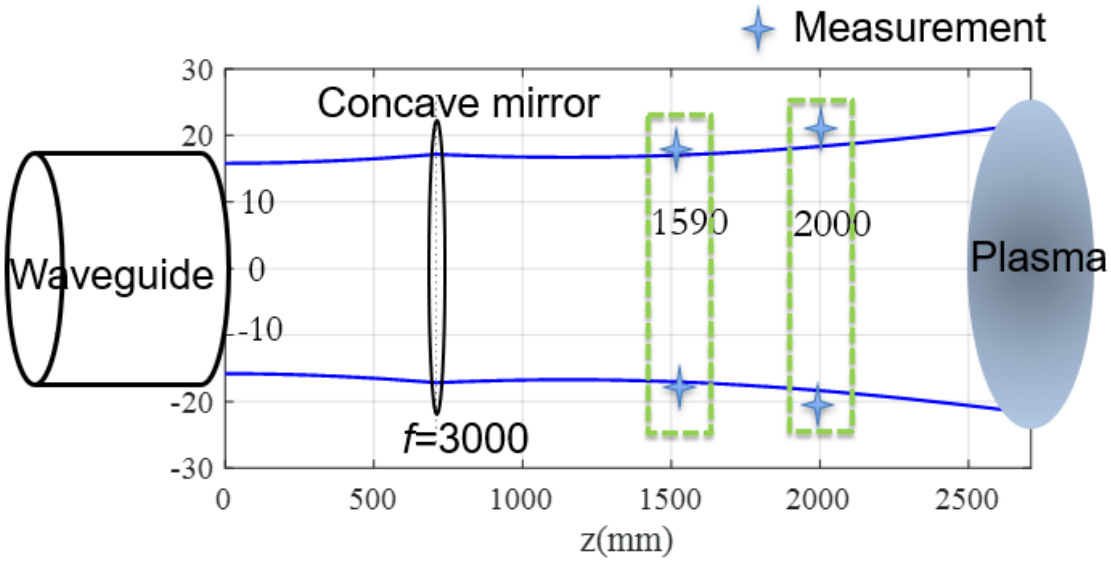

Fig. 4.29 Calculation of beam size from waveguide to plasma. One concave mirror with a focal length of f = 3000 mm is used to suppress the beam expansion after the waveguide [68].

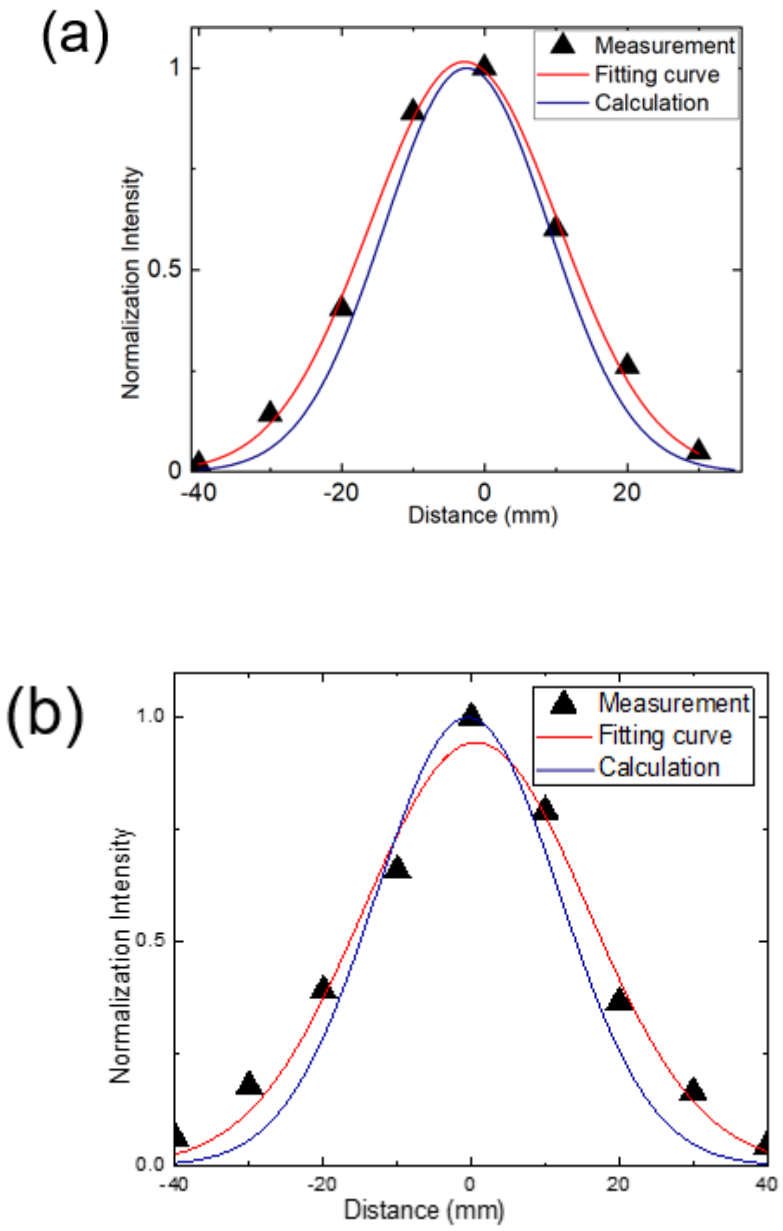

Fig. 4.30 (a)Profile of the beam on point 1,(b) Profile of the beam on point 2. Two positions indicated in Fig.4.29 on the optical bench B have been measured at to compare the beam profiles the results with the designed value [68].

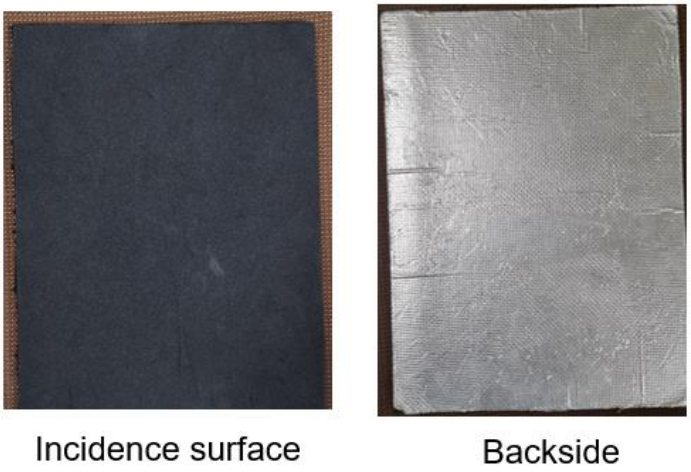

Fig. 4.31 The absorbing material.

4.4 Signal detection system

4.4.1 Detector

After being reflected by the retroreflector array on the wall of the vacuum chamber, the probe beam passes through the plasma and is reflected by the beam splitter. This converges with the reference beam into the mixer. Using the method described in Chapter 2, the intermediate frequency (IF) signal is detected by the WR2.8FD detector, as shown in Fig. 4.32. The detector is a single ended mixer with a high responsivity of ~350 mV/mW at the center frequency of 320 GHz. The parameter is shown at the table 4.5.

The detector output signal is then passed through the signal line to the ADC (WE7000 series ADC data processing system is used in this system) for further processing. The ADC performs data conversion and processing on the detector output signal.

Once the signal is acquired by the ADC, a Fast Fourier Transform (FFT) is applied to the data. By analyzing the frequency components, the line integral density of electrons can be derived.

4.4.2 Shielding box

To prevent the influence of magnetic field on the detector, a shielding box as shown in Fig. 4.33, is designed to shield the magnetic field and the surrounding electromagnetic waves and to fix the detector. The design of the shielding box is shown in Fig. 4.33 and consists of an internal L-support assembly and a shielding box housing. Since the detector has no fixed contacts, we take two small metal plates and bolts on the edges to fix the detector. The L-shaped metal plates and the shielding housing are fixed, and long holes are used for the connections, which can be adjusted in position during the alignment of the optical path.

Before the plasma experimental measurement, a beat signal has been measured with the interferometer, as shown in Fig. 4.34. The intensity of the waveform is 0.8V with the frequency 1MHz. The oscilloscope signal shows a smooth sine curve with a measurement period of 1 μs, which indicates that the setting of microwave source frequency and the optical path construction are in accordance with the design expectations.

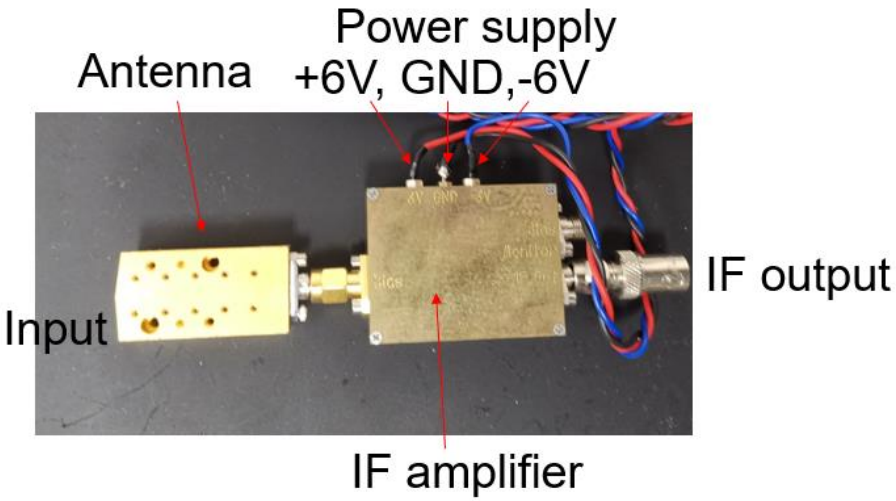

Fig.4 32. The photo of the detector.

Table 4.5 The parameter of the detector

Parameter	Specification
RF Output [1]	320GHz [WR2.8DH,~25dB]
LO Input [2]	320GHz [WR2.8DH,~25dB]
IF Output [3]	2MHz[SMA(f)]
LO Input power(Typical/Damage)	0.5-1mW/3 mW
RF Input power(Typical/Damage)	＜50 μ W/500 μ W
Typical Responsivity	＞350 V/W
DSB conversion loss	＜14dB
Customer Supplied Bias[3]	+6VDC(red)/GND(black)
IF Amplifier Gain	200
Change in Video Response[4]	＜300mV

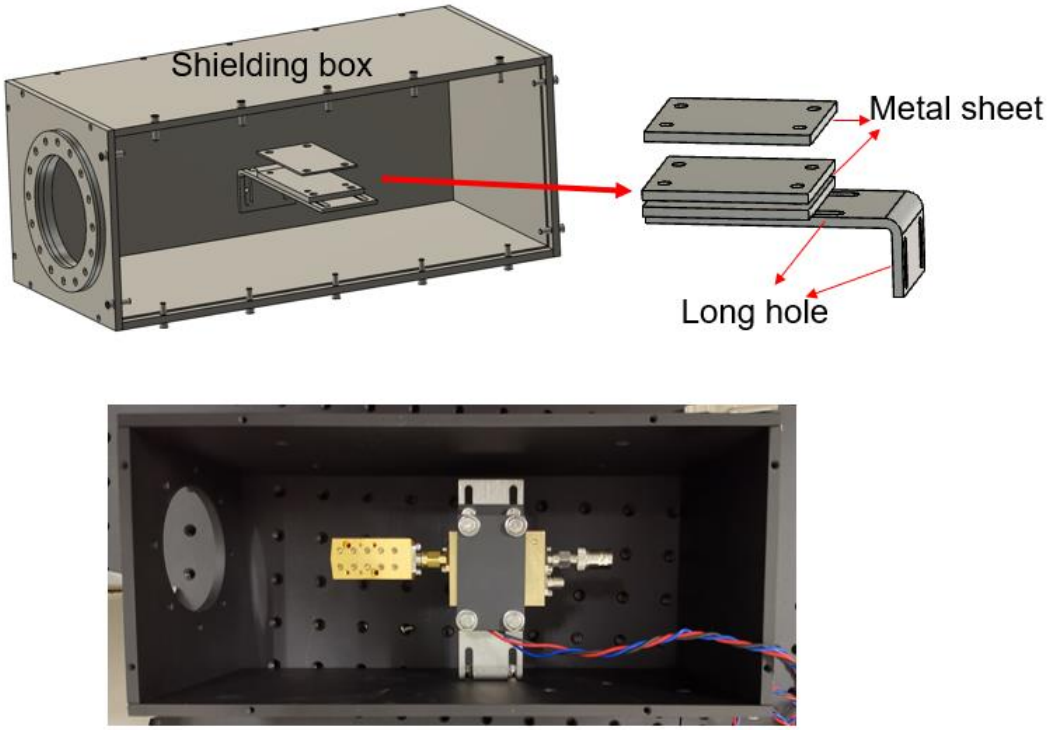

Fig. 4.33. The shielding box and the detector fixed in the shielding box.

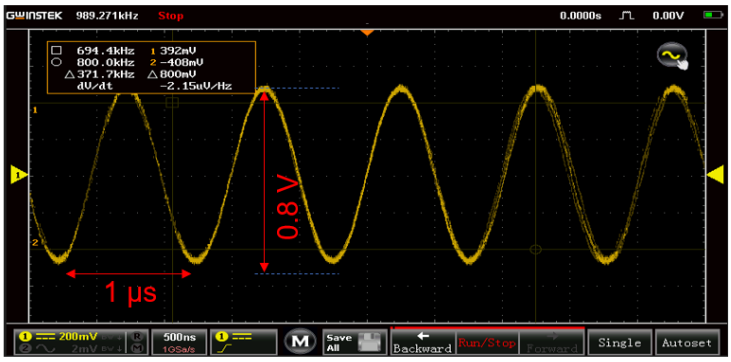

Fig. 4.34 The beat signal measured by the detector during the construction.

4.4.3 Methods of phase evaluation

The method used for signal measurement is the heterodyne， and the detector only sensitive to the low frequency signal. The beat signals of the probe detector and reference detector are transmitted to the ADC system. Therefore, the ADC system analyzes only the beat signals and obtains the phase difference by comparing the two beat signals. The beat signal measured as the real part, then the

Hilbert transform the real part to the imaginary one [40]. After this transformation, with the Euler's formula as shown in (4.8), we can obtain the analytic signal in Eq.(4.9)

$$e^{ix} = cosx + isinx \tag{4.8}$$

$$Z(t) = S(t) + \frac{j}{\pi}\int_{-\infty}^{\infty}\frac{s(t')}{t-t'} \tag{4.9}$$

According to the analytic signal theory, the instantaneous phase can be obtained by

$$\varphi = arctan\frac{I_m[Z(t)]}{R_e[Z(t)} \tag{4.10}$$

Where Im is the imaginary part, and the Re is the real part. By this method, the instantaneous phase will be calculated by the analysis system and the phase difference $\Delta\varphi$ can be obtained to calculate the electron density.

4.5 Development of multichannel interferometer system

The 320 GHz single-channel interferometer system has been used for the experimental campaign during 2021-2022, and detailed experimental results will be described and presented in chapter 6. To investigate the confinement and transport in fusion plasma experiments, the single channel of 320 GHz interferometer system has been upgraded to a multi-channel system by extending the probe beam to a sheet beam to enable the measurement in Heliotron J.

4.5.1 Overview of multichannel interferometer system

Figure 4.35 shows the schematic of the multi-channel interferometer. On the right side of the figure, optical bench A, the solid-state source and the optical path are depicted. The submillimeter wave is adjusted in shape by three large concave mirrors and two plane mirrors before reaching optical bench B near Heliotron J. After the probe beam reaches at the optical bench B, a concave mirror with a focal length of 3000 compresses the beam. To extend the probing beam to a sheet beam, a pair of off-axis parabolic (OAP) mirrors are used. The OAP system converts the probe beam to a parallel sheet beam with a diameter of 141mm to inject into the vacuum chamber. The sheet beam reflected on the retroreflector array on the wall of the vacuum chamber. By simply setting the detector after the beam splitter enables multi-channel measurements.

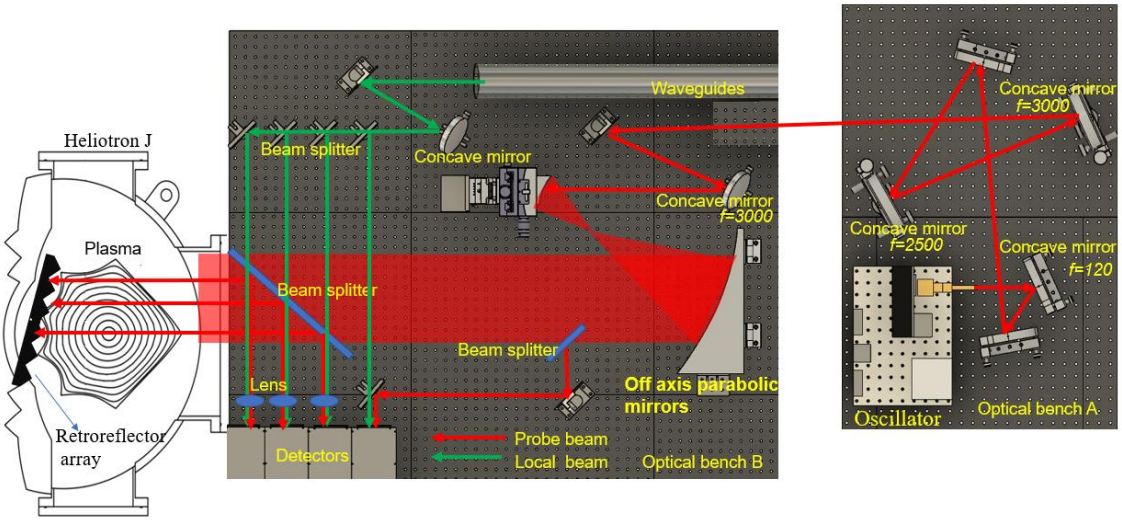

Fig. 4.35 Schematic of a multichannel interferometer. The OAP system extend the probing beam to sheet to realize the measurement.

For the multi-channel interferometer, the influence of the refractive index, especially for the edge channel's measurement should be considered to realize the precision measurements. With the TRAVIS ray-tracing code, the submillimeter wave refraction in the plasma can be obtained. As shown in Fig. 4.36, the refractive index in the plasma with density at $5\times10^{19}m^{-3}$ above 0.98. The influence of refractive index from the plasma can be ignored for the multi-channel interferometer.

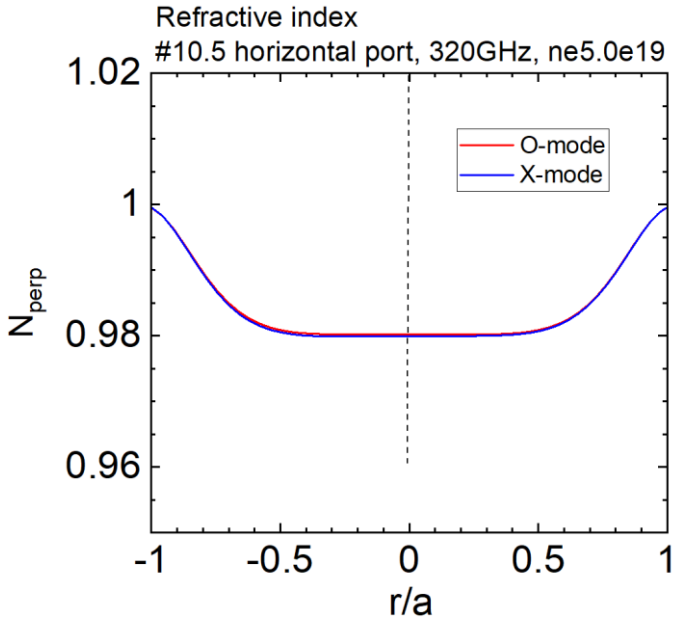

Fig. 4.36 The simulation result of refractive index in Heliotron J with TRAVIS

4.5.2 Transmission efficiency between the optical bench A and B

For the sheet beam produced by the OAP system, the beam intensity will decrease compared to the single-channel setup. To upgrade the interferometer to a multiple channel system, it is necessary to increase the beam power before the OAP system. Therefore, improving the transmission efficiency between optical plate A and optical plate B becomes important.

The beam transmission efficiency can be easily measured with the imaging camera (Terasense Group, Inc.), as shown in Fig. 4.37. The imaging camera has multiple sensitivity bands in the range of 50-700 GHz . The frequency response of the imaging camera is shown in Fig. 4.38. The beam profiles measured by the imaging camera at the entrance and exit of the probe beam waveguide are shown in Fig. 4.39. The beam profile at the inlet of the waveguide has a good Gaussian distribution, which also confirms the accuracy of the optical alignment at the single-channel optical bench A. Integrating the measured results of the two beam profiles, a comparison shows that the transmission efficiency of the waveguide is only 66.7%. By analyzing the factors that influence the transmission efficiency of the waveguide, it can be concluded that the axis of the Gaussian beam should coincide with the axis of the waveguide. However, since submillimeter waves are not visible, achieving precise alignment between the microwave transmission axis and the waveguide axis is extremely challenging.

To enhance the transmission efficiency for multichannel measurement, we have employed large-sized concave and plane mirrors to propagate the beam from optical bench A to optical bench B. For the new transmission scheme, we designed and performed a desktop experiment. The results of the beam transmission calculation using MATLAB are illustrated in Fig. 4.40. The beam is generated by the oscillator and, after size modulation using concave mirrors with focal lengths of 120 mm, 2500 mm, and 3000 mm, it is transmitted to optical bench B. On optical bench B, a concave mirror with a focal length of 3000 is employed to compress the beam size, and a plane mirror is used to adjust the transmission direction towards the OAPI.

During the tabletop test, the imaging camera has been used to measure the beam profile. The profile measurements of the transmitted beam were captured at the edge of the optical bench A and the edge of the optical bench B as shown in Fig. 4.41. The measurement results are presented in Fig. 4.42. Initially, the beam diameter near the source is measured to be 33.45mm. However, as the beam propagates over a distance of 3.5m, the peak power gradually decreases, leading to an increase in the beam diameter,

which expands to 81mm. Comparing the beam integration, the beam transmission efficiency between optical bench A and optical bench B is determined to be 87%. This represents a significant improvement in transmission efficiency compared to using a waveguide. Based on these measurement results, the optical path design is adopted, and the optical components are installed near the Heliotron J.

After the construction of optical bench A was completed, a long focal length concave mirror with a focal length of f=3000 was installed on optical bench B. The beam profile in front of the OAPI was captured using the imaging camera. The measurement results are presented in Fig. 4.43, and it can be observed that the beam profile is approximately Gaussian in shape, indicating that the optical path has been constructed according to the design expectations.

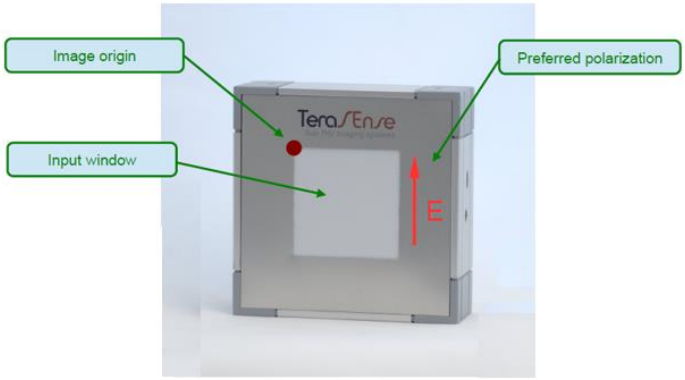

Fig. 4.37 The imaging camera with spectral range 50-700GHz and a sensor size 48 × 48 mm of 32 × 32 pixels.

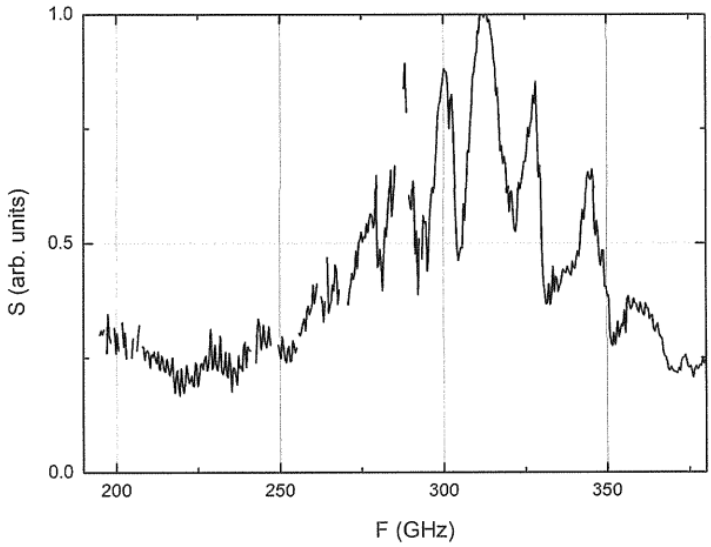

Fig. 4.38 Frequency response of the imaging camera

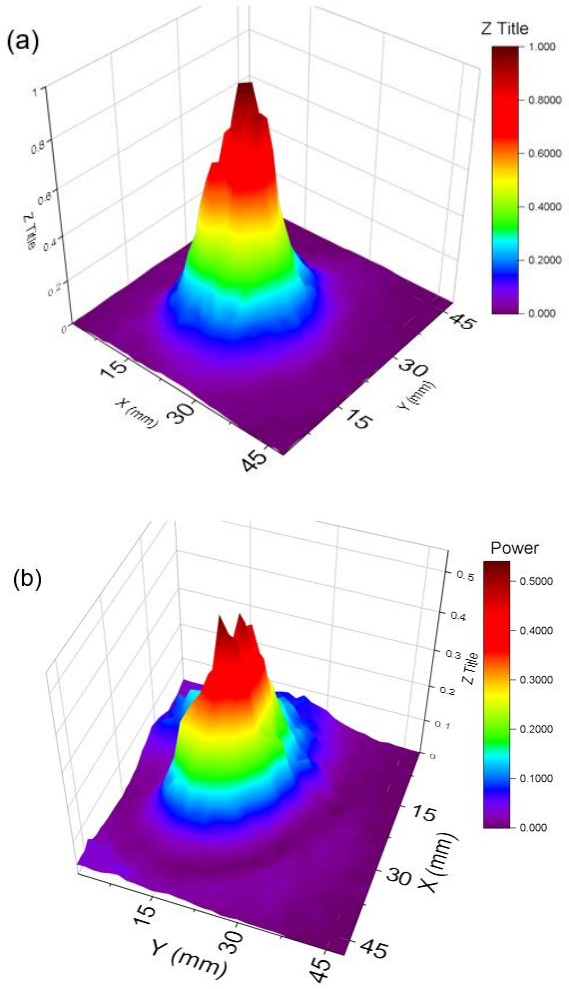

Fig. 4.39. The beam profile measured by imaging camera. (a) the beam profile on the inlet of the waveguide, (b) the beam profile on the outlet of the waveguide.

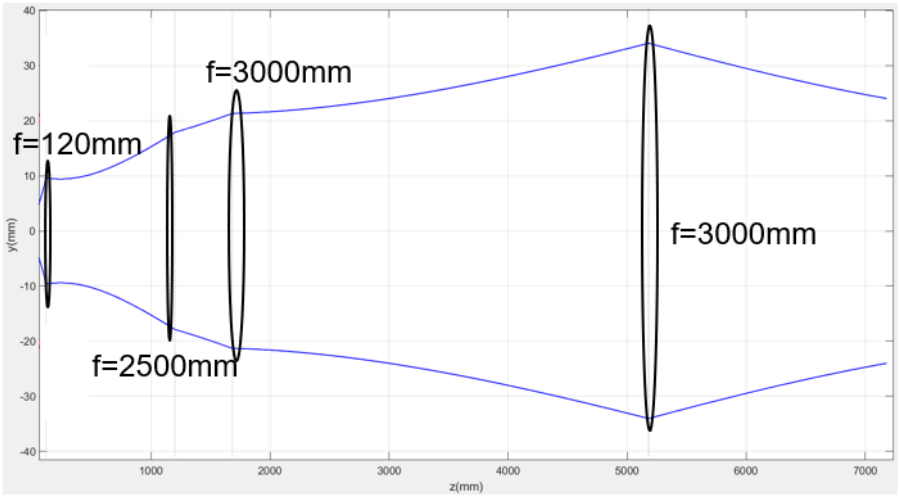

Fig. 4. 40. The optical path design with the big size concave mirrors for beam transmission between optical bench A and B

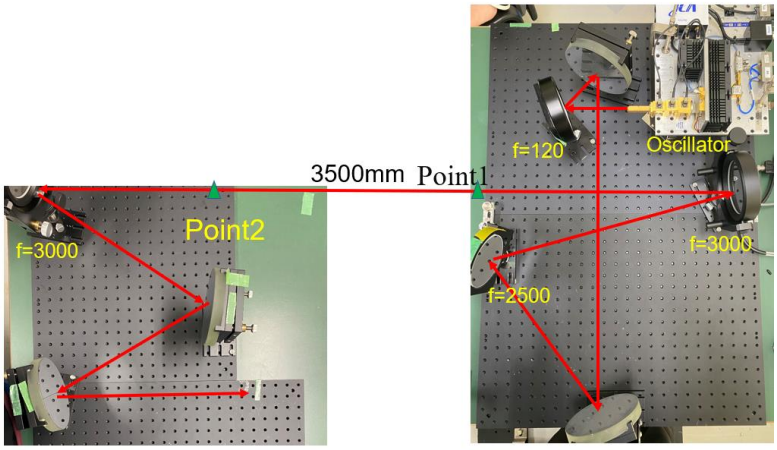

Fig. 4.41. The tabletop test for the new optical path design.

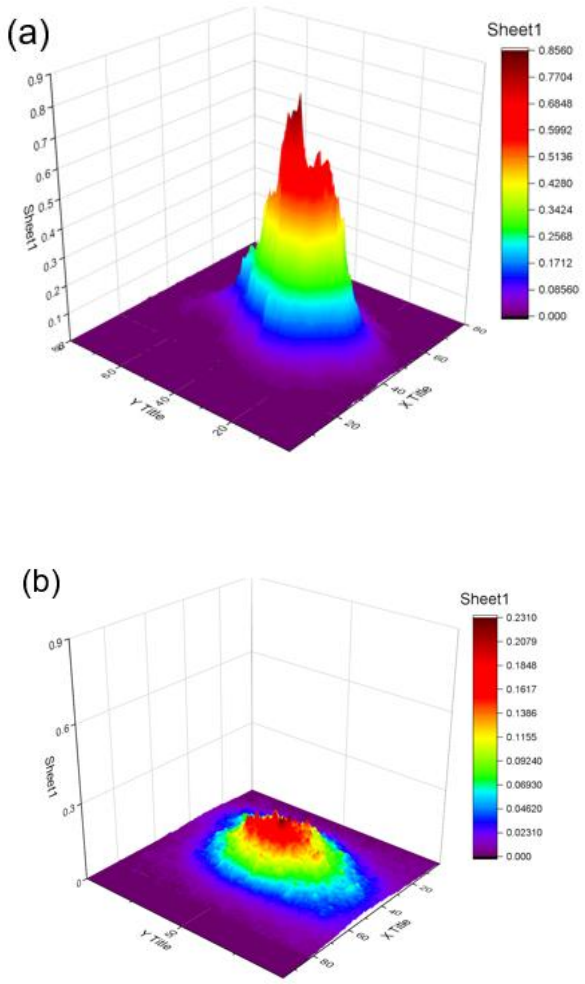

Fig. 4.42. The beam profile measured by imaging camera. (a) the beam profile on the edge of optical bench A, (b) the beam profile on the edge of optical bench B [74].

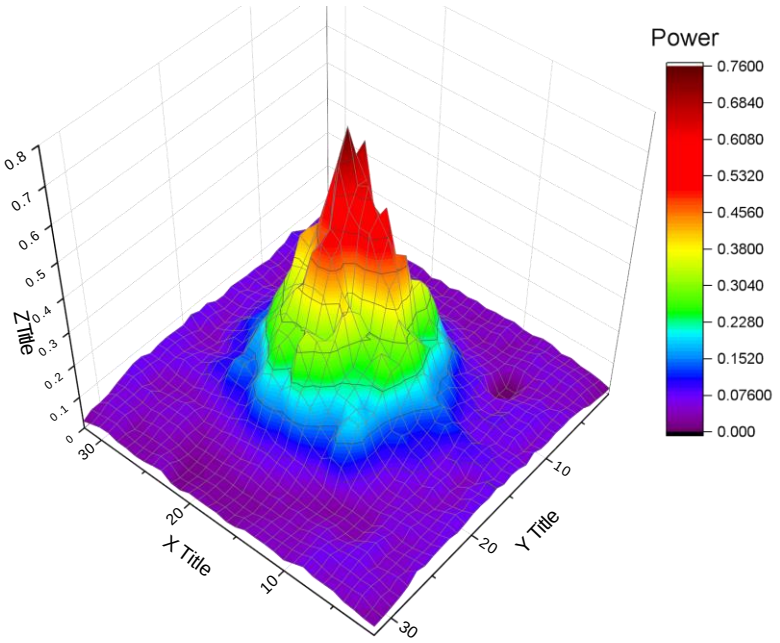

Fig. 4.43. The beam profile measured in front of OAPI.

4.5.3 Off-Axis Parabolic (OAP) system

Compared to the single-channel system, the upgrade of the multi-channel interferometer includes an Off-Axis Parabolic Mirror (OAP) for beam expansion. The OAP is often used as a component to build submillimeter optical paths. It can focus collimated beam / collimated wave with parallel incidence on the focus and then convert submillimeter wave from point light source into a parallel beam.

As shown in Fig. 4.44. (a) and Fig. 4.44. (b), the off-axis parabolic mirror uses the principle of a geometric paraboloid, where incident beams parallel to the axis of parabolic symmetry are reflected and their optical paths will converge at the focal point. It is possible to extend the beam into a parallel sheet beam by two off-axis parabolic mirrors, as shown in Fig. 4.45. The parallel beam incident into the OAP I, converges with the focal point of the parabolic mirror after reflection, and diverges after passing through the focal point. The beam reaches another parabolic mirror with the same focal point, the beam profile increases and is parallel to the symmetry axis after reflection, obtaining a parallel sheet beam of the desired size. The off-axis parabolic mirror is designed using the parabolic equation with the following equation.

$$Y^2 = 4pX, \tag{4.11}$$

where X and Y are the horizontal and vertical coordinates and p is the focal length of the parabola.

After deriving the equation for designing the Off-Axis Parabolic mirror (OAP), we use it to determine the specific design parameters of the OAP system by combining the beam size after passing through the waveguide with the diagnostic window size. Fig. 4.46 demonstrates that for the #10.5 diagnostic port, it is sufficient to cover only the upper portion with the sheet beam, considering the symmetry of the upper and lower structures of magnetic configuration. Moreover, the expansion of the beam results in a decrease in power density. To address this, we establish a design criterion by setting the size of the sheet beam covering the plasma at 0.6 times the corresponding peak beam power. By applying these constraints, utilizing Eq. 4.11, we successfully determine the design parameters of the OAP system [74].

As shown in Fig. 4.47, the focal points of the two parabolic mirrors coincide, and using Eq. (4.11), we can obtain the equation for OAP I.

$$Y^2 = 129.74X\ (0 \le X \le 22.26)\ , \tag{4.12}$$

For OAP II, the equation is:

$$Y^2 = -1065.236X(-115.404 \le X \le -7.709)\ , \tag{4.13}$$

The design of the two OAPs is based on Eq. 4.12 and 4.13. The principle of operation of the OAP is that two OAPs with coincident focal points extend the parallel beam in proportion to the focal length.

Based on the design, the OAP components are produced and shown in Fig. 4.48. Both OAPs are fixed on a 3D moving stage ((Misumi ZLFD series & XYMB series), allowing adjustments in three directions. Additionally, the angle can be finely tuned in parallel to the optical bench by set of αβ swivel stages (Misumi GFWG series). After the

optical alignment is finalized, the sheet beam produced by the OAP system undergoes scanning using an imaging camera. The outcomes of this scanning are depicted in Fig. 4.49.

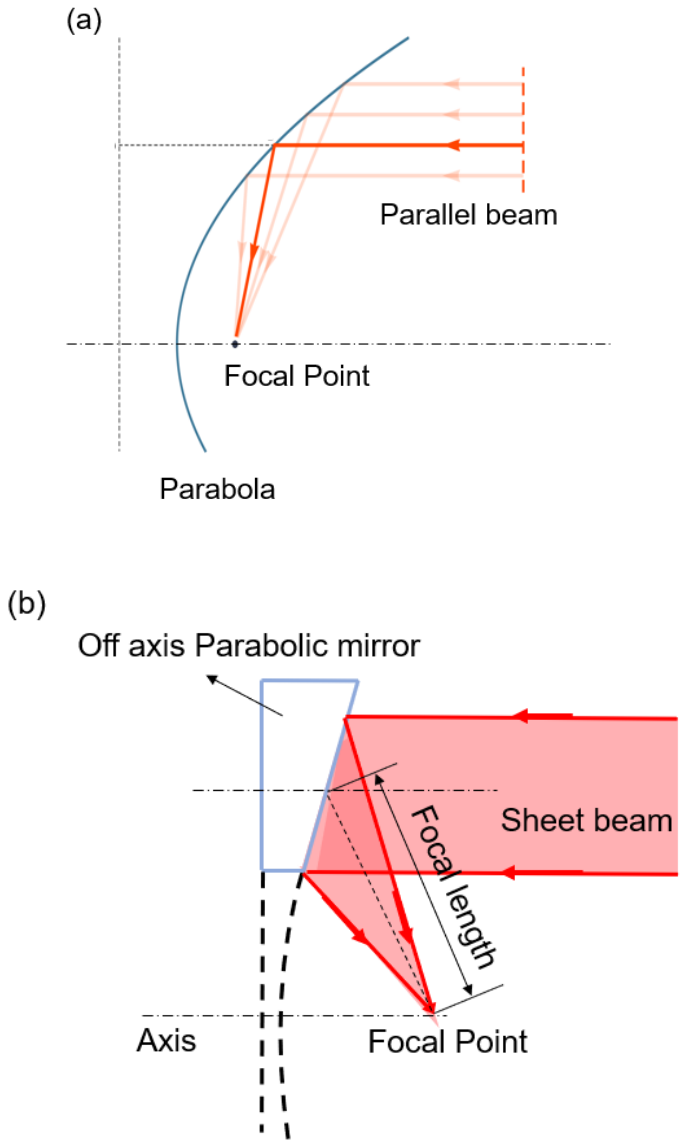

Fig. 4.44 (a)The principle of parabola. (b) The principle of the parabolic mirror. The incident beam parallel to the axis of the parabola will converge on the focal point after its reflection. The off-axis parabolic mirror depends on the principle of parabola convert the parallel beam to a point beam.

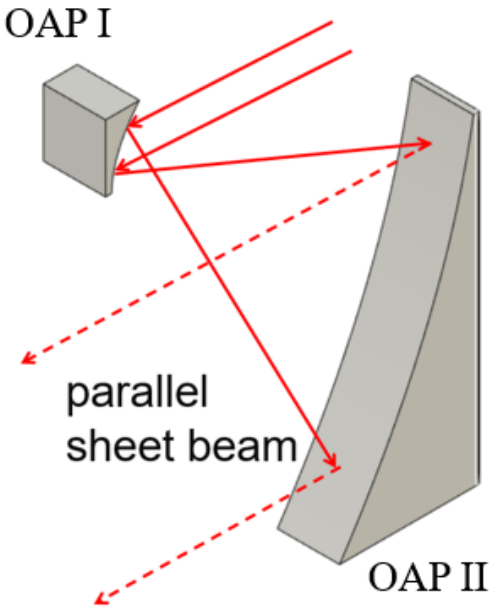

Fig. 4.45 Transformation of sheet beam. The focal points of the two OAPs overlap, and the size of the converted sheet beam is adjusted by the distance between them.

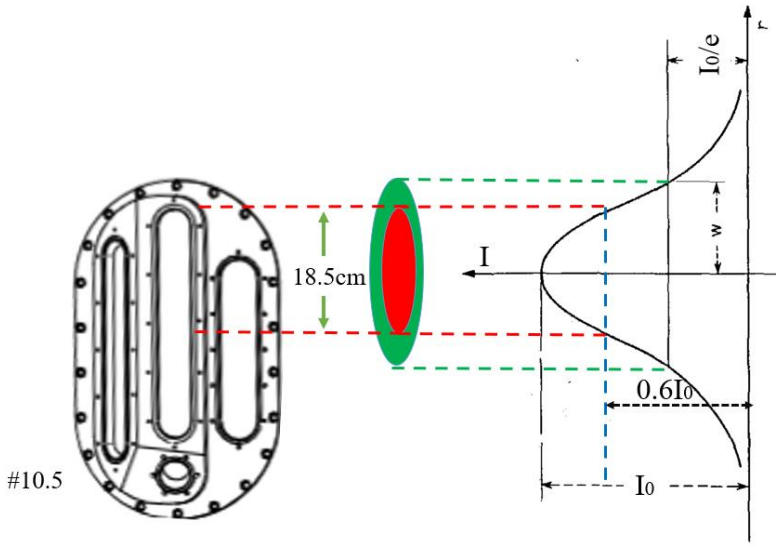

Fig. 4.46 Transformation of sheet beam. The focal points of the two OAPs overlap, and the size of the converted sheet beam is adjusted by the distance between them.

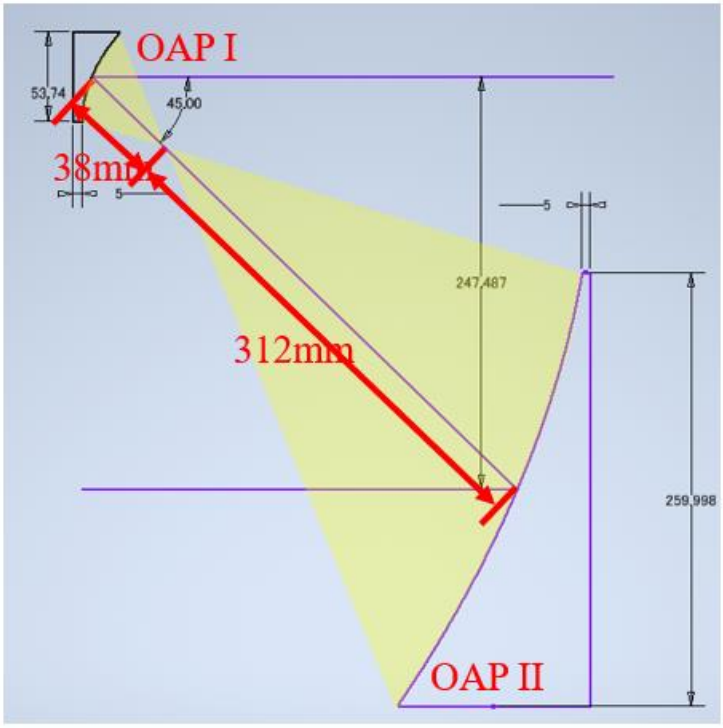

Fig. 4.47 The design of off axis parabolic mirrors.

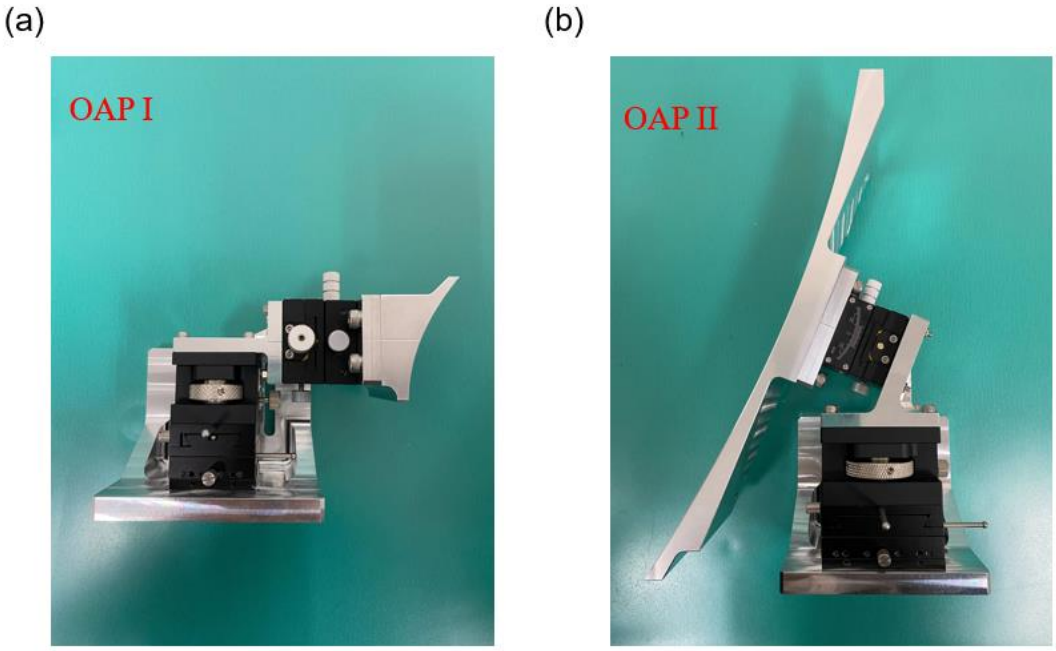

Fig. 4.48 The pictures of OAP I and OAP II.

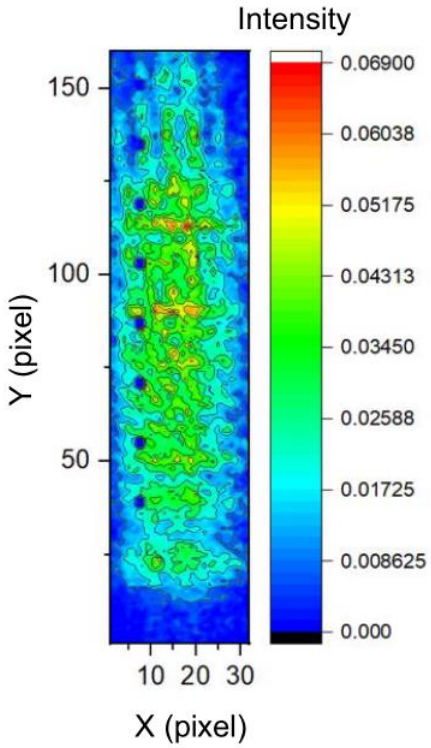

Fig. 4.49 The beam profile of the sheet beam on the optical bench B.

4.5.4 The spatial resolution of the multi-channel system

With the sheet beam, multi-channel measurements can be realized by simply adding detectors at the corresponding positions. However, this setup causes spatial resolution settings and crosstalk effects that affect the final measurement results. In order to achieve accurate measurements and minimize the effect of the crosstalk effect on the measurement results, absorbing material with hole is used to cover the non-measurement area, as shown in Fig. 4.50. Three to four of these materials are placed in front of the diagnostic port of the vacuum chamber and the detector, the number depending on the specific space. This ensures that the detection beam comes from the designed viewing chord. This setting up combined with the lens make the spatial resolution to 22.5mm for this multi-channel interferometer system.

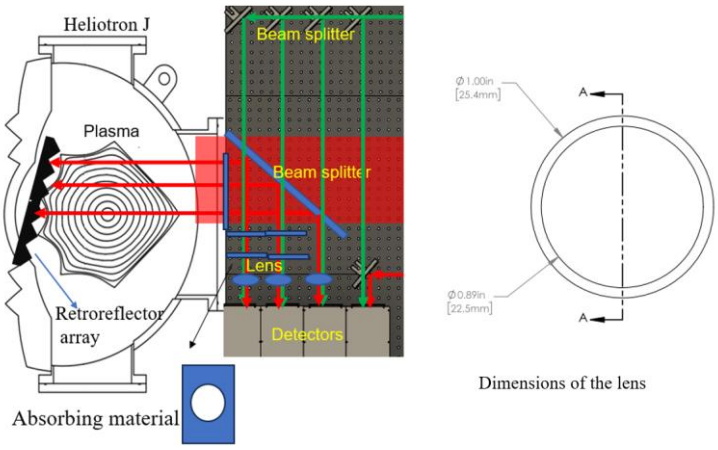

Fig. 4.50 Setting up absorbing materials and the lens

4.6 Discussion

The single channel 320 GHz solid-state interferometer system have been successfully developed for the density measurement operated as commissioning. After extending the beam into a sheet by the OAP system, we achieved the anticipated outcome of enabling two channels of measurements. This accomplishment affirms the accurate realization of the multi-channel interferometer system as its original design.

However, during the plasma experimental, we identified potential enhancement within the system. The utilization of a sheet beam, while advantageous for compactness, introduced a challenge in the form of crosstalk effects, particularly between adjacent channels. To address this issue, we have currently adopted an approach involving the placement of three to four perforated shielding materials in front of the diagnostic port within the vacuum chamber and detector. This strategic positioning effectively shields beams deviating from the designated viewing chord, thereby mitigating the crosstalk effect.

To further improve this system, we propose choosing the location and quantity of shielding material by selectively blocking the beta signals in different measurement areas before the plasma experiment. This additional step promises to further minimize the interference between adjacent channels.

The 320 GHz solid-state source multichannel interferometer as an optimal choice for density measurements in fusion device, as its compact configuration and less maintenance requirements. The incorporation of sheet beam and Michelson-type significantly make the system compacted with few optical components, aligning perfectly

with the spatial limitations often encountered in fusion device. Moreover, the variable IF signals and the position of detectors make the interferometer with adaptable time resolution and measurement positioning capabilities, effectively realizing the diverse measurement requirements of physics experiments.

4.7 Summary

To understand the physics of high-density plasma production, a new 320 GHz multi-channel solid-state source interferometer was designed and constructed for the electron density measurement in Heliotron J. This interferometer is a Michelson-type, based on the heterodyne principle, with two independent solid-state sources. Two solid-state THz sources as the microwave generator can provide up to 50 mW microwave with compacted structure, high stability, and ease maintenance.

The single-channel 320 GHz interferometer was constructed and operated as commissioning before the installation of the multi-channel system. The optical path design depends on the quasi-optical technique, with less transmission losses, suitable for the design of sub-millimeter and millimeter wave transmission in free space. The oversized waveguide connects the microwave sources, located 3 meters away from the magnetic coils and the Heliotron J device, enabling efficient microwave transmission. Concave mirrors and plane mirrors control the position and the size of the beam. The retroreflector array with the compacted structure is installed in the vacuum chamber to reflect the probe beam to recombine with the reference beam to realize the interference measurement.

The single-channel interferometer has been upgraded to a multi-channel one by introducing a pair of OAP mirrors for the beam expansion to a sheet beam to reconstruct the electron density profile. To improve the transmission efficiency between the source and HJ, oversized and long focal length concave mirrors were used to transmit the microwave. With the high transmission efficiency of 87 % and better beam profile, the transmission quality and intensity of the beam are improved to enable multi-channel measurement.

The new 320 GHz multi-channel interferometer system with high time resolution has been developed for the electron density measurement in Heliotron J. During the plasma experiment campaign, we have obtained the data by this new system. The experiment results will be shown in the chapter 6.

Chapter 5

Characterization of a retroreflector array for 320-GHz interferometer system in Heliotron J

A retroreflector array, composed of a cluster of small retroreflectors, is a new-type reflector has the potential to be a vital and effective tool at a spatially limited location on the vacuum chamber wall of plasma experimental devices. The retroreflector array installed on the vacuum chamber wall reflected the probing beam in the original direction to realize the interferometer measurement. To investigate the effect of retroreflector array on the reflected beam properties, a tabletop experiment is performed under the situation where the retroreflector array is composed of 4 mm corner-cube retroreflectors and a 320 GHz submillimeter wave source is employed as a source. This chapter will show the measurement results of the reflected beam from the retroreflector array and estimate the usefulness as the reflector.

5.1 Retroreflector array

Retroreflectors are [75]widely used in various applications such as optical communication [76], remote sensing [77], and aerospace engineering [78], which can compensate for the beam deviation induced by refraction [79]. However, since a retroreflector is composed of a three-perpendicular reflective surface, the thickness of the retroreflector needs to be comparable to the size of effective diameter of retroreflector and hence its application to the spatially limited place is limited in some cases.

The most important feature of a retroreflector is that the incident beam on the reflector can be returned to the source direction. The directional characteristics of the retroreflector are attributed to the total internal reflection with the structure composed of a three-perpendicular reflective surface [79]. As shown in in Fig. 5.1(a), [80], three

mutually perpendicular reflective surfaces form a corner cube to reflect incident beam back to the original direction. Note that, although there are different types of retroreflectors with different surface structures, this chapter focuses on the corner-cube style. The feature of retroreflectivity is essential in the practical application when a reflector is required since careful alignment is unrequired with it. A disadvantage of retroreflector is that the thickness of retroreflectors needs to be comparable to the size of the reflector itself and therefore enough spatial area is required to utilize it.

A retroreflector array is a reflector composed of several individual small corner-cube structures arranged on a reflection plane [81]. Since each corner cube structure and the thickness of the retroreflector array are substantially smaller than those of single retroreflector, which potentially expand the application of the reflector to be utilized even in the location with limited space in fusion plasma experiment [82,83]. Multiple retroreflector elements are arranged in a reflection plane, as shown in Fig. 5.1 (b), and hence the array is much thinner compared to one single retroreflector and other reflectors including a holder with some alignment functions. This is favorable to install it at the location with limited space.

However, a periodic structure of retroreflector array can induce a diffractive grating effect. The effect depends on the ratio of incident beam wavelength to periodic structure size of retroreflector array, as pointed out in the past numerical study [81]. When incident beams over the size of the retroreflector element, the reflected beams from many corner reflectors interferes each other like a reflection from diffractive grating, resulting in the interference pattern that may appear on the reflected beam profile. Such a grating effect is ignorable when the wavelength is much smaller than the size of periodic structure but should appear more prominently when the wavelength becomes comparable to the scale of the periodic structure of retroreflector. Although this tendency has been previously mentioned in the past study, experimental characterization has never been done, in particular, motivated by its application to interferometry in fusion plasma experiment.

Let us consider the typical situation of interferometry in fusion plasma experiments, where commercially available microwave or submillimeter sources with corresponding frequencies of 100-300 GHz and wavelengths of approximately 1 to 3 mm. The thickness of retroreflector array should be 5 - 15 mm from the processing accuracy of machining in present day, and each retroreflector size of array is still larger but comparable to the wavelength. This condition is expected to be transient, as retroreflector array behave as a retroreflector or as a diffractive grating, depending on the ratio of wavelength and the periodic structure size of an array.

The reflective grating consists of reflecting elements separated by a distance comparable to the wavelength of incident beam. The constructive interference will be created with the geometrical path difference between beam from adjacent elements equal the wavelength of the incident beam or integral multiple, as shown in Fig. 5.2 (a). The path difference between the adjacent elements is $\mathrm{d}sin\theta_m - \mathrm{d}sin\theta_i$. For the incident monochromatic plane electromagnetic wave ,the reflection diffraction grating will give rise to a discrete number of reflected waves. The grating equation is as follows [84],

$$d(sin\theta_m - sin\theta_i) = m\lambda, \tag{5.1}$$

where d is the grating groove size, λ is the beam wavelength, θ_i is incident angle on the grating and θm is the diffracted angle for diffraction order m. The m number can be positive and negative. Fig. 5.2 (b) shows a typical reflective diffraction grating and the diffracted beam and a diffractive grating reflect mono-frequency microwave, resulting in the emergence of an interference pattern. For the incident monochromatic electromagnetic wave, the reflective diffraction grating give rise to a discrete number of the reflected wave as an interference pattern and the local maxima of an m-th order peaks appear on the reflected beam profile at the angle where this equation is satisfied [81]. At $\theta_{m=0} = \theta_i$, the 0-th order diffraction beam corresponds to a specular diffraction beam having the highest power [85]. The higher-order diffraction has a lower power, and the envelope of diffracted beam peaks are distributed within a Gaussian function, as shown as a dotted line in Fig. 5.2 (b) [85]. The equation indicates the diffraction characteristics are dependent on the grating period and the incident wavelength. For the retroreflector array with the periodic structure, the grating effect is more prominent when the wavelength of the incident beam is comparable with the periodic of the retroreflector array [84,85].

Unlike a grating used commonly, it is expected that a retroreflector array can reflect the incident beam in its incident direction dominantly due to the property of a retroreflector although the diffraction effect caused by its periodic structure disperses the reflected beam [85]. As illustrated in Fig. 5.2 (c), after reflected at the retroreflector array, the diffracted beam forms discrete peaks in the original direction but the most of beam power is concentrated on the peaks directed to the incident direction, forming an approximate Gaussian envelope [81]. However, experimental characterization of the reflection from a retroreflector array has never been done before to investigate the diffraction effect and retroreflectivity discussed here. Experimental characterization of the reflected beam profile from the retroreflector array is, therefore, required under such

a transient situation mentioned here.

5.2 Experimental setup

A tabletop experiment has been conducted to investigate the spatial distribution of reflected beam profile and diffraction effect caused by retroreflector array with the aim of assessing its usefulness for interferometer measurement.

The experimental setup in the tabletop experiment is shown in Fig. 5.3(a). A solid-state oscillator (VDIE0029, AMC 630, Virginia Diodes, Inc.) provides a 320 GHz submillimeter wave with a 50 mW output power at maximum. A Gaussian beam with a diameter of ~ 36 mm is injected into the retroreflector array through a concave lens to make the beam parallel. The 50 × 50mm retroreflector array in Fig. 5.3(b) consists of a bunch of small corner cubes with each structure of dimensions of 4 × 4 × 4 mm, where the corresponding periodic distance d= 5.66($= 4\sqrt{2}$) mm as a grating as shown in Fig. 5.3(c) (Fig. 5.3(c) is the retroreflector array installed onto the Heliotron J vacuum chamber. The thickness is different from the one for test). The surface structure of retroreflector array was manufactured by numerical control machining.

The reflected beam from the retroreflector array is transferred into the imaging camera using a beam splitter (polyester) with ~50 % transmission efficiency. A THz imaging camera with a measurable spectral range of 50-700GHz (Terasense Group, Inc.) is placed after the reflection from the beam splitter. The distance between the retroreflector array and the imaging camera is 400mm, and within this distance, the beam diameter varies by approximately 10%, and the beam can be considered as a parallel beam approximately.

In this setup, the incident angle to the retroreflector array, θi, is controlled by rotating the optical stage of the array since the reflected beam profile depends on the incident angle as the grating equation indicates. The reflected beam profile is measured with the imaging camera at every different angle.

5.3 Characterization of retroreflector array on tabletop experiment

The experiment aimed to characterize the property of a retroreflector array as a retroreflector and a grating. The beam incident on the retroreflector array is a Gaussian beam with a diameter of 19.5 mm. Typical beam profiles with some different incident

beam angles are shown in Fig. 5. 4. Here the profile is obtained by scanning the imaging camera with 480 mm perpendicular to the beam propagation direction (defined as "X-direction" here) and the two-dimensional profile obtained is integrated in Y-direction. Fig. 5.4 (a) shows the one-dimensional beam profiles at four different incident angles and the same Fig. 5.4 (b) is plotted against the angle θ displaced from the original incident direction. The blue hatched area corresponds to the incident beam width when the beam is reflected at the mirror, instead of retroreflector array.

Two peaks (or three) are observed, and the peak oriented most toward the original incident direction has stronger power than that of other peaks. By varying the angle of retroreflector array, namely, the incident beam angle, the peak positions continuously shift according to the angle. As a result, the strongest peak moves away from the direction of incidence and becomes weaker, and another peak becomes stronger and is oriented toward the direction of incidence. Thus, the peak directed towards the original incident direction always remains strongest, resulting from the property as a retroreflector. These two peaks are spitted beams generated by the grating effect, which can be evaluated from eq. (1). The grating equation can be rephrased as $\theta_m = m\lambda/d + \theta_i$ using a Taylor expansion, and hence the displacement between m-th and $m+1$-th order peaks should be ~ 10 degree when d and λ are 5.66 mm and 0.937 mm, respectively. To suppress probe beam deflection caused by the plasma refraction, a submillimeter wave with a wavelength of 0.937 mm was employed as the source. The period length of the retroreflector array determines its thickness, which should be larger than the wavelength, but should be as thin as possible to avoid the plasma-material interaction inside the vacuum chamber in the fusion device. Considering the factors above, the dimension of each corner cube is chosen to be 4 x 4 x 4 mm, corresponding to the period length of 5.66 mm. The observed displacement between the different m-th order peaks is well consistent with the one calculated with the grating equation. We emphasize again that, although the beam is spitted into discrete peaks, the functionality as a retroreflector is kept consistent to reflect the beam power predominantly in the incident direction, regardless of the angle of retroreflector array. This property, mentioned in the past numerical studies found in references77 and 78, is experimentally demonstrated for the first time.

The reflectivity of the main reflection may be high when the reflected beam is closer to the original direction of incident beam after the retroreflector array. The reflectivity of metals such as SUS 316 is almost 99 % for 320 GHz at perpendicular injection, and the reflectivity is high enough to neglect the ohmic loss [86,87,88]. For a more thorough examination of the retroreflector array's reflectivity, it should be noted that the reflected

beam will exhibit a two-dimensional distribution upon interaction with the array. Since the reflectivity may be different in non-perpendicular cases, an accurate estimate of the reflectivity at the retroreflector array is future work.

Subsequently, a dependence of the beam distribution on the incident angle was investigated by continuously varying the angle on the retroreflector array. A Gaussian beam with a diameter of ~ 36 mm is injected into the retroreflector array. The imaging camera was fixed at the original incident direction after the beam splitter, while the retroreflector array was rotated in the experimental setup shown in Fig.5.3 (a). Fig. 5.5 (a)-(f) illustrates the reflected beam profiles within a 5-degree range at every 1 degree. As the angle of incidence changes, the beam position shifts continuously towards the rightmost side of the imaging camera and another peak appears from the leftmost side. This indicates that when an *m*-th order peak is observed, then the peak disappears, and (*m*+1)-th or (*m*-1)-th order peak appears instead within the observable range of the imaging camera while rotating the retroreflector array. Although the grating effect induces some discrete peaks, regardless of the angle of incidence on retroreflector array, reflected beam power focuses into an *m*-th order peak oriented most toward the original incident direction, resulted from the property as a retroreflector. The beam profile of the reflected beam is influenced by diffraction effects, leading to a distinct alteration of its profile after reflection on the retroreflector array, which results in a deviation from the Gaussian beam profile.

To evaluate the displacement of the reflected beam from its original direction, the peak position is plotted as a function of angle θ, where the angle θ is defined with respect to the incident beam direction, as shown in Fig. 5.6(a). The strongest peak position with *m*-th order is plotted as a function of θ with respect to the incident beam direction.

When the reflected beam power is focused on an *m*-th order peak oriented toward the original incident direction, this condition can be expressed as $\theta_m \sim -\theta_i$. Thus, the grating equation gives a condition $\theta_i \sim m\lambda/2d$ where an *m*-th order peak beam is oriented into the incident direction, which exhibits that the strongest peak with different *m*-th order appears every 5-6 degrees approximately while varying incident angle. The peak position evaluated in the experiment and the predicted position of *m*-th order peaks from Eq. (1) are compared in Fig. 5.6 (b). The incident angle is controlled from 0 to 35 degrees. In the figure, the red circles and black lines indicate the experimental results against different incident angles and the calculated results assuming d = 5.1 mm, respectively. Although the assumed d value is displaced 10 % from the designed value of d (~5.66 mm), the error is within the reasonable range considering machining accuracy. The experimental

observation is well consistent with the calculated result based on Eq.(1), indicating that the discrete peak is induced by the grating effect, and nevertheless, reflected beam power dominantly focuses into an *m*-th order peak oriented most toward the original incident direction.

5.4 Application of retroreflector array to a Michelson interferometer in Heliotron J

The retroreflector array was applied to the Michelson interferometer system in Heliotron J. Since a Michelson interferometer system requires the probing beam to return to its original path to suppress the beam deflection caused by plasma refraction, the beam displacement, caused by the retroreflector array about ~ 5 degree deviation under the present λ/d ratio, needs to be minimized. To reduce the effect, a lens (50 mm diameter and f= 75 mm) is introduced to converge the reflected beam in front of a detector.

In the tabletop experimental setup, depicted in Fig. 5.3 (a), the retroreflector array is positioned 405 mm away from the imaging camera. Additionally, a lens is placed between the beam splitter and the imaging camera, with a separation distance of 75 mm from the imaging camera. The lens can increase the detected signal intensity and improve the beam profile as well as reduce the beam displacement. Figure 5.7 (a) and (b) show the intensity of the reflected beam from the retroreflector array after passing through the lens at incident angles of 0 degree and 4 degree, respectively. Figure 5.7 (c) shows the one-dimensional profile with a Gaussian fitting curve. Comparing it with the profile without the lens shown in Fig. 5.7 (d), the intensity is almost seven times as high as the case without the lens, and the beam profile is also approximately Gaussian, which improves the quality and intensity of the beam, and compensate the beam displacement induced by the grating effect.

Furthermore, the dependences of reflected beam intensity on the incident angle with and without the lens are characterized and compared by rotating the retroreflector array within a range of -35 degrees to 35 degrees. In Fig. 5.7(e), the peaks at different incident angles are illustrated, where the black square and red circles indicate the peak value without and with the lens, respectively. The zero angle is defined as the point at which the maximum intensity is obtained at the center of the imaging camera. By employing the lens, the beam reflected from the retroreflector array, undergoes minimal beam deviation relative to its original direction. As shown in Fig. 5.7 (b), the position of the beam peak

deviates from the original direction by around 3 mm, but it remains within the central region of the imaging camera. However, the beams without the lens deviate from the center of the imaging camera, even outside the receiving area. The small deviation in the case with a lens also results in a larger detected signal intensity compared to the case without a lens. Consequently, the power variation caused by the diffraction-induced beam displacement is effectively suppressed, maintaining the signal level higher than the noise level even when the reflected beam is not oriented exactly to the detector, as shown in Fig.5.7(e).

Using the detector system combined with the lens, a 320 GHz interferometer system with the retroreflector array was installed to Heliotron J and applied to practical density measurements. Figure. 5.8(a) shows the interferometer system in Heliotron J [68] and Fig. 5.8(b) shows the retroreflector array placed on the vacuum chamber wall of Heliotron J with the same surface dimensions (4 mm x 4mm x 4mm corner-cube structures) as in the tabletop experiment [67]. To ascertain the shape of the vacuum chamber wall at the reflector's position, a total of 160 coordinate points were measured employing a laser range finder, as shown in Fig. 5.8(c). Subsequently, the incident angles at these points were accurately determined. At the midplane, the measured angle is around 0.6deg, while the angle at the edge of the retroreflector is almost 8deg. A 100 mm diameter lens is set in front of the detector to reduce the effect of beam displacement induced by the diffraction effect on the experimental results.

5.5 Discussion

For the first time, we characterized the reflected properties of retroreflector array with the periodic size comparable to the wavelength of incident beam. The reflected beam is separated into different beams due to the grating effect, however, it is affected by the structure of the reflector so that the reflected energy is concentrated close to the original direction.

Our measurement and discussion focus on the one-dimensional reflected beam properties induced by the one-dimensional grating effect. But the two-dimensional effect due to the two-dimensional periodic structure of the retroreflector array was also observed. The two-dimensional measurement will be done next step to deeply research the properties of the retroreflector array. Based on prior numerical studies, it has been established that extending the period length of the individual retroreflector structure to a

notable amplification in the power of the reflected beam, ultimately converging it towards the original direction. However, to refine the directionality of the retroreflector array and consider the limit space inside the vacuum chamber, additional simulations and experiments are imperative. These subsequent investigations will be instrumental in advancing our understanding and optimizing the performance of the retroreflector array.

In numerous cases, obtaining multi-channel results for measurements of physical parameters necessitates the use of compact retroreflector arrays as the reflector. This choice aligns seamlessly with the requirements of experiments, offering a more effective solution especially in the location with limited space.

The retroreflector array is mounted on the wall of the vacuum chamber, and its surface is affected during plasma experiments. In wall-conditioning experiments, it is more likely to pollute its surface, thus affecting its surface reflectivity. The retroreflector array in the vacuum chamber has undergone four years of plasma experiments, and possible contamination of its surface could affect its reflective properties, requiring measurement of its surface reflectivity for further analysis.

5.6 Summary

In this chapter, we have experimentally characterized the properties of a retroreflector array in a tabletop experiment, motivated by its application to the interferometry in a fusion plasma experiment. A THz imaging camera was used to measure the reflected beam profiles from the array at different incident angles. For the first time, we have experimentally demonstrated that the retroreflector array exhibits combined functions as a retroreflector and a grating. The retroreflector array diffracts the beam and produces discrete peaks like a grating, which is predicted from a simple grating equation. However, almost all the power is converged into a single peak that is oriented the most toward the original incident direction and this property could be caused by the surface structure of each retroreflector. The deflection between the incident beam and the reflected beam depends on the λ/d ratio, and the angle is 5 degrees under our present condition. This influence of deviation is not ignorable in some cases, however, is controllable considering the beam wavelength, retroreflector-period, and distance between a reflector and detector for minimizing the impact. A focusing lens in front of a detector can be one of the options to suppress the impact of the grating effect. Furthermore, the interferometer with the same retroreflector array as in the tabletop experiment has been developed in Heliotron J and successfully applied to the density measurement,

which demonstrates that the retroreflector array can be a convenient and effective option as an instrument for the interferometer system in fusion research.

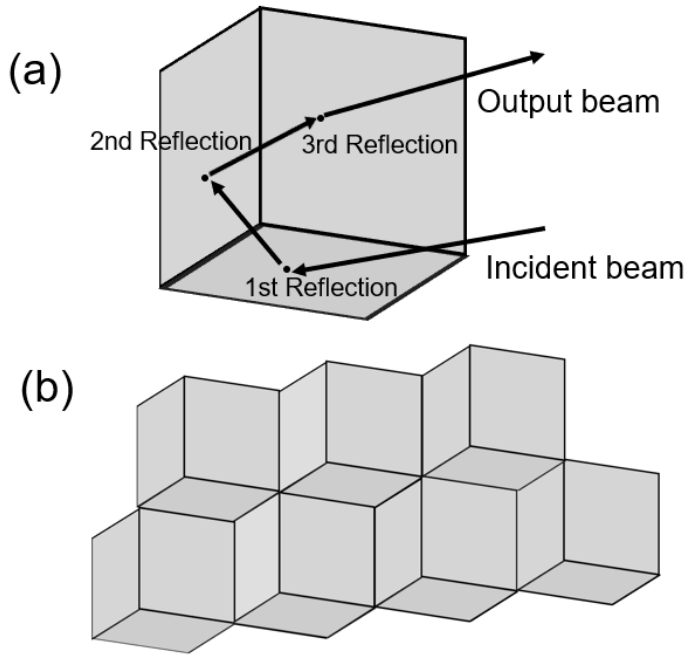

Fig. 5.1. Schematics of retroreflector array, (a) Principle of retroreflector, (b) Retroreflector array [89].

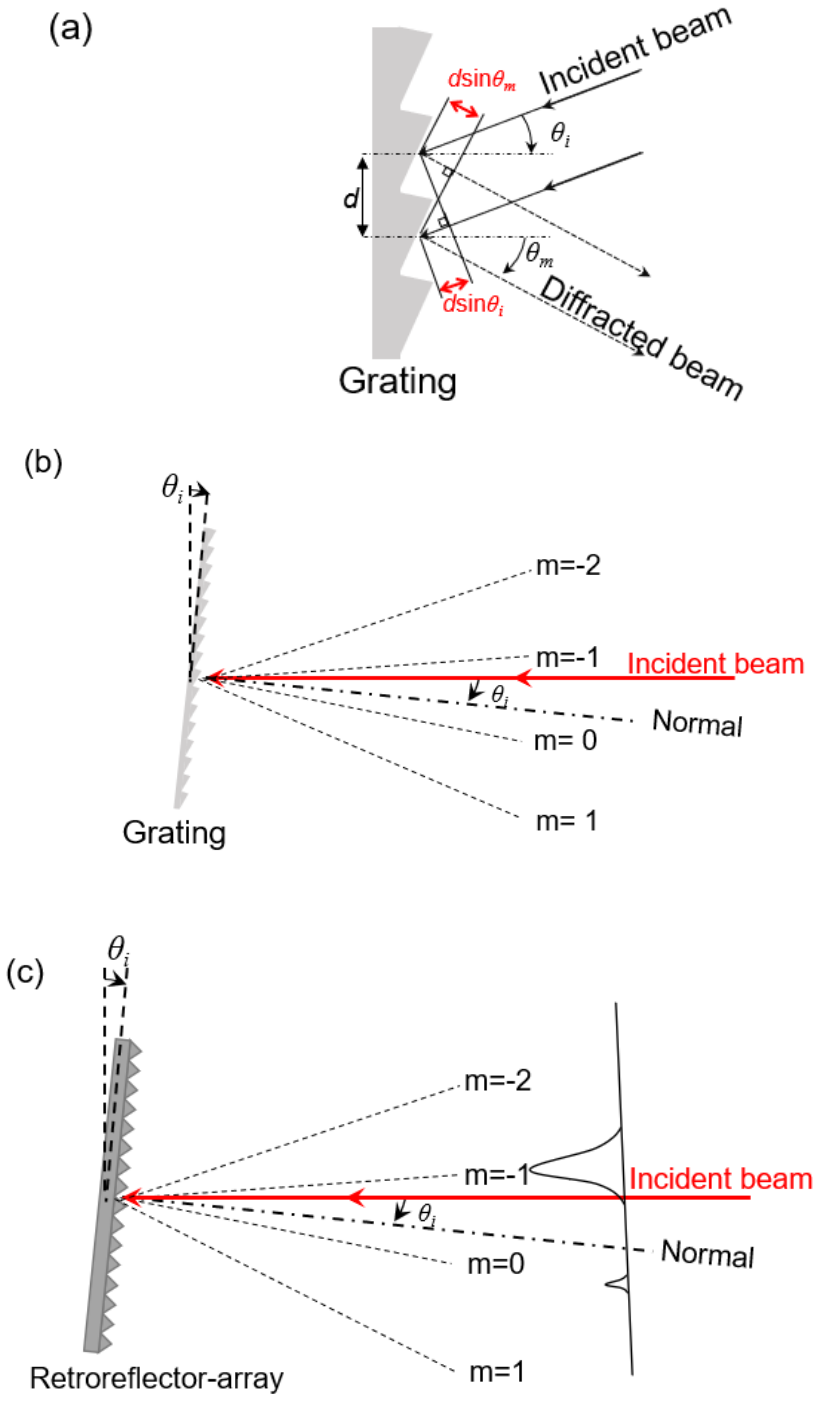

Fig. 5.2. (a) Principle of reflective diffraction grating where θ_i is the incident angle, θ_m is the diffraction beam, m=0,±1,±2... is the m-th order of diffraction beam.(b) Schematic of reflected beam from diffraction grating, and (c) Schematic of reflected beam from retroreflector array when the λ (wavelength) and d (retroreflector period) are comparable [89].

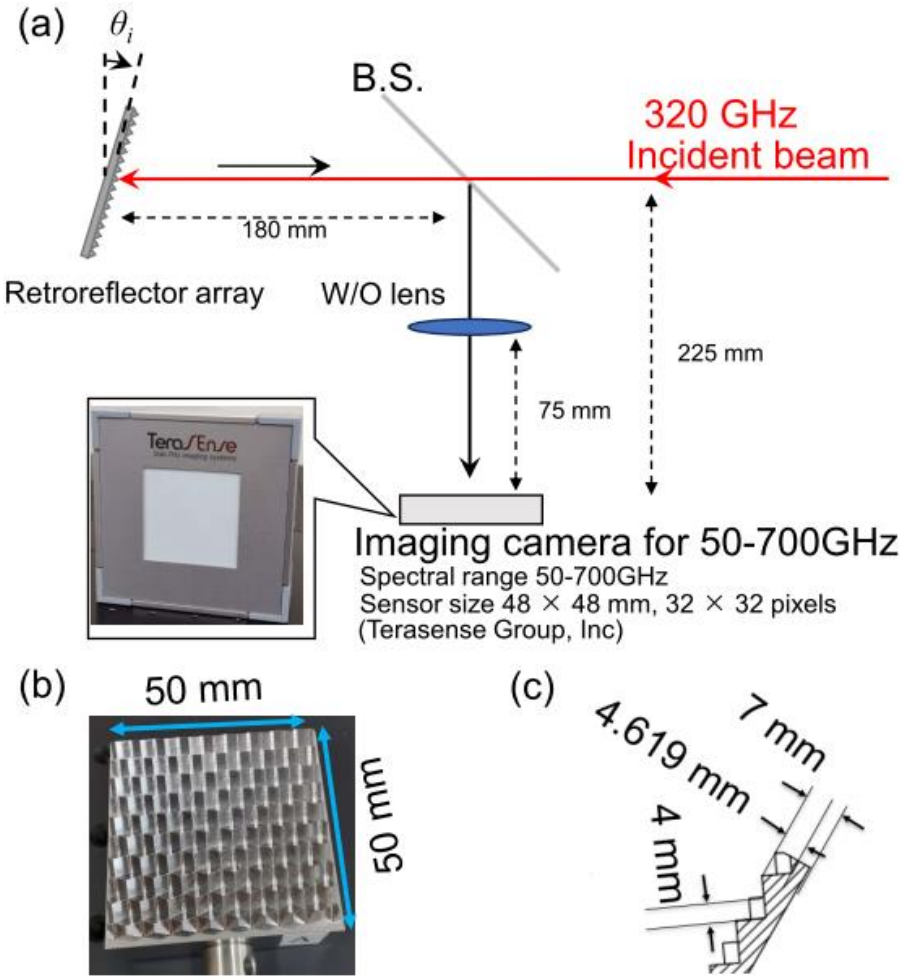

Fig. 5.3. (a) Experimental setup of tabletop test, (b) Retroreflector array used in the tabletop test, (c) Dimensions of the retroreflector array [89].

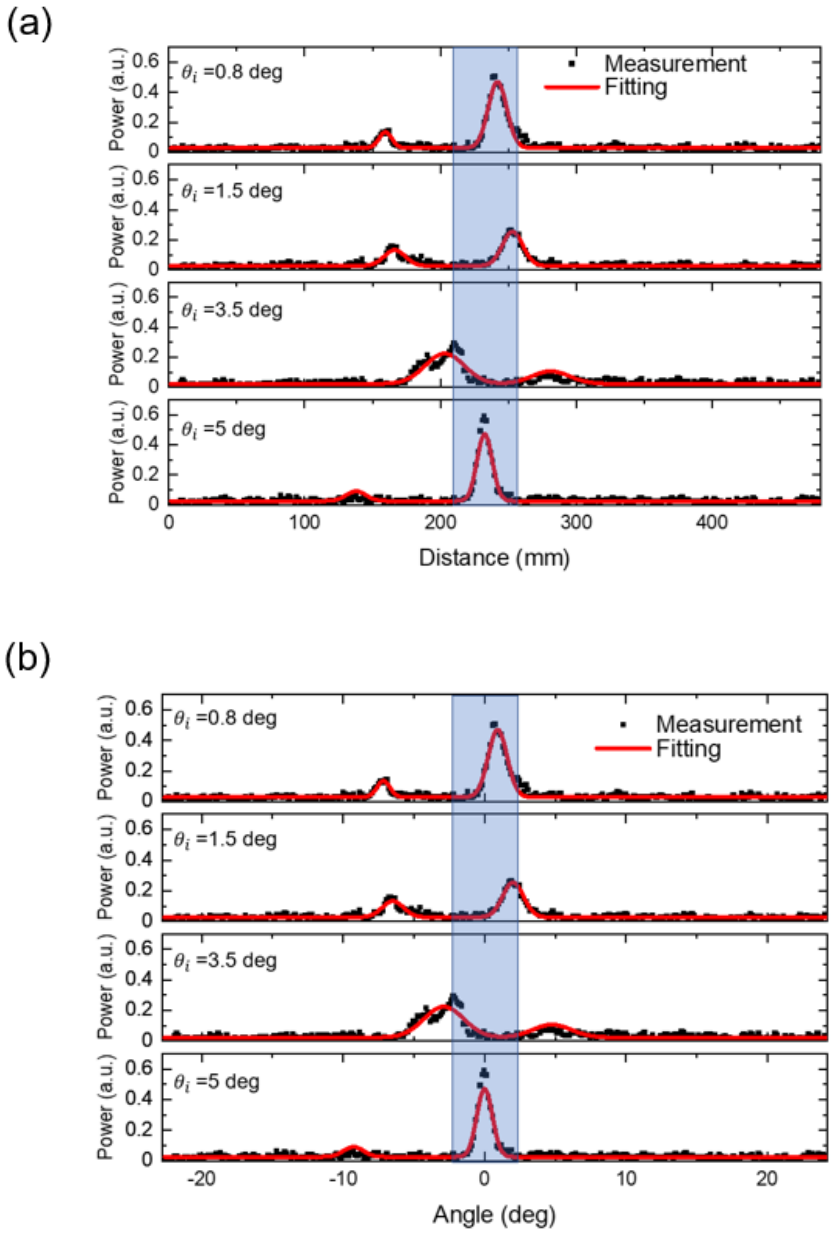

Fig. 5.4. (a)Intensity profiles of the diffraction beam with different incident angle at θ_i =0.8,1.5,3.5 and 5 degree. The results are obtained with scanning the imaging camera position (b) The same figure plotted against a displaced angle θ_i from the original incident direction. The black squares are the measurement results, and the red lines are the fitting curves using Gaussian. The blue hatched area represents the correspondent beam width if the beam is reflected from a plane mirror instead of retroreflector array [89].

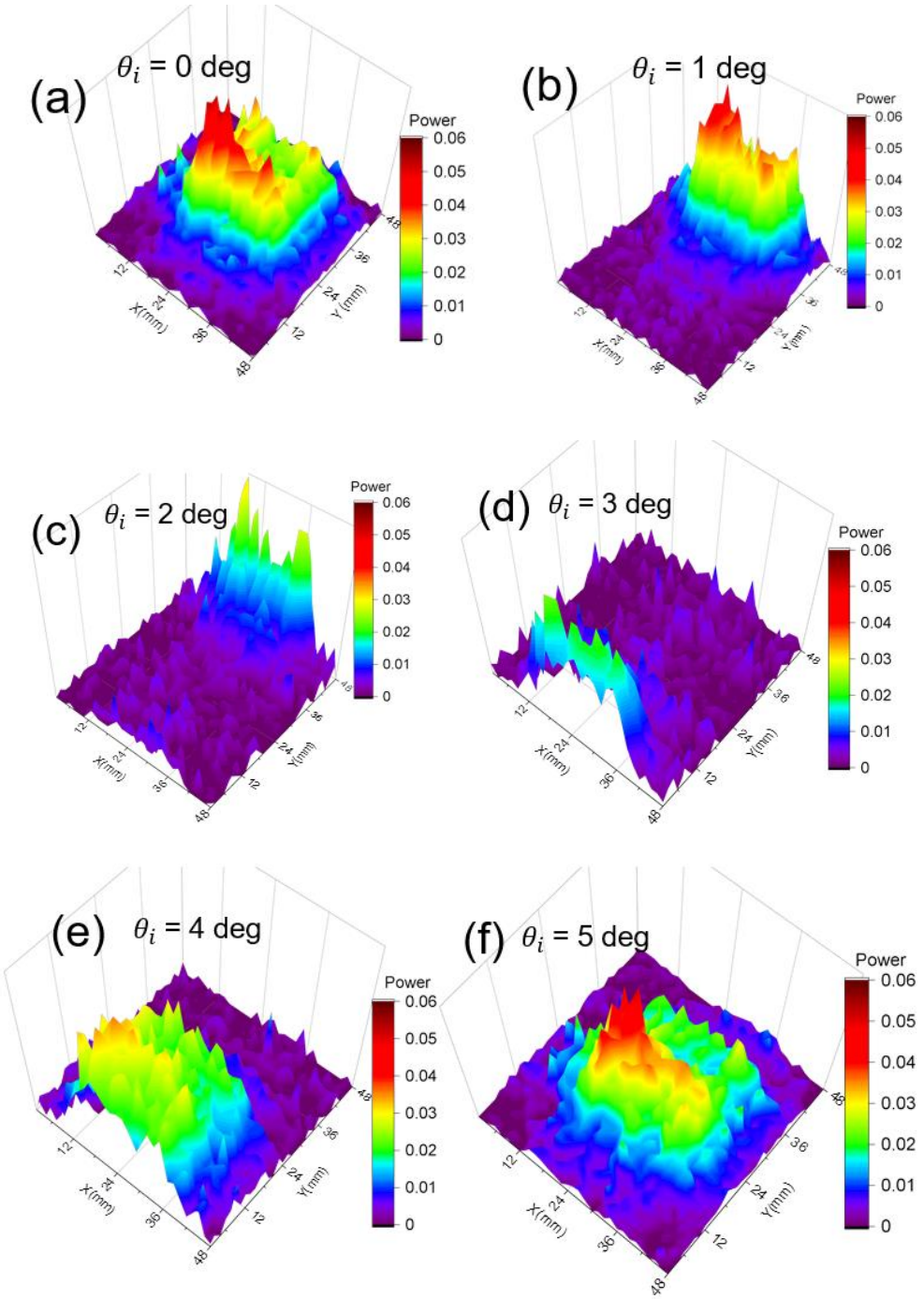

Fig. 5.5. Reflected beam profiles at different incident angle from 0 deg to 5 deg [89].

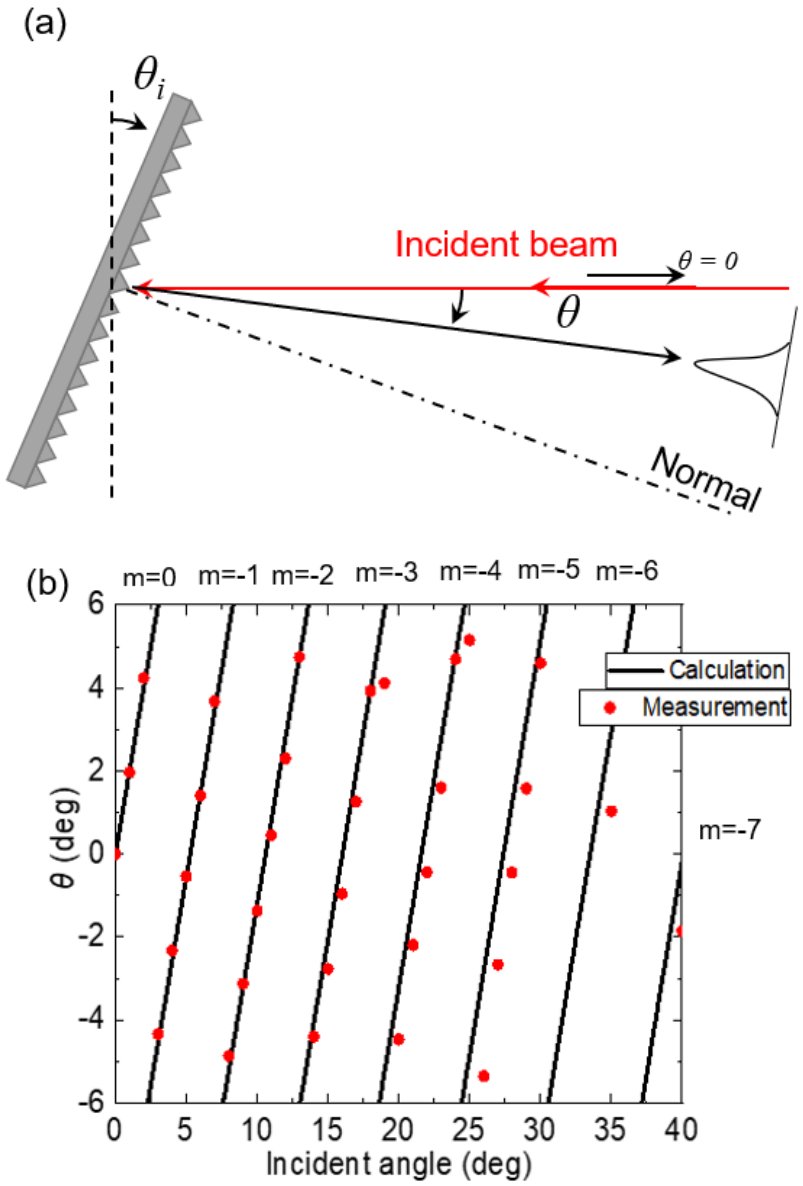

Fig. 5.6. (a) Schematic of experiment for incident angle dependence of reflected beam profile, where θ_i is the incident angle and θ is the displaced angle from the original direction. (b) The dependence of m-th order peak position θ at every incident angle θ_i.The red circles are the measurement results, and the black lines shows the calculation results based on the eq.(1) assuming d=5.1 mm. As the incident angle increases, the higher m-th order peaks appear alternately [89].

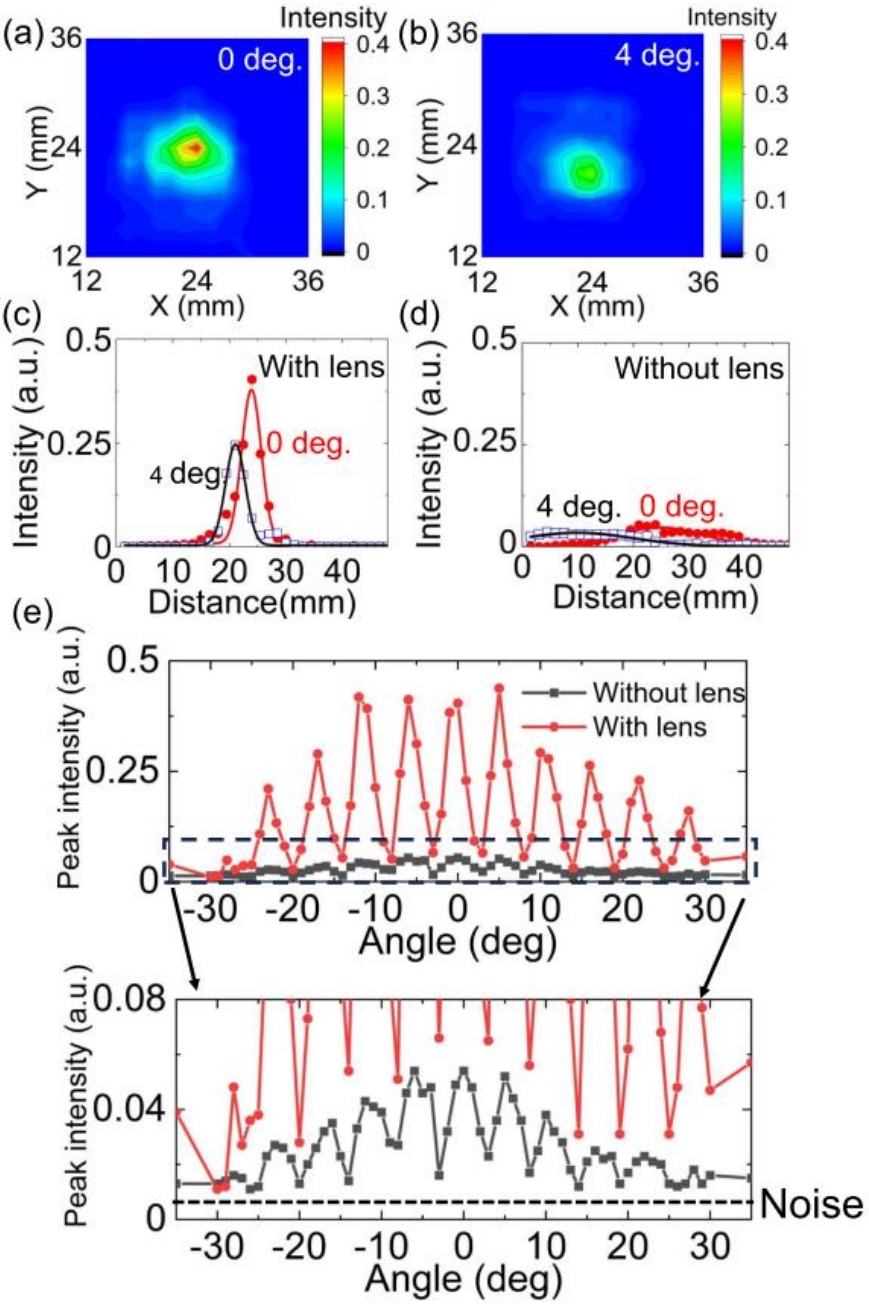

Fig. 5.7. (a) The beam profile obtained with the imaging camera where a lens with 50 mm diameter and f= 75 mm is placed in front of the imaging camera with an incidence angle of 0 deg. (b) The beam profile with a lens at an incident angle of 4 deg. (c) One-dimensional beam profile with a fitting curve of the beam with the lens at incident angles of 0 deg and 4 deg, where solid red circles and blue hollow squares represent measurements of 0 and 4 deg, respectively. (d) One-dimensional beam profile with a fitting curve of the beam without the lens at incident angles of 0 deg and 4 deg. (e) The peak intensity with different incident angles [89].

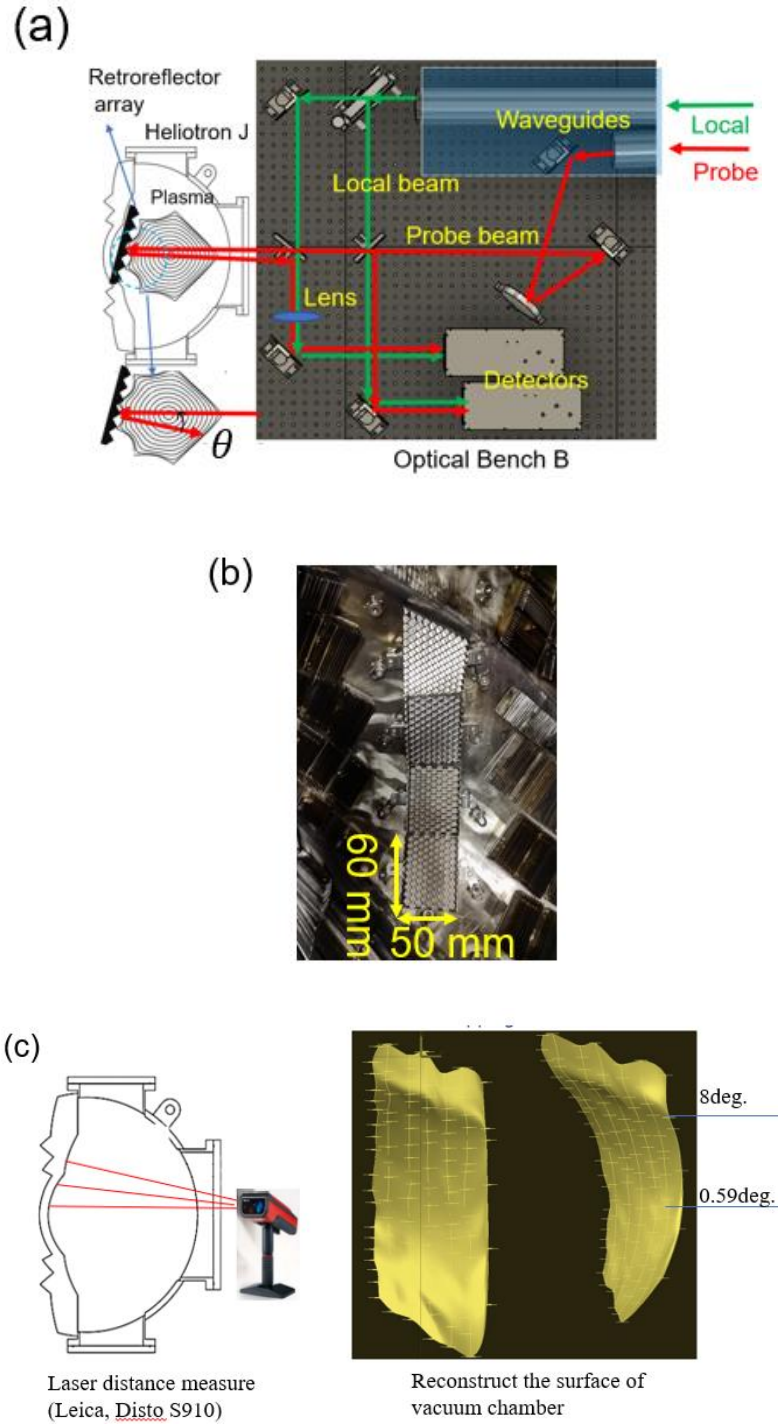

Fig. 5.8. (a) The interferometer system with the retroreflector array in Heliotron J, (b) Retroreflector array installed on the vacuum chamber wall of Heliotron J. (c) Reconstruction of the surface by laser distance measurement [66].

Chapter 6

Measurement of electron density with interferometer system

A new 320 GHz solid-state source interferometer is developed in Heliotron J to explore the physics of high-density plasmas (ne > 2–3 × 10^{19} m^{-3}, typically) realized with advanced fueling techniques. We successfully measured the line-averaged electron density in high-density plasma experiments. This chapter will show the measurement results of the interferometer system.

6.1 Measurement result from single-channel interferometer with conventional gas puffing-fueled (GP)

The new single-channel submillimeter interferometer has been applied to the Heliotron J plasma experiments. An example of time traces of the plasma discharge is shown in Fig. 6.1. Figure 6.1 (a) shows the NBI heating power. The time trace of the gas puff control with the deuterium as the working gas is shown in Fig. 6.1 (b). Plotted in Fig. 6.1 (c) is the line-averaged electron density measured with the new single-channel interferometer. Fig. 6.1 (d) shows the line-averaged electron density measured with a microwave interferometer of 135 GHz located at the different diagnostic ports [66].

The plasma was initiated by a 70 GHz ECH with a power of 264 kW and sustained by the NBI only. The port-through powers of the NBIs were 186 and 216 kW (402 kW in total). During the NBI heating, the injection amount of the gas puff was increased like a step function at t = ~225 ms; subsequently, the line-averaged density reached n_e = 1.8 ×

10^{19} m^{-3}. The waveform of the new submillimeter interferometer agreed well with that of a conventional microwave interferometer (130 GHz) operating as a routine density diagnostic system in Heliotron J.

For the comparison between the two interferometer measurements, the results obtained from the new interferometer were plotted against those obtained from the conventional interferometer as a Lissajous figure, as shown in Fig. 6.2. Several shot data in ECH plasmas were used. The Pearson correlation coefficient between the two interferometers is approximately 0.99, with a standard error of approximately 0.03 for the shots. The result presented the linearity between the two interferometer measurements, demonstrating that the new interferometer system works appropriately and can be used in Heliotron J for routine density measurement. Because these two interferometers are installed at different ports with different paths, a small difference between them can be seen. For example, the contribution of the plasma outside the last closed flux surface should vary significantly, depending on the path of the interferometer, inducing a discrepancy of approximately 10% between the two interferometers. Such a discrepancy may emerge due to the strong asymmetry of scrape-off layer plasma in Heliotron J [90].

The density fluctuation was also measured in the plasma experiment. The spectrogram for the density fluctuation, measured with the new interferometer, is shown in Fig. 6.3 (b) and that for the magnetic probe in Fig. 6.3 (c). The sampling rate of the data acquisition system is 5 MS/s; however, the maximum frequency of the spectrogram is determined by the 1 MHz IF signal frequency, resulting in a Nyquist frequency of 500 kHz. We observed coherent modes in both the spectrograms (200–270 ms), where the modes were energetic-particle (EP)-driven magnetohydrodynamic (MHD) instabilities. The EP-driven MHD mode is frequently observed in the NBI heating plasma of Heliotron J [91,92].

6.2 Measurement result from single-channel interferometer with high-intensity gas puff fueling (HIGP)

The new system successfully measured the electron density during high-density plasma experiments with HIGP and Pellet injection. In Heliotron J, the ECH can sustain the plasma with the density of less than 3.0×10^{19} m^{-3}. To achieve high-density plasma ($ne > \sim 2–3 \times 10^{19}$ m^{-3}), NBI and some fueling techniques were needed.

Figure 6.4 shows the time traces of the electron density ne with the HIGP applied to the NBI plasma of Heliotron J to obtain high density plasma. The plasma was initiated by a short pulse of 70 GHz ECH and sustained only by the NBI. During NBI heating, the electron density increases because of the injection of deuterium molecules from the GP system. As depicted in Figure 6.4 (b), the HIGP injection occurred between 225-240 ms. The electron density experiences an immediate increase upon the initiation of HIGP. Based on the measurement results from the 320 GHz interferometer, the electron density reaches 4.3×10^{19} m^{-3} after the cessation of HIGP. Figure 6.4(d) shows the waveform of electron density measured by the 130 GHz microwave interferometer. Several fringe jumps happen at the initial of plasma and after the HIGP, which caused by refraction in higher density gradient.

6.3 Measurement result from single-channel interferometer in high-density plasma experiments with pellet injection

Fig. 6.5(a-d) shows the time traces of a high-density plasma experiment with a pellet injection into ECH ＋ NBI heating plasma. The ECH and NBI heating power, the gas puff, and line-averaged densities measured with the new and the microwave interferometers were plotted. In this experiment, the pellet was injected at approximately 275 ms, after which the line-averaged density increased rapidly. Even in high-density experiments, the new interferometer system achieved a reliable measurement; however, fringe jumps were often observed in the microwave interferometer.

As shown in Fig. 6.6, the waveforms of electron density of the 320GHz interferometer and the 130 GHz microwave interferometer are compared during 334-335ms. The black line denotes the 320 GHz interferometer, and the red line is the result of the 130 GHz microwave interferometer. During 334-335ms, there is a significant variation in density, resulting in a substantial change in the refractive index. Consequently, the probe beam of the 130 GHz microwave interferometer experiences fringe jump. On the contrary, the new interferometer system demonstrates the absence of fringe jumping, indicating its ability to reliably measurement even in high-density plasma experiments.

6.4 Measurement result from two-channel interferometer system

The single-channel 320 GHz interferometer system developed in Heliotron J has

been upgraded to a multi-channel system by extending the probe beam to a sheet beam to enable the measurement in Heliotron J. During the last experimental campaign, the multi-channel interferometer system successfully obtained electron density measurements using two channels. The results of electron density measurements at the center and edge of the plasma cross-section are shown in Fig .6.7. In ECH power modulation experiment, an increase in the power of the ECH results in a decrease in the measured electron density in the center and edge channels, as shown in Fig .6.8. The ECH power modulation most likely affected the density distribution of the plasma. The decrease in edge density may be caused by particle transport. Additionally, it is also possible that the crosstalk effect in the adjacent channels caused by the sheet beam has an impact on the actual measurements.

The waveforms of the electron density obtained by the two channels of the 320 GHz interferometer agreed well with the 130 GHz microwave interferometer during the ECH modulation experiment.

6.5 Discussion

We have successfully developed the 320 GHz interferometer system in Heliotron J. This achievement has allowed us to obtain line-average electron density measurements during the plasma experiments. In the previous year's experiments, we successfully implemented two-channel measurements with the Off-axis parabolic (OAP) system. However, we have observed that the edge channel sometimes exhibits weak signals, causing signal fringe jump during the initiation of plasma in certain shots.

To address this issue, we are considering two steps for future improvements. Firstly, improving the retroreflector array within the vacuum chamber for increasing the reflected signal strength for the probe beam, thereby enhancing the measurement quality. Secondly, we are actively pursuing the development of a new digital phase analysis method to mitigate fringe jumps and further refine our measurements [93].

6.6 Summary

The first measurement with the 320 GHz solid-state source interferometer was successfully performed in Heliotron J. We successfully measured the line-averaged electron density, and the measurement results agreed with that obtained from a microwave interferometer with a different viewing chord, demonstrating that the new system can be used for routine diagnostics in Heliotron J. Additionally, the measurement was conducted

in high-density plasma experiments involving pellet injection and HIGP. During the plasma experiment, density fluctuations were observed.

Subsequently, the single-channel interferometer has been upgraded to a multi-channel interferometer by incorporating a pair of off-axis parabolic mirrors for beam expansion into a sheet beam. As a result, measurement results from the two-channel configuration were obtained during the plasma experiment campaign.

However, we still encountered some measurement problems in the plasma experiments. For the single-channel measurement system, fringe jumps are likely to occur at higher densities (greater than 5×10^{19} m^{-3}), and for the two-channel measurement system, the detection signals of the edge channels are consistently weak, which also causes fringe jumps to occur. Due to the diffraction effect of the retroreflector array, the incident beam is deflected from the original direction, resulting in a reduction in the detected intensity of the probe beam. Optimizing the design of the retroreflector array may increase the detected signal intensity and decrease the occurrence of fringe jumps.

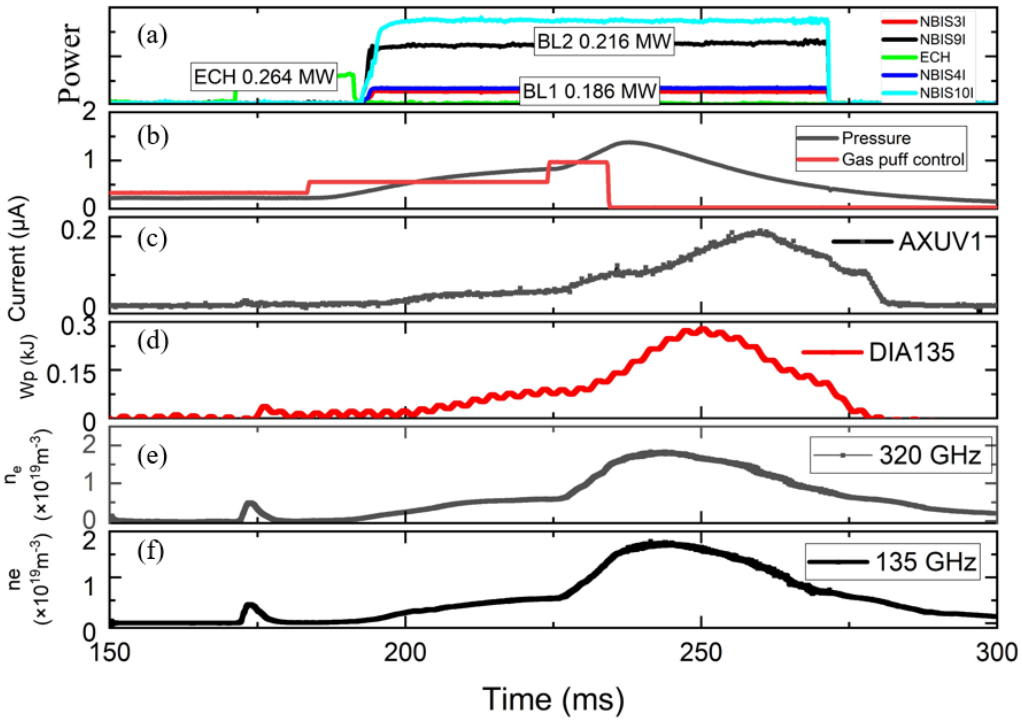

Fig. 6.1 Time trace of plasma discharge, (a) heating power, (b) gas puff, (c) radiation intensity form AXUV, (d) plasma stored energy (e) electron density measured with the new interferometer, and (f) electron density measured with the microwave interferometer.

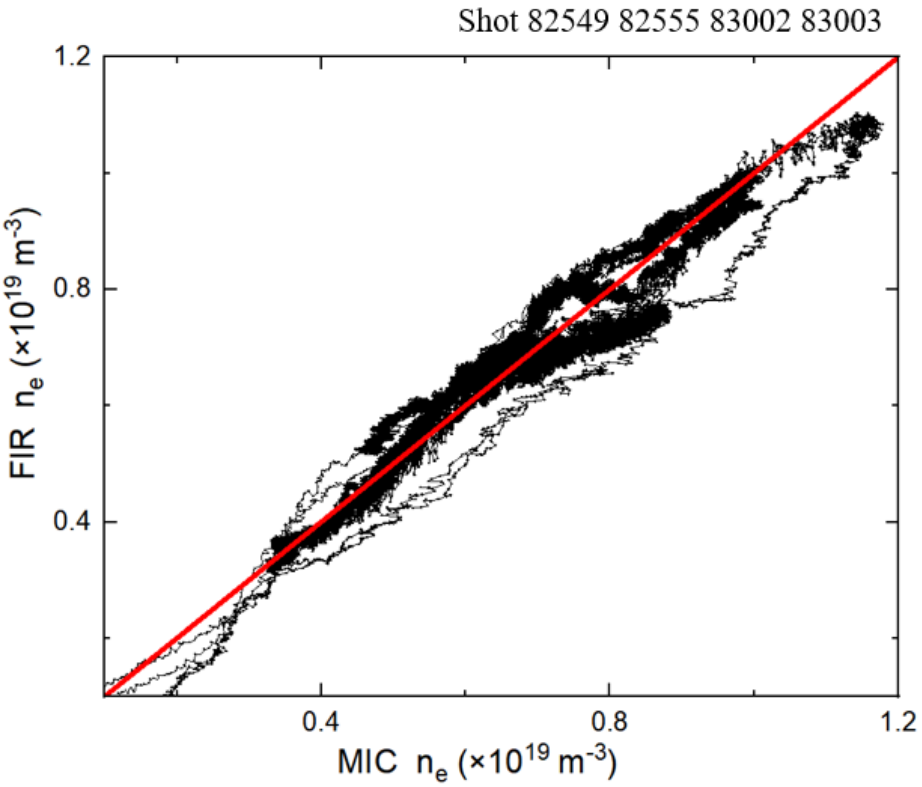

Fig. 6.2. Comparison between results of the new interferometer (FIR) and the microwave interferometer (MIC) for several shots [68].

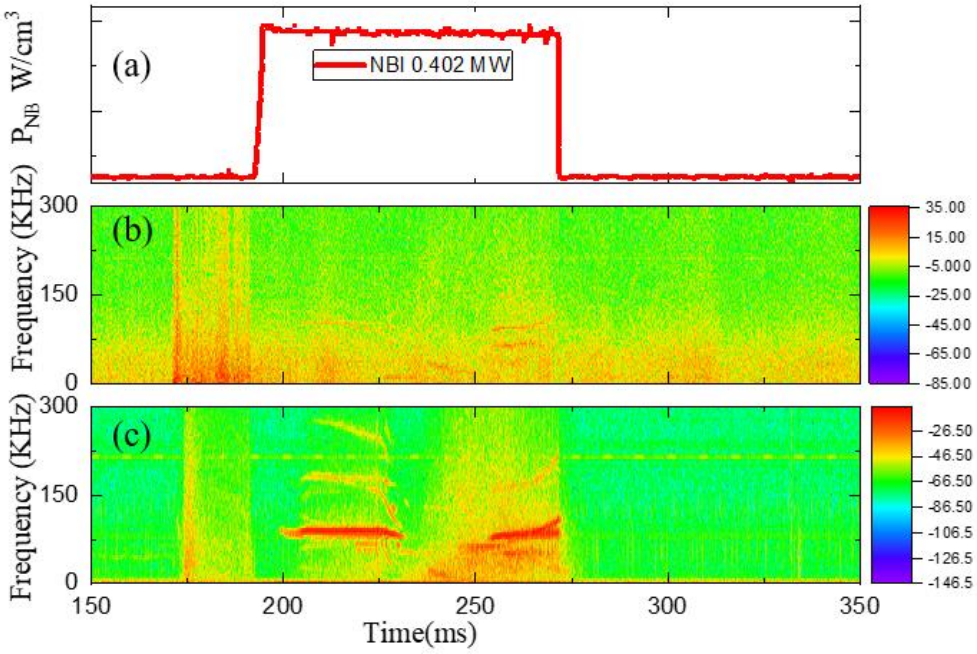

Fig. 6.3. (a) Time trace of heating power, spectrogram of (b)single-channel interferometer signal and (c) magnetic probe in plasma shot #82318 [68].

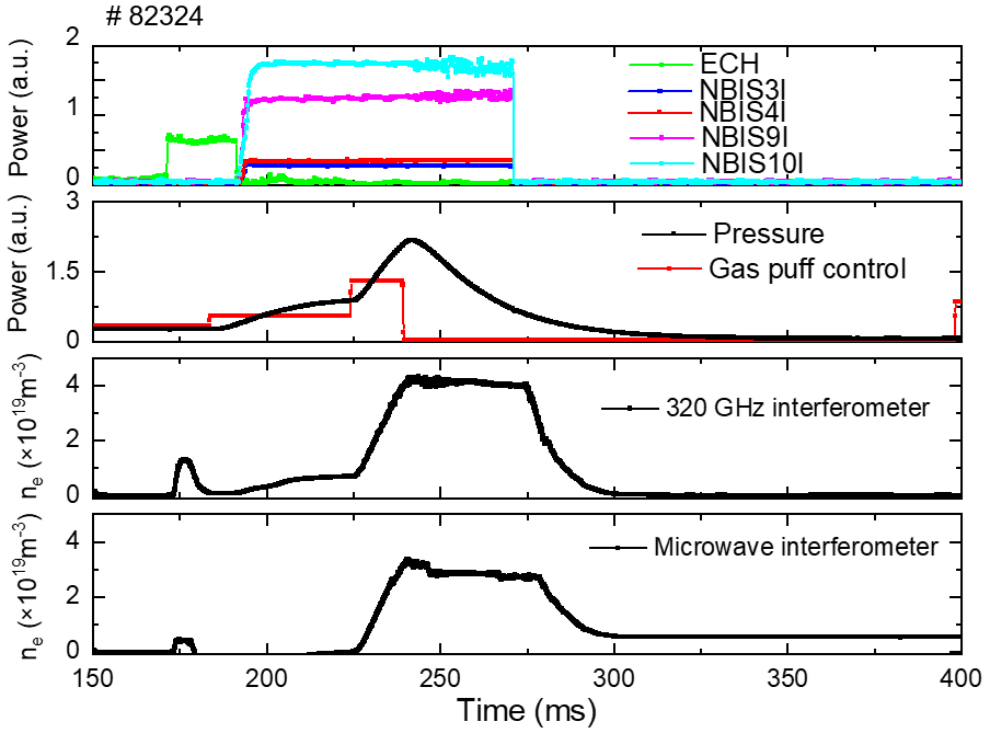

Fig. 6.4 Time trace of (a) heating power, (b) gas puff (c) electron density measured with the 320 GHz interferometer, and (d) electron density measured with the microwave interferometer in NBI only plasmas.

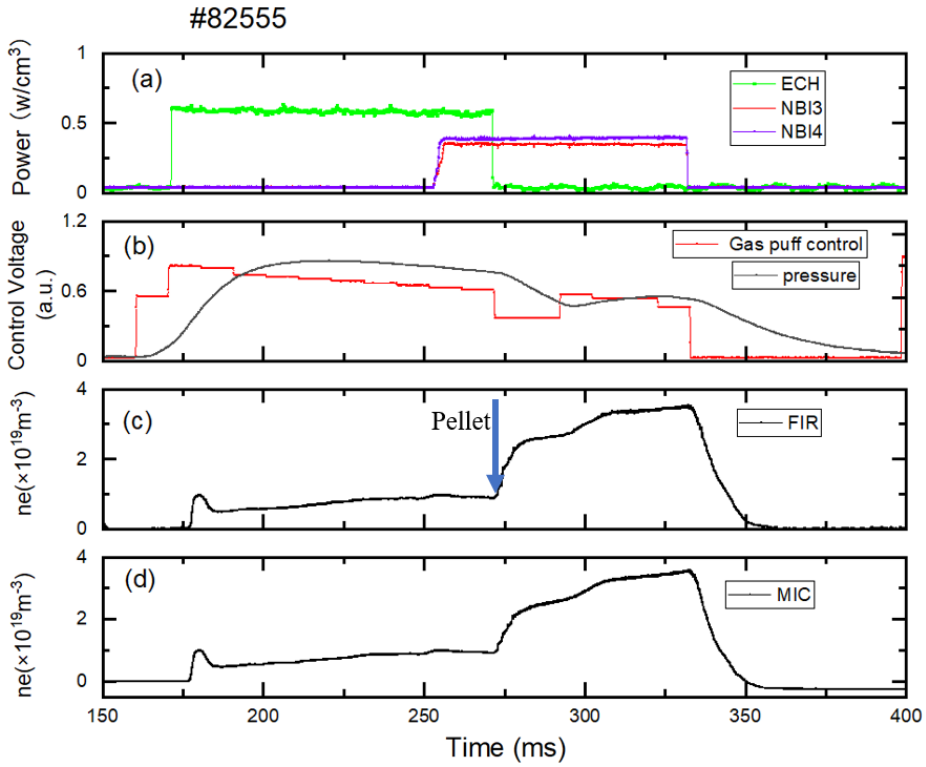

Fig. 6.5. Time trace of (a) heating power, (b) gas puff (c) electron density measured with the new interferometer, and (d) electron density measured with the microwave interferometer in ECH + NBI plasmas [68].

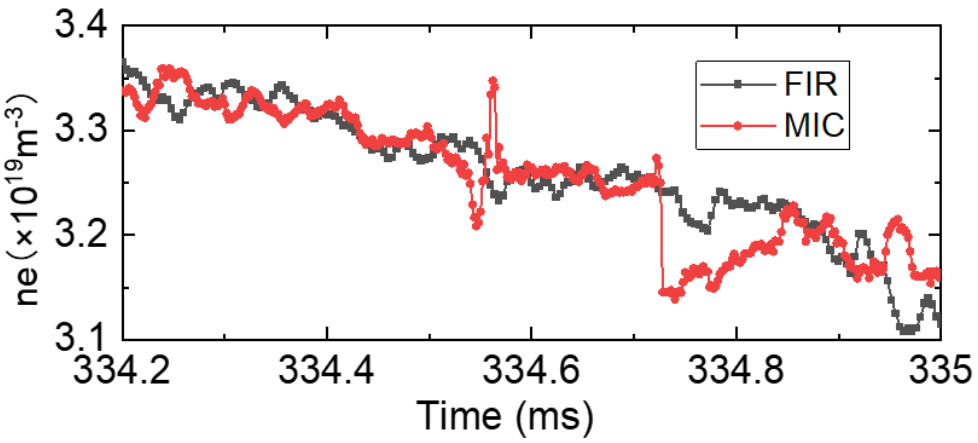

Fig. 6.6 The fringe jump from microwave interferometer was observed (334-335ms)

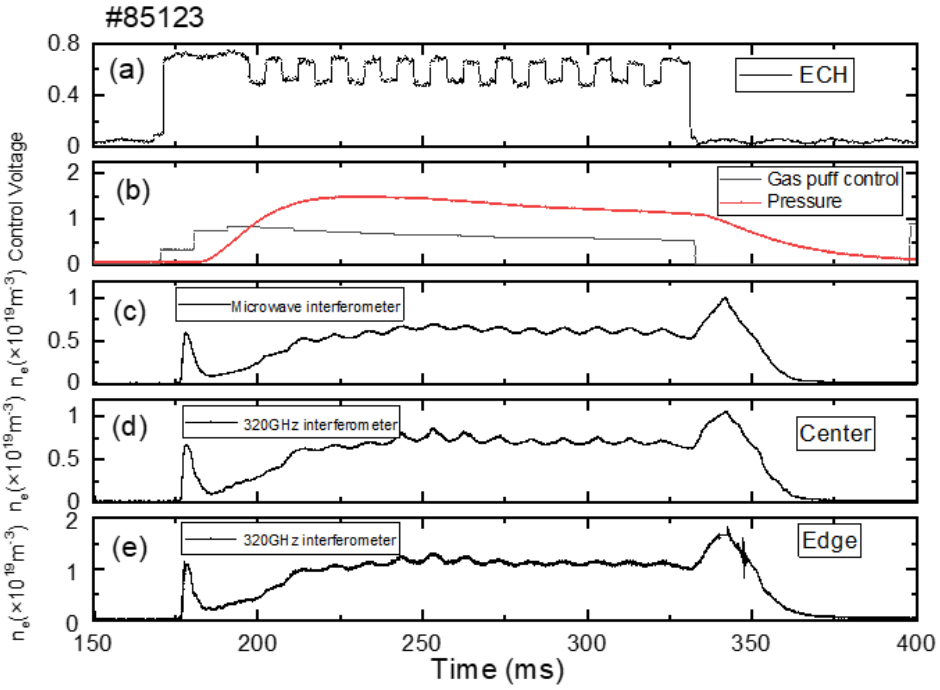

Fig. 6.7 Time traces of ECH(a), Control voltage for Gas-puff valves (GP) (b), the line-averaged density from the microwave interferometer(c) and two-channel interferometer(d),(e).

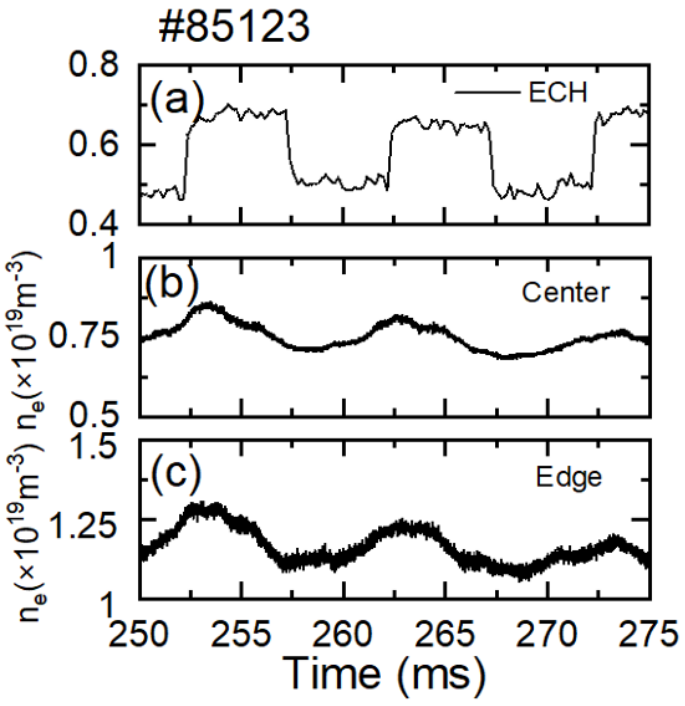

Fig. 6.8 The electron density in center and edge channel in ECH power modulation

Chapter 7

Summary

In this study, a multi-channel 320 GHz interferometer system was developed and constructed in Heliotron J to explore the physics of high-density plasmas realized with advanced fueling techniques. This system is equipped with two independent solid-state sources capable of delivering an output power of up to 50 mW, making it compact and easier to maintain. A high time resolution measurement of <1 μs can be derived by tuning the frequency of one source in the frequency range of 312–324 GHz on the new system, which can realize the fluctuation measurement. During the Heliotron J experiment campaign, the interferometer system successfully measured the electron density using advanced fueling techniques. The measured density agreed well with a microwave interferometer measurement using a different viewing chord, demonstrating that the new system can be used for routine diagnostics of electron density in Heliotron J.

A retroreflector array, comprising a cluster of small corner-cube retroreflectors, has the potential to be used as a reflector in confined spaces within fusion plasma experiments. The properties of a retroreflector array have been experimentally characterized in the tabletop experiment. For the first time, we have experimentally demonstrated that the retroreflector array exhibits combined functions as a retroreflector and a grating. A focusing lens in front of a detector can be one of the options to suppress the impact of the grating effect. The interferometer with the same retroreflector array as in the tabletop experiment has been developed in Heliotron J and successfully applied to the density measurement, which demonstrates that the retroreflector array can be a convenient and effective option as an instrument for the interferometer system in fusion research.

Each chapter is summarized as follows.

In chapter 1, summarized the development of nuclear fusion energy to achieve carbon neutrality for the improvement of the Earth's environment. In the pursuit of magnetic confinement fusion, which holds the greatest potential for achieving fusion energy on Earth, the increase of plasma density plays a vital role in enhancing energy confinement. Consequently, precise measurement and comprehensive analysis of plasma density are very important. The interferometer is a crucial measurement method extensively employed in fusion devices. This section presents a previous study on interferometers and briefly outlines their application in fusion devices like tokamaks and stellarators/heliotron. Finally, the motivation and objectives of this research are presented to develop a new interferometer to measure plasma electron density for the study of high-density and high-performance plasmas.

In chapter 2, the principle of the interferometer measurement is summarized. Interferometer depends on the phase change before and after the transmission of the electromagnetic waves in a plasma. From the Appleton-Hartree formula, we can derive the relationship between the phase difference and the density of plasma. The principle of the different types of interferometers is introduced, the Michelson-type interferometer with compact configuration is suitable for Heliotron J. The explanation of the interferometer detection method is presented, the method of heterodyne is introduced in detail. Finally, the interferometer utilized in the fusion device is summarized, serving as a comprehensive reference framework for the design of the interferometer on Heliotron J.

In chapter 3, the Heliotron J device is introduced. Heliotron J is a medium sized plasma experimental device with an advanced helical axis heliotron to test the new physics principles to extend the future of the heliotron line. A brief description is provided regarding the heating and advanced fueling technology employed in Heliotron J. Additionally, an overview of some diagnostic systems utilized in the experiment is presented.

In chapter 4, the design and construction of the new submillimeter wave interferometer system are summarized. The interferometer system we developed is a Michelson type, based on the heterodyne principle, with two independent solid-state sources. Two solid-state THz sources as the microwave generator can provide up to 50 mW microwave with compacted structure, high stability, and ease of maintenance. Initially, a single-channel 320 GHz interferometer was constructed and operated as the commissioning. Following its successful performance in Heliotron J, the single-channel interferometer was upgraded to a multi-channel system. This upgrade involved the

introduction of a pair of OAP (Off-Axis Parabolic) mirrors to expand the beam into a sheet beam, enabling the multichannel measurement. As a result, a new 320 GHz multichannel interferometer system with high time resolution was developed specifically for electron density measurements in Heliotron J.

In chapter 5, we have experimentally characterized the properties of a retroreflector array in a tabletop experiment, motivated by its application to the interferometry in a fusion plasma experiment. A THz imaging camera was used to measure the reflected beam profiles from the array at different incident angles. A tabletop experiment is performed to investigate the effect of the retroreflector array on the reflected beam properties. The results from an imaging camera exhibit that diffraction effect on the reflected beam, resulting in the emergence of separated peaks on the reflected beam profile, as predicted in the past numerical study; however, the most reflected beam power converges on the one reflected into the incident direction, showing the property as a retroreflector. Furthermore, the dependence of the reflected beam on the incident beam angle is characterized while fixing the detector position and the retroreflection beam is found to oscillate every 5 degree due to the diffraction effect. Such an undesired oscillation of beam power induced by the diffraction can be substantially suppressed with a focusing lens placed at the front of the detector in the practical application of an interferometer.

In chapter 6, the measurement results of the electron density are summarized. The measurement result agreed with that obtained from a microwave interferometer with a different viewing chord, demonstrating that the new system can be used for routine diagnostics in Heliotron J. Furthermore, the measurement was performed in high-density plasma experiments with a pellet injection and HIGP. Density fluctuations were observed during the plasma experiment.

Acknowledgements

I would like to express my deepest gratitude to my academic advisor Prof. Nagasaki Kazunobu for his unwavering guidance, boundless patience, and exceptional expertise. Prof. Nagasaki providing meticulous guidance on the direction of my research. His unwavering support during the experimental phase was instrumental in enabling significant progress in my research endeavors. It is with his guidance and encouragement, I successfully completed this thesis.

I would like to extend my profound gratitude to Asst. Prof. Ohshima Shinsuke (University of California, Irvine) for his invaluable contributions to this research journey. We had a lot of discussions that were important to me both in academic and in life. In addition, he has helped me to improve my article writing and presentation skills. Without his assistance and these meaningful discussions, it would not have been possible for me to complete this Ph.D. thesis.

I sincerely thank Assoc. Prof. Kobayashi Shinji, his advice in experimentation and article writing has been very inspiring and helpful to me.

I wish to express my appreciation to the professors in Heliotron J: Prof. Inagaki Shigeru, Assoc. Prof. Kado Shinichiro, Assoc. Prof. Minami Takashi, Asst. Prof. Kin Fumiyoshi, Dr. Okada Hiroyuki, Emeritus Prof. Mizuuchi Tohru, and Dr. Konoshima Shigeru for their support in experiment and fruitful discussions for my papers.

I appreciate Mr. Zhao Haochen, he assisted me with the experiment. Without his support, I cannot finish the construction of the interferometer system.

I need to thank the students in the Graduate School of Energy Science, Kyoto University: Dr. Qiu Dechuan, Dr. Wang Chenyu, Dr. Miyashita Akira, Dr. Iwata Akihiro, Dr. Feng Chao, Dr. Luo Maoyuan, were always help me in the experiment and life.

Finally, I would like to express my profound gratitude to my family. My wife, Liu Chengcheng, has provided unwavering support and encouragement, offering me the peace of mind necessary to successfully complete my doctoral research. My parents, Zhang Shijie and Sun Wenling, have stood by me quietly, enabling me to accomplish my research tasks. Additionally, I am thankful to my cousin, Sun Yuchuan, whose encouragement has been a constant source of motivation for continuous improvement.

Lists of Publication and Presentations

Publication

1. P. Zhang, S. Ohshima, H. Zhao, S. Kobayashi, S. Kado, T. Minami, F. Kin, A. Miyashita, A. Iwata, Y.Kondo, D. Qiu, C. Wang, M. Luo, S. Konoshima, S.Inagaki, H. Okada, T. Mizuuchi, K. Nagasaki. “Characterization of a retroreflector array for 320-GHz interferometer system in Heliotron J”, Review of Scientific Instruments, 94, 093501, (2023).

2. P. Zhang, S. Ohshima, H. Zhao, C. Deng, S. Kobayashi, S. Kado, T. Minami, R. Matoike, A. Miyashita, A. Iwata, Y.Kondo, D. Qiu, C. Wang, M. Luo, S. Konoshima, S.Inagaki, H. Okada, T. Mizuuchi, K. Nagasaki. “Development and initial results of 320 GHz interferometer system in Heliotron J”, Review of Scientific Instruments, 93,113519, (2022).

3. Dechuan Qiu, Takashi Minami, Shinichiro Kado, Ryo Matsutani, Yusuke Toba, Naoki Kenmochi, Chihiro Takahashi, Chenyu Wang, Maoyuan Luo, Pengfei Zhang, Shinsuke Ohshima, Shinji Kobayashi, Hiroyuki Okada, Tohru Mizuuchi, Shigeru Konoshima, Ryo Yasuhara, Shigeru Inagaki, and Kazunobu Nagasaki. “Design of a dual scattering angle multi-pass Thomson scattering system with signal separation function on Heliotron J”, Review of Scientific Instruments, 94(1) (2023).

4. Dechuan Qiu, Takashi Minami, Shinichiro Kado, Shigeru Inagaki, Chenyu Wang, Ryo Matsutani, Yusuke Toba, Maoyuan Luo, Pengfei Zhang, Naoki Kenmochi, Shinsuke Ohshima, Shinji Kobayashi, Hiroyuki Okada, Tohru Mizuuchi, Shigeru Konoshima, Ryo Yasuhara, and Kazunobu Nagasaki. “Increased signal separation upgrade permits preliminary electron anisotropy measurements with Heliotron J multipass Thomson diagnostic” 94(2) (2023).

5. S. Ohshima, T. Suzuki, R. Matoike , G. Motojima, S. Kado, A. Mori , A. Miyashita , S.

Kobayashi , T. Minami , A. Iwata , D. Qiu , C. Wang , M. Luo , P. Zhang , Y. Kondo , N. Nishino , T. Mizuuchi, H. Okada, S. Konoshima , S. Inagaki & K. Nagasaki. “Three-dimensional dynamics of fuctuations appearing during pellet ablation process around a pellet in a fusion plasma experiment”, Scientific Reports, 2022,12(1), 14204.

6. S. Ohshima, P. Zhang, H. Kume, C. Deng, A. Miyashita, S. Kobayashi, H. Okada, T. Minami, S. Kado, P. Adulsiriswad, D. Qiu, M. Luo, R. Matoike, T. Suzuki, S. Konoshima, T. Mizuuchi, and K.Nagasaki. “Development of a multi-channel 320 GHz interferometer for high density plasma measurement in Heliotron J”, Review of Scientific Instruments, 92(5) (2021).

Presentations

1. P. Zhang, S. Ohshima, H. Zhao, S. Kobayashi, S. Kado, T. Minami, F. Kin, A. Miyashita, A. Iwata, Y.Kondo, D. Qiu, C. Wang, M. Luo, S. Konoshima, S.Inagaki, H. Okada, T. Mizuuchi, K. Nagasaki. “Construction and initial result of the 320 GHz interferometer system in Heliotron J” 第 39 回 プラズマ・核融合学会 年会, Nov. 22 –25, 2022. 富山 (Oral).

2. P. Zhang, S. Ohshima, H. Zhao, S. Kobayashi, S. Kado, T. Minami, F. Kin, A. Miyashita, A. Iwata, Y.Kondo, D. Qiu, C. Wang, M. Luo, S. Konoshima, S.Inagaki, H. Okada, T. Mizuuchi, K. Nagasaki. “Properties and characterization of retroreflector array for multi-channel 320 GHz interferometer system in Heliotron J” 31th International Toki Conference (ITC), Nov.8-11, 2022. Toki, Japan (Poster).

3. P. Zhang, S. Ohshima, H. Zhao, S. Kobayashi, S. Kado, T. Minami, R. Matoike, A. Miyashita, A. Iwata, Y.Kondo, D. Qiu, C. Wang, M. Luo, S. Konoshima, H. Okada, T. Mizuuchi, K. Nagasaki. “Initial result of the new 320 GHz interferometer system on Heliotron J” 第 14 回核融合エネルギー連合講演会, Jul.7-8, 2022. Online

conference (Poster).

4. P. Zhang, S. Ohshima, H. Zhao, C. Deng, S. Kobayashi, S. Kado, T. Minami, R. Matoike, A. Miyashita, A. Iwata, Y.Kondo, D. Qiu, C. Wang, M. Luo, S. Konoshima, S.Inagaki, H. Okada, T. Mizuuchi, K. Nagasaki. “Development and initial results of 320 GHz interferometer system in Heliotron J”, High-Temperature Plasma Diagnostics Conference May. 15 -19, 2022. Online conference (Poster).

5. P. Zhang, S. Ohshima, H. Kume, S. Kobayashi, H. Okada, T. Minami, S. Kado, S. Konoshima, T. Mizuuchi, K. Nagasaki. “Development and construction of 320 GHz interferometer system for Heliotron J” 第 38 回 プラズマ・核融合学会 年会, Nov. 22 –25, 2021. Online conference (poster).

6.P. Zhang, S. Ohshima, H. Zhao, S. Kobayashi, H. Okada, T. Minami, S. Kado, S. Konoshima, T. Mizuuchi, K. Nagasaki “ Development of 320 GHz interferometer system for Heliotron J” 12th International Symposium of Advanced Energy Science, Sept. 7-8, 2021. Online conference (Poster).

7.P. Zhang, S. Ohshima, H. Kume, S. Kobayashi, H. Okada, T. Minami, S. Kado, S. Konoshima, T. Mizuuchi, K. Nagasaki. “Development of 320 GHz interferometer system in Heliotron J” 第 37 回 プラズマ・核融合学会 年会, Dec. 1–4, 2020. Online conference (poster).

References

[1] Adopted I. Climate change 2014 synthesis report[J]. IPCC: Geneva, Szwitzerland, 2014.

[2] Lindsey, Rebecca, and LuAnn Dahlman. "Climate change: Global temperature." *Climate. gov* 16 (2020).

[3] Chen, Lin, et al. "Strategies to achieve a carbon neutral society: a review." *Environmental Chemistry Letters* 20.4 (2022): 2277-2310.

[4] Fankhauser, Sam, et al. "The meaning of net zero and how to get it right." *Nature Climate Change* 12.1 (2022): 15-21.

[5] Kang, Meimei, et al. "Balancing carbon emission reductions and social economic development for sustainable development: Experience from 24 countries." *Chinese Geographical Science* 30 (2020): 379-396.

[6] Deutch, John M., et al. "Update of the MIT 2003 future of nuclear power." *Cambridge, mass.: Report for massachusetts institute of technology. retrieved september* 17 (2009): 2009.

[7] Patterson, Walter C. *Nuclear power*. London: Penguin Books, 1976.

[8] EUROfusion Consortium Research Institutions. Fusion History Timeline. https://euro-fusion.org/fusion/history-of-fusion/.

[9] EUROfusion Consortium Research Institutions. Fusion on the sun. https://euro-fusion.org/fusion/fusion-on-the-sun/

[10] Wesson, John, and David J. Campbell. *Tokamaks*. Vol. 149. Oxford university press, 2011.

[11] Francis F. Chen, An Indispensable Truth (published in Springer, 2011).

[12] L.A. Artsimovich et al., Proceedings of Plasma Physics and Controlled Nuclear Fusion Research, 1 (1968) 17.

[13] N.J Peacock et al., Nature, 224 (1969) 488.

[14] G. Grieger et al, Nuclear Fusion, 25 (1985) 1231.

[15] M. Yoshikawa, Nuclear Fusion, 25 (1985) 1081.

[16] R. Aymar, IEEE Transaction of Plasma Science, 25 (1997) 1187.

[17] Spitzer Jr, Lyman. "The stellarator concept." *The Physics of Fluids* 1.4 (1958): 253-264.

[18] MATSUOKA Keisuke. "New Trend of Helical System Research" J. Plasma Fusion Res. Vol.78, No.3 (2002) 200 – 204

[19] K. Uo et al., Proceedings of the workshop, Varenna, (1977) 369.

[20] K. Nishimura et al., Fusion Technology, 17 (1990) 86.

[21] A. Iiyoshi et al., Fusion Technology, 17 (1990) 169.

[22] J. Sapper and H. Renner, Fusion Technology, 17 (1990) 62.

[23] Padron, Ivan, ed. *Interferometry: Research and Applications in Science and Technology*. BoD–Books on Demand, 2012.

[24] Bass, Michael, et al., eds. *Handbook of optics*. Vol. 2. New York: McGraw-Hill, 1995.

[25]Hariharan, Parameswaran. *Basics of interferometry*. Elsevier, 2010.
[26] Hutchinson, Ian H. "Principles of plasma diagnostics." *Plasma Physics and Controlled Fusion* 44.12 (2002): 2603-2603.
[27] Hariharan, Parameswaran. *Optical interferometry, 2e*. Elsevier, 2003.
[28] Donné, A. J. H. "High spatial resolution interferometry and polarimetry in hot plasmas." *Review of scientific instruments* 66.6 (1995): 3407-3423.
[29] Akiyama, T., et al. "Interferometer systems on LHD." *Fusion Science and Technology* 58.1 (2010): 352-363.
[30] Li, Y. G., et al. "A new high sensitivity far-infrared laser interferometer for the HL-2A tokamak." *Review of Scientific Instruments* 88.8 (2017): 083508.
[31] Deng, Chuanbao, et al. "First results from the multichannel interferometer system on HSX." *Review of scientific instruments* 74.3 (2003): 1625-1628.
[32] S. Kobayashi, T. Mizuuchi, Y. Nakashima, K. Nagasaki, H. Okada, T. Minami, S. Kado, S. Yamamoto, S. Ohshima, H. Y. Lee et al., 40th EPS Conference on Plasma Physics (2013).
[33] T. Mizuuchi, H.Y. Lee, K. Mukai, K. Yamamoto, S. Kobayashi, H. Okada, S. Yamamoto, S. Ohshima, L. Zang, K. Nagasaki et al., Journal of Nuclear Materials 438 (2013).
[34]Y. Ohtani, S. Ohshima, N. Asavathavornvanit, T. Akiyama, T. Minami, K. Tanaka, K. Nagasaki, N. Shi, T. Mizuuchi, N. B. Marushchenko et al., Plasma Fusion Res. 10, 1402091 (2015).
[35] Motojima, G., et al. "High-density experiments with hydrogen ice pellet injection and analysis of pellet penetration depth in Heliotron J." *Plasma Physics and Controlled Fusion* 61.7 (2019): 075014.
[36] Zhou, Y., et al. "Multi-channel far-infrared HL-2A interferometer-polarimeter." Review of Scientific Instruments 83.10 (2012): 10E336.
[37] Zhou, Y., et al. "A new multichannel interferometer system on HL-2A." *Review of Scientific Instruments* 78.11 (2007): 113503.
[38] D. Veron, Infrared and Millimeter Wave (Academic Press, New York), Vol. 2 (1979).
[39] Li, J., et al. "Development and preliminary experimental results of a high-temporal-resolution terahertz solid-source interferometer on EAST." *Journal of Instrumentation* 15.02 (2020): C02048.
[40] Y. Ohtani. ヘリカル型閉じ込め装置におけるイオン種の違いが粒子輸送に与える影響に関する研究. PhD thesis, Kyoto University, Kyoto, 2017.
[41] Kim, Sung K., et al. "High-resolution multichannel interferometric measurement of sawtooth density-pulse propagation." Review of Scientific Instruments 59.8 (1988): 1550-1555.
[42] Kawahata, K., et al. "Far infrared laser interferometer system on the Large Helical Device." *Review of scientific instruments* 70.1 (1999): 707-709.
[43] D. L. Brower, C. Deng, W. X. Ding D. T. Anderson, W. Mason, Rev. Sci. Instrum. 72, 1081 (2001).

[44] Obiki, T., et al. "First plasmas in Heliotron J." *Nuclear fusion* 41.7 (2001): 833.
[45] Obiki, T., et al. "Goals and status of Heliotron J." *Plasma Physics and Controlled Fusion* 42.11 (2000): 1151.
[46] Nagasaki, K., et al. "Stabilization of energetic-ion-driven MHD modes by ECCD in Heliotron J." *Nuclear Fusion* 53.11 (2013): 113041.
[47] Sano, Fumimichi, et al. "Physics of Heliotron J confinement." *Plasma and Fusion Research* 5 (2010): S2003-S2003.
[48] Wakatani, M., et al. "Study of a helical axis heliotron." Nuclear fusion 40.3Y (2000): 569.
[49] Kobayashi, S., et al. "Fast-Ion Response to Energetic-Particle-Driven MHD Activity in Heliotron J." Contributions to Plasma Physics 50.6-7 (2010): 534-539.
[50] Nagasaki, K., et al. "Heliotron J Experiments"J. Plasma Fusion Res. Vol.96, No.9 (2020)475-518.
[51] Matoike, R. ヘリオトロン J3 次元磁場における周辺プラズマ輸送およびダイバータ熱負荷に関する研究. PhD thesis, Kyoto University, Kyoto, 2022.
[52] Mizuuchi, T., S. Kobayashi, and T. Minami. A new operation regime for high-density plasma in Heliotron J. No. NIFS--1121. National Inst. for Fusion Science, 2014.
[53] Nagasaki, K., et al. "ECCD Experiments Using the Upgraded Launching System in Heliotron J." Contributions to Plasma Physics 50.6-7 (2010): 656-660.
[54] Okada, Hiroyuki, et al. "Formation and confinement of high-energy ions in heliotron J." Fusion science and technology 50.2 (2006): 287-293.
[55] Motojima, G., et al. "High-density experiments with hydrogen ice pellet injection and analysis of pellet penetration depth in Heliotron J." Plasma Physics and Controlled Fusion 61.7 (2019): 075014.
[56] Mizuuchi, T., et al. "Effects of Supersonic Molecular Beam Injection (SMBI) on plasma performance in heliotron J." Contributions to Plasma Physics 50.6-7 (2010): 639-645.
[57] Yao, Lianghua, et al. "Plasma behaviour with hydrogen supersonic molecular beam and cluster jet injection in the HL-2A tokamak." Nuclear fusion 47.11 (2007): 1399.
[58] Mizuuchi, T., et al. "Gas fueling effect on plasma profile in Heliotron J." Journal of Nuclear Materials 438 (2013): S453-S458.
[59] Luo, Maoyuan, et al. "Measurement of Electron Temperature Profile and Fluctuation with ECE Radiometer System in Heliotron J." Plasma and Fusion Research 15 (2020): 2402038-2402038.
[60] Kenmochi, N., et al. "First measurement of time evolution of electron temperature profiles with Nd: YAG Thomson scattering system on Heliotron J." Review of Scientific Instruments 85.11 (2014): 11D819.
[61] Minami, Takashi, et al. "Design of a new high repetition rate Nd: YAG Thomson scattering system for Heliotron J." Review of Scientific Instruments 81.10 (2010): 10D532.
[62] Besshou, S., et al. "Diamagnetic double-loop method for a highly sensitive measurement of energy stored in a Stellarator plasma." Review of Scientific Instruments

72.10 (2001): 3859-3863.
[63] Watanabe, S., et al. Measurement of radiation profile at density ramp-up phase by using AXUV photodiode arrays in Heliotron J. No. NIFS-PROC--69-V2. 2008.
[64] Watanabe, S., et al. Radiation measurement in Heliotron J by using an AXUV photodiode array with multiple optical filters. No. NIFS-PROC--78. 2009.
[65] M. Takeda. ヘリオトロンJプラズマにおける電子密度制御. Master thesis, Kyoto University, Kyoto, 2002.
[66] H. Kume.ヘリオトロン Jにおける高密度プラズマ計測用 320GHz 多視線干渉計の開発. Master thesis, Kyoto University, Kyoto, 2020.
[67] Ohshima, S., et al. "Development of a multi-channel 320 GHz interferometer for high density plasma measurement in Heliotron J." Review of Scientific Instruments 92.5 (2021): 053519.
[68] Zhang, P., et al. "Development and initial results of 320 GHz interferometer system in Heliotron J." Review of Scientific Instruments 93.11 (2022): 113519.
[69] Goldsmith, Paul F. Quasioptical systems. New York, NY, USA: Chapman & Hall, 1998.
[70] Goldsmith, Paul F. "Quasi-optical techniques." Proceedings of the IEEE 80.11 (1992): 1729-1747.
[71] Kogelnik, Herwig, and Tingye Li. "Laser beams and resonators." Applied optics 5.10 (1966): 1550-1567.
[72] Crenn, J. P. "Optical study of the EH 11 mode in a hollow circular oversized waveguide and Gaussian approximation of the far-field pattern." Applied optics 23.19 (1984): 3428-3433.
[73] Crenn, J. P. "Optical theory of Gaussian beam transmission through a hollow circular dielectric waveguide." Applied Optics 21.24 (1982): 4533-4541.
[74] H. Zhao. Design and construction of 320 GHz interferometer for electron density measurement in Heliotron J. Master thesis, Kyoto University, Kyoto, 2023.
[75] Ahmed, Rajib, et al. RSC advances 7.41 (2017): 25657-25664.
[76] Zhou L, Kahn J M, Pister K S J. Journal of microelectromechanical systems, 12(3): 233-242(2003).
[77] S. Wang, T. Sherlock, B. Salazar, N. Sudheendran,R. K. Manapuram, K.Kourentzi, P. Ruchhoe, IEEER. C. Willson and K. V. Larin, IEEE Sens. J., 2013, 13, 4534 –4541.
[78] Zhong-Ping Zhang, Hai-Feng Zhang, Wan-Zhen Chen ,Pu Li, Wen-Dong Meng , Yuan-Ming Wang, Jie Wang, Wei Hu, Fu-Min Yang, Advances in Space Research. 54, (5), 811-817(2014).
[79] Konan Peck; Michael D. Morris, Rev Sci Instrum 58, 189–196 (1987).
[80] Eckhardt, H. D. Applied Optics 10.7 (1971): 1559-1566.

[81] Hiroyuki Ichikawa, J. Opt. A: Pure Appl. Opt. 6,S121–S127, (2004).
[82] R. Imazawa, Y. Kawano, T. Ono, Y. Kusama., Rev Sci Instrum 82, 023116 (2011).
[83] Ryota Imazawa, Yasunori Kawano, Takehiro Ono, Yoshinori Kusama., Plasma and Fusion Res. 6, 02402032 (2011).
[84] Christopher Palmer, DIFFRACTION GRATING HANDBOOK. Sixth edition(2005).
[85] ERWIH 6. LOEWEH, Diffraction gratings and applications. (1997).
[86] Pozar, David M. Microwave engineering. John wiley & sons, Fourth edition (2011).
[87] Hansen, R. C., and W. T. Pawlewicz. IEEE Transactions on Microwave Theory and Techniques 30.11: 2064-2066 (1982).
[88] K. Nagasaki, S. Kobayashi, K. Sakamoto, H. Zushi, T. Obiki, K. Ohkubo, M. Kawaguchi, G G. Denisov, A L. Goldenberg, V I. Kurbatov et al., Fusion technology, 32.2: 287-295 (1997).
[89] Zhang. P., et al. "Characterization of a retroreflector array for 320-GHz interferometer system in Heliotron J." Review of Scientific Instruments 94.9 (2023).
[90] R. Matoike, G. Kawamura, S. Ohshima, M. Kobayashi, Y. Suzuki, K. Nagasaki, S. Masuzaki, S. Kobayashi, S. Yamamoto, S. Kado et al., Plasma Fusion Res. 3403127 (2019).
[91] S. Yamamoto, K. Nagasaki, K. Nagaoka, J. Varela, A. Cappa, E. Ascasíbar, F. Castej´on, J.M. Fontdecaba, J.M. García-Regaña, A. Gonz´alez-Jerez et al., Nucl. Fusion 60, 066018 (2020).
[92] S. Ohshima, S. Kobayashi, S. Yamamoto, K. Nagasaki, T. Mizuuchi, H. Okada, T. Minami, K. Hashimoto, N. Shi, L. Zang et al., Nucl. Fusion 56 (2016) 016009.
[93] SAKAI, Hikona, et al. "Application of Digital Phase Analysis to Far-Infrared Laser Interferometer for the Large Helical Device." Plasma and Fusion Research 18 (2023): 1402062-1402062.